

Bio-Inspired Trailing Edge Noise Control: Acoustic and Flow Measurements

Anthony J. Millican

Thesis submitted to the faculty of the
Virginia Polytechnic Institute and State University
in partial fulfillment of the requirements for the degree of

Master of Science
in
Aerospace Engineering

William J. Devenport, Chair
W. Nathan Alexander
K. Todd Lowe

May 9, 2017
Blacksburg, Virginia

Keywords: Aeroacoustics, Trailing Edge Noise, Noise Control, Bio-Inspired, Shear Sheltering, Turbulent Wall Jet, Hot-Wire Anemometry, Mixing Layer

Bio-Inspired Trailing Edge Noise Control: Acoustic and Flow Measurements

Anthony J. Millican

ACADEMIC ABSTRACT

Trailing edge noise control is an important problem associated mainly with wind turbines. As turbulence in the air flows over a wind turbine blade, it impacts the trailing edge and scatters, producing noise. Traditional methods of noise control involve modifying the physical trailing edge, or the scattering efficiency. Recently, inspired by the downy covering of owl feathers, researchers developed treatments that can be applied to the trailing edge to significantly reduce trailing edge noise. It was hypothesized that the noise reduction was due to manipulating the incoming turbulence, rather than the physical trailing edge itself, representing a new method of noise control. However, only acoustic measurements were reported, meaning the associated flow physics were still unknown. This thesis describes a comprehensive wall jet experiment to measure the flow effects near the bio-inspired treatments, termed “finlets” and “rails,” and relate those flow effects to the noise reduction. This was done using far-field microphones, a single hot-wire probe, and surface pressure fluctuation microphones. The far-field noise results showed that each treatment successfully reduced the noise, by up to 7 dB in some cases. The surface pressure measurements showed that the spanwise coherence was slightly reduced when the treatments were applied to the trailing edge. The velocity measurements clearly established the presence of a shear layer near the top of the treatments. As a whole, the dataset led to the shear-sheltering hypothesis: the bio-inspired treatments are effective based on reducing the spanwise pressure correlation and by sheltering the trailing edge from turbulent structures with the shear layer they create.

Bio-Inspired Trailing Edge Noise Control: Acoustic and Flow Measurements

Anthony J. Millican

GENERAL AUDIENCE ABSTRACT

This thesis describes a project aimed at developing a technology inspired by the silent flight of owls, with the end goal of using this technology to reduce the noise generated by wind turbines. Specifically, the phenomenon known as “trailing edge noise” is the primary source of wind turbine noise, and is the noise source of interest here. It occurs when air turbulence (which can be thought of as unsteady air fluctuations) crashes into the rear (trailing) edge of wind turbine blades, scattering and producing noise. Typically, methods of reducing this noise source involve changing the shape of the trailing edge; this may not always be practical for existing wind turbines. Recently, inspired by the downy covering of owl feathers, researchers developed treatments that can be applied directly to the trailing edge, significantly reducing trailing edge noise. This bio-inspired concept was verified with numerous acoustic measurements. Based on those measurements, researchers hypothesized that the noise reduction was achieved by manipulating the incoming turbulence before it scattered off the trailing edge, rather than by changing the existing wind turbine blade, representing a new method of trailing edge noise control. However, as only acoustic measurements (not flow measurements) were reported, the changes in turbulence could not be examined.

With the above motivation in mind, this thesis describes a comprehensive wind tunnel experiment to measure the changes in the aerodynamics and turbulence near the bio-inspired treatments, and relate those changes to the reduction in trailing edge noise. This was done using a hot-wire probe to measure the aerodynamics, as well as microphones to measure the radiated noise and surface pressure fluctuations. As a whole, the experimental results led to the shear-sheltering hypothesis: the bio-inspired treatments are effective based on the creation of a shear layer (a thin region between areas with different air speeds) which shelters the trailing edge from some turbulence, as well as by de-correlating surface pressure fluctuations along the trailing edge.

Acknowledgments

This is my favorite part of any report. Quality work does not happen in a vacuum; it happens in collaborative environments like the Center for Renewable Energy and Aerodynamic Testing (CREATE), where I have been blessed to conduct my graduate work. There are many, many people responsible for making such a wonderful working environment at CREATE, and at Virginia Tech (VT) at large. I will do my best to thank them all here.

First, I'd like to thank my advisor, Dr. William Devenport, for gambling on me when I approached him out of the blue and asked to join his research group. I will be forever grateful he said yes. Next, I'd like to thank committee members Drs. Nathan Alexander and Todd Lowe, for their guidance and mentorship throughout this process. In fact, Dr. Lowe was the first professor I met at VT during my visit, and it was the friendly conversation we had that made me realize I might be able to survive moving from San Diego to Blacksburg.

I have always said that who I work with is as important to me as the work I'm doing. At CREATE, we have a warm and welcoming research community that is completely at odds with what I expected graduate school to be like. Thanks to Tamara Guimaraes-Bucalo, Sean Shea, Tyler Vincent, Will George, Tamar Daniels, Christopher Hickling, Marcie Stuber, Matt Boyda, Matt Ruda, and Manasi Palwankar among many others, for being such great friends. I intentionally left out my labmates, who deserve a special thanks for putting up with me. Liselle Joseph, you told me on Day 1 that I belonged here, and you'll never know how much that meant. Agastya Balantrapu, what is there to say? I'm so glad you joined the team, and I'm looking forward to many (well, not THAT many) more years together; we're not done yet. And of course, DOCTOR Ian Clark. You took the time to teach me how to be a good researcher when we both know it was inconvenient for you. You always did it with a smile, and I am incredibly glad I got to share an office with you and have you as a friend. I'll save the rest for a toast at your wedding.

My research was generously supported in part by the Office of Naval Research, grants N00014-16-1-2395 and N00014-15-1-2326. I'd also like to gratefully acknowledge the GEM Consortium and the New Horizons program at Virginia Tech for funding my graduate education. Through New Horizons, I am lucky to have two wonderful mentors in Drs. Jack Lesko and Catherine Amelink. I am also blessed to have made some great friends through New Horizons and our Graduate Society of Hispanic Professional Engineers (GradSHPE) chapter:

Javier Gonzalez-Rocha, who was my first friend in Blacksburg, as well as Andrea Rolong, Elisa Wasson, John Angarita, Mark Pastor Hurtado, and Andrea Ogilvie. Thank you for creating such a welcoming familia away from home. I also want to thank my roommates and friends Robert Mao and Chris Winslow, for being awesome. Chris, you were welcoming from the day we met, and were kind enough to introduce me to the wonderful people in food science, including Lily Yang, Jen Zornak, Oscar Galagarza, and Josh Lee.

You may have noticed there's one group of people I haven't thanked yet: my family! Obviously, I would not have made it this far without their unwavering love and support. Not many parents would have been so understanding about their "baby" moving across the country for more school, of all things (although Dad took some convincing). Of course, not many would replace their "baby" with a dog *before* he left, but that's beside the point. If I were to write down how grateful I am to the whole family, I'd have to turn this into a new chapter. So, thank you! to everyone who was a part of this, and as we'd say at SHPE UCSD, ¡Sí se puede!

Contents

1	Introduction	1
1.1	Background	1
1.2	Inspiration from Biology- The Silent Flight of Owls	2
1.2.1	Flow Effects due to a Canopy- Motivation for Finlets and Rails	3
1.3	Fundamentals of Trailing Edge Noise Theory	4
1.4	Experimental Validation of Trailing Edge Noise Theory	6
1.5	Trailing Edge Noise Control	8
1.6	Bio-Inspired Finlets and Rails	9
1.6.1	Pilot Study- Clark <i>et al.</i> [1]	9
1.6.2	Experimental and Theoretical Analysis- Clark <i>et al.</i> [2]	12
1.6.3	Related Experiments	14
1.7	Technical Justification and Contributions of this Thesis	15
1.7.1	Achievements	15
2	Experimental Methods	17
2.1	Anechoic Wall Jet	17
2.1.1	Flow Structure	20
2.2	Mock Trailing Edge	22
2.3	Far-Field Sound Measurements	27
2.4	Surface Pressure Fluctuation Measurements	30
2.5	Constant-Temperature Anemometry	31

2.5.1	Calibration	31
2.5.2	Measurement	33
2.6	Trailing Edge Treatments	38
2.7	Experimental Uncertainty	42
2.8	Test Plan	44
3	Results and Discussion	46
3.1	Far-Field Noise	46
3.1.1	Facility Acoustic Performance	46
3.1.2	Untreated Trailing Edge Noise	50
3.1.3	Finlet Effects on Far-Field Sound	56
3.2	Hot-Wire Measurements	59
3.2.1	Flow Near the Untreated Trailing Edge	63
3.2.2	Treatment Effects on the Mean Flow Quantities	64
3.2.3	Turbulence Spectra	74
3.2.4	Streamwise Development	78
3.3	Surface Pressure Fluctuations	79
4	Conclusions	100
	Bibliography	101

List of Figures

1.1	Idealized schematic of turbulent boundary layer-trailing edge noise.	5
1.2	Idealized schematic of trailing edge bluntness - vortex shedding noise.	8
1.3	Schematic of treatments tested by [1] on the trailing edge of a DU96-W180 airfoil. a) Finlets, b) Rails.	11
2.1	(a) Side-view schematic of the Virginia Tech Anechoic Wall Jet. Flow is from left to right. Dimensions are in millimeters. (b) Inset from figure 2.1a showing the coordinate system. The origin is on the smooth wall surface, on the spanwise center of the smooth wall. The x -direction is aligned with the flow, and the y -direction is the wall upward normal. The z -direction completes the right-handed coordinate system.	18
2.2	Wall jet interior, looking upstream. Coordinate system origin is on the smooth wall surface at the smooth wall centerline. The x -direction is aligned with the flow (out of the page). Far-field microphones shown in dashed circle.	19
2.3	Spanwise velocity variation, normalized on the maximum velocity in the boundary layer, U_m . Data measured by Ian Clark, *, estimated decay, dashed line, wall edges, solid line. Probe was located at $x = 1257.3$ mm, $y = 6.35$ mm.	19
2.4	Wall jet nomenclature based on Launder <i>et al.</i> [3]. The velocity profile has a maximum U_m occurring at $y = \delta$, the boundary layer thickness. For the VT Anechoic Wall Jet, a jet of air at $U = U_j$ is exhausted from a nozzle of height b into still air, meaning $U_\infty = 0$. Flow is from left to right.	21
2.5	Schematic of the mock trailing edge piece, including dimensions. (a) Top view. Clearance holes are for mounting surface pressure fluctuation microphones flush with the trailing edge surface. (b) Dimensions and numbering scheme for the surface pressure fluctuation microphone positions. See figure 2.5a for locations relative to entire trailing edge piece. (c) Side view, showing the 0.76 mm trailing edge.	23

2.6	CTA probe relative to the mock trailing edge. The figure can be thought of as being in the $x-y$ plane, where x is along the flow and y is the wall upward normal.	24
2.7	(a) Schematic of the 349.25 mm long transition ramp attached to the leading edge of the test article (side view). (b) Top view schematic of the transition ramp-trailing edge assembly. (c) Transition ramp attached upstream of the mock trailing edge, to ensure smooth boundary layer growth. The gap between the end of the mock trailing edge and the ramp edge did not need to be treated, as this is well outside the 2-D jet region.	25
2.8	Far-field spectra for $U_j=60$ m/s (measured at $\theta=123.5^\circ$, see following section for microphone setup details) showing the acoustic impact of the exposed outer edges of the transition ramp. Comparisons were made using rounded endpieces and a full-span trailing edge piece. Spectra are shown using different symbols for clarity.	26
2.9	Far-field microphone observer angles relative to trailing edge (a) Streamwise far-field array observer angles, measured relative to the upstream horizontal. Bolded microphone is at $\theta = 90^\circ$, and is also part of the spanwise array. (b) Spanwise far-field array observer angles, measured relative to the vertical. Bolded microphone at $\phi = 90^\circ$ is also part of the streamwise array.	29
2.10	Top view of two B&K 4138 microphones mounted flush with the smooth wall surface to measure unsteady surface pressure fluctuations.	29
2.11	Amplitude response of the B&K 4138 microphones with pinhole caps used to measure unsteady surface pressure fluctuations.	30
2.12	Close-up of the setup used to calibrate the jet. Flow travels from left to right, as indicated with thick arrows, through the Plexiglass settling chamber and the conical nozzle (both are outlined in black). The dashed line indicates the nozzle exit plane.	32
2.13	Calibration results for the CTA hot-wire system. Different markers-color combinations indicate data for each unique calibration used in acquiring the result presented in chapter 3. (a) King's Law fit (solid line) to the measured data, used to identify the A and B constants. (b) Inverse calibration curve, used to estimate the sensitivity $\partial U/\partial E$ for uncertainty analysis. (c) Variation in calibration flow temperature.	34
2.14	CTA set-up in the wall jet. Stepper motors and threaded rod for z -axis motion are not pictured. Figure is in the $y-z$ plane.	35

2.15	(a) Hot-wire probe location relative to the finlets (b) Schematic of the probe traverse profile. Vertical measurements are made along the channel centerline (vertical dashed line), and spanwise measurements are made from the outside of the left finlet to the outside of the adjacent one (horizontal arrow).	36
2.16	Turbulence spectra for each measurement run, with the probe located at (a) $y \approx 37$ mm, (b) $y \approx 63$ mm, and (c) $y \approx 81$ mm. The vertical black line (dash-dot) has been included to show the cutoff integration frequency (7000 Hz), and does not represent data.	37
2.17	Baseline finlet treatment applied to the mock trailing edge, with a hot-wire probe downstream. The inset image shows the nomenclature used for the finlet and rail treatments.	39
2.18	(a) Side view of the finlet treatment design. The treatment height, h , was one of the parameters varied in the study. The dashed lines are used to indicate the location and dimensions of the “mid-plane” finlets used to document the flow along a channel. Mid-plane pieces were only made for the Baseline and Short finlet designs. (b) Rail treatment, with the same design parameters as the “R0” treatment described in Clark <i>et al.</i> [1].	39
2.19	Schematic of the hot-wire measurements downstream of (a) the full Baseline finlet, and (b) the mid-plane of the Baseline finlet.	40
3.1	Far-field sound spectra for the clean wall cases, as measured by the microphone at $\theta = 123.5^\circ$. Nine different repetitions were performed for each speed.	47
3.2	Integrated sound levels for the clean wall cases, measured by the microphone at $\theta = 123.5^\circ$. Nine different repetitions were performed for each speed and included in the figures, demonstrating the repeatability of the acoustic measurements in this facility. Simulated quadrupole (U_{ref}^8) and dipole (U_{ref}^6) results are included for reference.	48
3.3	Far-field sound directivity pattern for the background (smooth wall) configuration, shown for $U_{ref} = 50$ m/s. Note that the streamwise array of eight microphones has a constant $R=578$ mm radius. (a-b) Far-field spectra as a function of stream- and spanwise observer angle, respectively. (c-d) Integrated spectra ($f_0 = 700$ Hz to $f_1 = 20000$ Hz) as a function of stream- and spanwise observer angles, respectively. Angles are consistent with the coordinate systems defined in figure 2.9.	49
3.4	Clean wall (solid) and untreated trailing edge (dash-dot) far-field sound spectra are shown for all measured speeds. The legend shows the colors corresponding to each speed. The microphone is at $\theta = 123.5^\circ$	51

3.5	Signal-to-Noise ratio using the untreated trailing edge and background noise levels in the (a) streamwise direction, and (b) spanwise direction. Levels are shown for $U_j = 50$ m/s	51
3.6	Comparison of measured, background-subtracted far-field noise spectra (x) and a BPM prediction [4] for turbulent boundary layer-trailing edge noise (TBL-TE, dotted line) and trailing edge bluntness-vortex shedding noise (TEBVS, dash-dot) at $\alpha = 0^\circ$ for (a) $U_{ref} = 40$ m/s, (b) $U_{ref} = 50$ m/s, (c) $U_{ref} = 60$ m/s. Additional simulation inputs are given in table 3.1.	53
3.7	Background-subtracted trailing edge noise as a function of U_{ref} , measured with the microphone at $\theta = 123.5^\circ$. Data presented only where the signal-to-noise ratio exceeds 2 dB.	55
3.8	Background-subtracted far-field sound spectra for the untreated trailing edge, measured by the stream-wise microphone at $\theta = 123.5^\circ$	57
3.9	Far-field directivities in the (a) streamwise, and (b) spanwise directions for $U_{ref} = 50$ m/s. Spectra have been background-subtracted and are only shown where signal-to-noise ratio is greater than 2 dB.	57
3.10	Background subtracted far-field sound spectra for the mock trailing edge with and without Baseline, Thick, and Dense finlets applied, measured at $\theta = 123.5^\circ$. Data is only shown where the signal-to-noise ratio exceeds 2 dB. (a) $U_{ref} = 40$ m/s, (b) $U_{ref} = 50$ m/s, (c) $U_{ref} = 60$ m/s, (d) Relative treatment geometries, shown as side view (flow direction denoted by arrow) and rear view (flow is directed out of page). Dimensions given in figure 2.3	58
3.11	Signal-to-Noise Ratio (SNR) and background-subtracted SPL spectra at $U_{ref} = 50$ m/s for the trailing edge (T.E.) with Baseline finlets applied. Background-subtracted spectra are only shown for SNR > 2 dB. (a) SPL in the streamwise array, (b) SPL in the spanwise array, (c) SNR in the streamwise array, (d) SNR in the spanwise array.	60
3.12	Signal-to-Noise Ratio (SNR) and background-subtracted SPL spectra at $U_{ref} = 50$ m/s for the trailing edge (T.E.) with Thick finlets applied. Background-subtracted spectra are only shown for SNR > 2 dB. (a) SPL in the streamwise array, (b) SPL in the spanwise array, (c) SNR in the streamwise array, (d) SNR in the spanwise array.	61
3.13	Signal-to-Noise Ratio (SNR) and background-subtracted SPL spectra at $U_{ref} = 50$ m/s for the trailing edge (T.E.) with Dense finlets applied. Background-subtracted spectra are only shown for SNR > 2 dB. (a) SPL in the streamwise array, (b) SPL in the spanwise array, (c) SNR in the streamwise array, (d) SNR in the spanwise array.	62

3.14	<p>(a) Mean velocity profiles, normalized on the corresponding jet velocity, showing the effect of the transition ramp-mock trailing edge piece. Probe was in the $x - y$ plane at $x = 1398$ mm, $x = 1398$ mm, and $x = 1400$ mm (\circ, \square, and \mathbf{x}, respectively). Trailing edge location is shown with a dashed line. (b) Untreated trailing edge profiles normalized on U_m and $y_{1/2}$. The wall jet is self-similar, consistent with measurements in this facility presented Clark [5] and Devenport <i>et al.</i> [6] in this facility. (c) Turbulence intensity profiles showing the effect of the transition ramp-mock trailing edge. The root-mean-square of the fluctuations, u', was computed by integrating the turbulence spectra up to 7 kHz, as described in section 2.5.2. (d) Turbulence intensities plotted versus $y/y_{1/2}$, in agreement with those presented by Devenport <i>et al.</i> [6].</p>	65
3.15	<p>(a) Mean velocity profiles for the treated and untreated trailing edge cases, expressed as a percentage of U_j and plotted through the full wall jet region. (b) Turbulence intensity profiles for the treated and untreated trailing edge cases, plotted through the full wall jet region. Note that the turbulence intensity was found by integrating the spectra (section 3.2.3) up to 8 kHz.</p>	66
3.16	<p>Normalized mean velocity profiles U/U_j for the treated and untreated trailing edge, measured at $x = 1400 \pm 1$ mm, $z = 0 \pm 0.25$ mm. Shaded areas represent the 95% confidence intervals. Horizontal lines indicate maximum treatment height. Legends are inset in figures a-e. (f) Relevant treatment geometries.</p>	67
3.17	<p>(a) Shear layer near the top of the Baseline treatment in figure 3.16a. Legend given in figure 3.16a. (b) Corresponding velocity gradient, with zero marked by the vertical line.</p>	68
3.18	<p>(a) Shear layer near the top of the Thick treatment in figure 3.16b. Legend is shown in figure 3.16b. (b) Corresponding velocity gradient, with zero marked by the vertical line.</p>	68
3.19	<p>(a) Shear layer near the top of the Short treatment. Legend is shown in figure 3.16c. (b) Corresponding velocity gradient, with zero marked by the vertical line.</p>	68
3.20	<p>(a) Shear layer near the top of the Rail treatment. Legend is shown in figure 3.16e. (b) Corresponding velocity gradient, with zero marked by the vertical line.</p>	69
3.21	<p>(a) Shear layer near the top of the Dense treatment. Legend is shown in figure 3.16d. (b) Corresponding velocity gradient, with zero marked by the vertical line.</p>	69

3.22	Comparison of normalized mean velocity profiles U/U_j between modified treatments and the Baseline finlet treatment applied to the trailing edge. Probe location is scaled on the treatment height, h . (a) Baseline and Short finlets, (b) Baseline and Thick finlets, (c) Baseline finlets and Rails, (d) Baseline and Dense finlets.	70
3.23	Treated and untreated trailing edge turbulence intensities, measured at $x = 1400 \pm 1$ mm, $z = 0 \pm 0.25$ mm. Shaded areas indicate the 95% confidence interval. Horizontal line indicates maximum treatment height. Legends are inset in figures a-e. (f) Relevant treatment geometries.	72
3.24	Change in power spectral densities (units of dB/Hz) with the treatments applied. Vertical axis is the normalized probe location using the maximum treatment height, h . Horizontal axis is the frequency, up to 7 kHz. Color indicates magnitude of the change. Grayed areas contain no data.	75
3.25	Streamwise flow development along the Baseline finlets, comparing data measured at the “mid-plane” of the Baseline treatment with results for the untreated trailing edge and trailing edge with the full Baseline finlets applied. Influence is shown for (a) mean velocity, normalized on U_j , and (b) turbulence intensity, found by integrating the turbulent spectra up to 7000 Hz, for reasons given in section 2.5.2. (c) Corresponding treatment geometry	80
3.26	Comparison of mean velocity, (a) , and turbulence intensity, (b) , as a function of normalized probe location, \tilde{y}/h , where h is the maximum height of the applied treatment.	81
3.27	(a) Shear layer near the top of the Baseline and Baseline mid-plane treatments (see figure 3.25c), (b) Corresponding velocity gradient, with zero marked by vertical dotted line. Legend given in figure 3.25.	81
3.28	Change in power spectral density (units of dB/Hz) with the mid-plane Baseline finlet treatment applied. Vertical axis is normalized on maximum treatment height, h . Horizontal axis is the frequency up to 7 kHz. Color indicates magnitude of the change. Grayed areas contain no data.	82
3.29	Surface pressure spectra variation in the streamwise direction for the untreated trailing edge. Each row represents a different speed ($U_{\text{ref}} = 40, 50, \text{ and } 60$ m/s). Each column represents a different frequency range (left to right, 100-1,000 Hz, 1,000-10,000 Hz, and 10,000-20,000 Hz). Within each figure, the different symbols denote different, streamwise-aligned microphone positions.	85

3.30	Surface pressure spectra variation in the streamwise direction for the trailing edge with Baseline finlets applied. Each row represents a different speed ($U_{\text{ref}} = 40, 50, \text{ and } 60 \text{ m/s}$). Each column represents a different frequency range (left to right, 100-1,000 Hz, 1,000-10,000 Hz, and 10,000-20,000 Hz). Within each figure, the different symbols denote different, streamwise-aligned microphone positions.	86
3.31	Surface pressure spectra variation in the streamwise direction for the trailing edge with Thick finlets applied. Each row represents a different speed ($U_{\text{ref}} = 40, 50, \text{ and } 60 \text{ m/s}$). Each column represents a different frequency range (left to right, 100-1,000 Hz, 1,000-10,000 Hz, and 10,000-20,000 Hz). Within each figure, the different symbols denote different, streamwise-aligned microphone positions.	87
3.32	Surface pressure spectra variation in the spanwise direction for the untreated trailing edge. Each row represents a different speed ($U_{\text{ref}} = 40, 50, \text{ and } 60 \text{ m/s}$). Each column represents a different frequency range (left to right, 100-1,000 Hz, 1,000-10,000 Hz, and 10,000-20,000 Hz). Within each figure, the different symbols denote different, spanwise-aligned microphone positions.	88
3.33	Surface pressure spectra variation in the spanwise direction for the trailing edge with Baseline finlets applied. Each row represents a different speed ($U_{\text{ref}} = 40, 50, \text{ and } 60 \text{ m/s}$). Each column represents a different frequency range (left to right, 100-1,000 Hz, 1,000-10,000 Hz, and 10,000-20,000 Hz). Within each figure, the different symbols denote different, spanwise-aligned microphone positions.	89
3.34	Surface pressure spectra variation in the streamwise direction for the untreated trailing edge (first row), trailing edge with Baseline finlets applied (second row), and trailing edge with Thick finlets applied (third row), measured at a jet speed of $U_{\text{ref}} = 60 \text{ m/s}$. Each column represents a different frequency range (left to right, 100-1,000 Hz, 1,000-10,000 Hz, and 10,000-20,000 Hz). Within each figure, the different symbols denote different, streamwise-aligned microphone positions.	90
3.35	Surface pressure spectra variation in the spanwise direction for the untreated trailing edge (first row) and trailing edge with Baseline finlets applied (second row), measured at a jet speed of $U_{\text{ref}} = 60 \text{ m/s}$. Each column represents a different frequency range (left to right, 100-1,000 Hz, 1,000-10,000 Hz, and 10,000-20,000 Hz). Within each figure, the different symbols denote different, spanwise-aligned microphone positions.	91

3.36	Surface pressure spectra at various streamwise positions, shown for $100 \leq f \leq 1,000$ Hz. a-d) Positions 9-7, 4, e) Top view (flow direction indicated with arrow) of relative surface pressure fluctuation microphone positions used in the experiment.	92
3.37	Surface pressure spectra at various streamwise positions, shown for $1,000 \leq f \leq 10,000$ Hz. a-d) Positions 9-7, 4, e) Top view (flow direction indicated with arrow) of relative surface pressure fluctuation microphone positions used in the experiment.	93
3.38	Surface pressure spectra at various streamwise positions, shown for $10,000 \leq f \leq 20,000$ Hz. a-d) Positions 9-7, 4, e) Top view (flow direction indicated with arrow) of relative surface pressure fluctuation microphone positions used in the experiment.	94
3.39	Surface pressure spectra at various spanwise positions, shown for $100 \leq f \leq 1,000$ Hz. Relative microphone positions are shown in figure 3.38e.	95
3.40	Surface pressure spectra at various spanwise positions, shown for $1,000 \leq f \leq 10,000$ Hz. Relative microphone positions are shown in figure 3.38e.	96
3.41	Surface pressure spectra at various spanwise positions, shown for $10,000 \leq f \leq 20,000$ Hz. Relative microphone positions are shown in figure 3.38e.	97
3.42	Coherence between streamwise pairs of surface pressure fluctuation microphones. a) Positions 4-9, $\Delta x = 57.15$ mm, b) Positions 4-8, $\Delta x = 38.1$ mm, c) Positions 4-7, $\Delta x = 19.05$ mm, d) Top view (flow direction indicated with arrow) of relative positions surface pressure fluctuation microphone positions used in the experiment.	98
3.43	Coherence between spanwise pairs of surface pressure fluctuation microphones. a) Positions 5-4, $\Delta z = 13.27$ mm, b) Positions 5-3, $\Delta z = 27.44$ mm, c) Positions 5-2, $\Delta z = 45.72$ mm, d) Positions 5-1, $\Delta z = 50.3$ mm, d) Top view (flow direction indicated with arrow) of relative positions surface pressure fluctuation microphone positions used in the experiment.	99

List of Tables

- 2.1 VT Anechoic Wall Jet Power Law Coefficients [5] 21
- 2.2 Smooth wall boundary layer parameters, $x= 1397$ mm. Measured values, to the left of the break, were averaged over 41 experimental runs at each speed. Estimated values, using Re_x Wagnanski’s relations (equations 2.1-2.5, table 2.1) are right of the break. 22
- 2.3 Treatment Design Parameters 41
- 2.4 Experiment test plan, showing the test cases, jet speeds at which data was taken, and positions of surface pressure instrumentation, referencing figure 2.5b. 45
- 3.1 Brooks, Pope, and Marcolini [4] trailing edge noise (TBL-TE and TEB-VS) prediction parameters. 52
- 3.2 Brooks, Pope, and Marcolini [4] Predicted Peak Frequencies. 52
- 3.3 Transition ramp effects on the boundary layer parameters, $x = 1397$ mm, $U_{ref} = 50$ m/s. Untreated trailing edge values are measured relative to the step surface. 64
- 3.4 Mean width and standard deviation of the 95% confidence intervals on mean velocity, U/U_j , and turbulence intensity, u'/U_m shown in figures 3.16a-3.16d. . 66
- 3.5 Boundary layer properties for the treated and untreated cases. 69
- 3.6 Estimates of the mixing layer frequency, f_M , and starting/ending locations in terms of the maximum treatment height, h 74
- 3.7 Comparison of boundary layer properties for the trailing edge treated with Baseline finlets, Baseline finlets at mid-plane, and Short finlets. 79

Chapter 1

Introduction

1.1 Background

Trailing edge noise is seen in a variety of applications, making this a problem of interest in the research community. During aircraft landings, when the engines are operated at low power settings, trailing edge noise can be an important component of the overall noise. Another prevalent situation is during the operation of wind turbines. Trailing edge noise is the dominant sound source as air flows over wind turbine blades, causing annoyance for surrounding communities. As a result, governments have imposed local regulation to mitigate wind turbine noise, placing an artificial constraint on power generation. For example, a 3-decibel noise reduction may correspond to a 15% increase in the wind turbine tip speed, an important parameter in determining wind turbine efficiency. In these situations, aeroacoustic effects must be considered during the design process, and noise-reducing technologies play an important role. Recently, researchers have begun to take inspiration from the silent flight of owls, trying to replicate the features in their feathers to create practical trailing edge treatments. The work described in this thesis is built on a foundation of experiments inspired by the downy canopy of owl feathers, described in detail by Clark *et al.* [1, 2, 7], which demonstrated the great potential for trailing edge noise reduction. However, as no flow measurements had been performed, it was difficult to identify the underlying physics responsible for the noise reduction, a significant knowledge gap that will be addressed in the following chapters.

The goals of this thesis are to clearly quantify the local aerodynamic effects of the bio-inspired noise treatments and relate those aerodynamics to any reduction in trailing edge noise. This was done through a series of wind tunnel tests with a mock trailing edge immersed in a wall jet, with and without the bio-inspired treatments applied. The results appear to be representative of a phenomenon known as “shear sheltering”. The remainder of Chapter 1 includes the specific details of silent owl flight that inspired the treatments, as well as a brief intro-

duction to trailing edge noise theory and experimental validation, and a review of existing trailing edge noise control techniques, focusing on the owl-inspired treatments developed by Clark *et al.* [1, 2, 7]. Chapter 2 describes the experimental methods, Chapter 3 includes the experimental results and discussion, and Chapter 4 presents some final conclusions regarding the physics responsible for the noise attenuation and treatment design considerations.

1.2 Inspiration from Biology- The Silent Flight of Owls

In 1934, Graham [8] identified three main features of owl feathers that he believed were responsible for their silent flight: a leading edge comb, trailing edge fringe, and downy upper surface. Graham hypothesized that the comb may reduce the sharp pressure difference near the leading edge by creating what he called a “wash-out” effect, deflecting the local incoming flow direction. He believed this effect would be most pronounced on the downstroke of flapping flight. In the case of the trailing edge fringe, the flow was thought to be smoothed so that as it passes over and through the wing tips there would be a lower tendency to form noisy turbulent structures. A secondary effect might be to prevent the local fluttering of the trailing edge feathers, which would also create noise. Not much attention was given to the role of the downy canopy in silent owl flight, but he suggested the canopy may serve the purpose of either muffling reverberations from the leading edge or continuing the local flow retardation that the leading edge comb induces.

About 30 years later, Thorpe *et al.* [9] noticed that the flapping motion of small birds was generating ultrasonic noise, which raised an interesting question in the context of silent owl flight. Does owl flight create noise at higher frequencies, above the normal upper limit of human hearing? If so, the supposed anatomical advantages of owl feathers would be lost, at least from a biological perspective, since the majority of small mammals preyed on by owls have good hearing in the ultrasonic region. However, the tests they conducted showed that the owl flapping was also silent at high frequencies. Kroeger *et al.* [10] followed this up with an extensive flyover experiment and wind tunnel study of owl wings, again motivated by possible applications to airframe noise. They found that the leading edge comb acts like a vortex sheet generator, which promotes attached laminar flow near the leading edge.

A critique of these owl-based studies may be that the silent flight is due to the low flight speed, not necessarily the unique features of owl feathers. This was addressed by Sarradj *et al.* [11], who performed flyover measurements with different bird species having similar flight speeds, including owls and “nonquietly flying” birds of prey, and found that the owls were indeed up to 8 dB quieter than the other species. This confirmed the hypothesis that silent owl flight is attributed to the low flight speed *and* the plumage features.

Lilley [12] did a thorough job interpreting the available experimental data [10, 13] and observations of owl anatomy [8] in the context of aeroacoustics, resulting in new insights on silent owl flight with practical engineering implications. The flyover measurements of

Kroeger *et al.* [10] were conducted at a Reynolds number of about 1.5×10^5 , meaning laminar separation would be expected near the leading edge of the wing. The leading edge comb on the feathers appeared to stabilize the wing, creating a “pseudo-turbulent” flow. This was confirmed by the poor flight performance of an owl with the leading edge comb removed. The vortex sheets created by the leading edge comb seemed to control separation and create streamwise vortices over the upper surface of the owl wing, reducing the boundary layer thickness along the entire chord. Lilley’s conclusion in regards to the leading edge comb was that it does contribute to the noise reduction by reducing the volume of turbulence scattering off of the trailing edge. He also hypothesized that the trailing edge fringe appeared to act as a “serrated” trailing edge, reducing the scattering efficiency (and thus, the radiated noise) of the edge. This technique for noise reduction was formally introduced by Howe [14], and will be discussed along with other noise control strategies in section 1.5.

1.2.1 Flow Effects due to a Canopy- Motivation for Finlets and Rails

Based his analysis, Lilley [12] hypothesized that the leading edge comb and trailing edge were not enough to account for the silent flight of the owl. He then focused on closely examining the features of the downy, velvet-like canopy on the owl wing. Starting from the assumption that the owl has a mechanism for eliminating high frequency noise (shown by Thorpe *et al.* [9]), Lilley suggested that the downy canopy must be a bypass mechanism for dissipation of turbulent energy at frequencies smaller than the ones associated with viscous dissipation, leading to a sound spectrum nearly cut-off in frequencies above 2 kHz.

Lilley’s analysis showing that the downy canopy was likely the main driver of silent flight served as motivation for using bio-inspired canopies for the reduction of roughness noise, particularly as presented recently by Clark *et al.* [7]. The findings described by Clark *et al.* served as the initial motivation for the development of the bio-inspired devices described here. They tested fabric canopies over a variety of rough surfaces. The canopies tended to work well at attenuating pressure fluctuations in the rough surfaces, up to 30 dB in some cases. The far-field noise results were mixed; however, it was noted that the far-field noise increased when the fabric had cross-threads at increasing angles relative to the flow direction. This led to the development of unidirectional canopies, whose fibers ran parallel to the flow. The surface pressure attenuation was still high, up to about 25 dB in some cases, and reductions of up to 6 dB in the far-field sound pressure levels were reported for higher frequencies and speeds.

The most important conclusions presented by Clark *et al.* [7] were the discovery of significant attenuation of surface pressures and their mixing-layer hypothesis as a model for surface pressure reduction. In regards to the surface pressure attenuation, Clark *et al.* reported that the smallest spacing between fibers was the most effective, possibly because the spacing limits the scale of eddies that can penetrate the canopy. The attenuation seems to develop as

it moves downstream, a feature that was attributed to pseudo-viscous damping influencing the flow. The underlying mechanism governing the surface pressure attenuation, and consequently the far-field sound attenuation, was hypothesized to be the following: the canopy induced a mixing layer, leading to unstable, nascent turbulent eddies that are lifted higher above the surface than they would have been without the canopy. This increased stand-off from the wall could then lead to a reduced pressure footprint. These findings would play a significant role in the later work by Clark *et al.* [1, 2].

As part of the mathematical modeling of this mixing layer aimed at recovering the experimental trends, Clark *et al.* presented a dispersion relation dependent on a nondimensionalized boundary layer thickness, nondimensionalized frequency, and canopy open-area ratio. Although the predicted surface pressure attenuation did not fully match the experimental data, it appears to capture the main physics well, and is certainly worth considering further. Indeed, such a mechanism may be responsible for the results presented in subsequent chapters.

The experimental findings presented in Clark *et al.* [7] led researchers to create the novel trailing edge control devices (termed “rails” and “finlets”) on which this thesis is based on. The early development of these rails and finlets is discussed in detail in section 1.6.

1.3 Fundamentals of Trailing Edge Noise Theory

Broadly, the self-noise of an airfoil can be classified into five categories: trailing edge bluntness-vortex shedding, tip vortex formation, laminar boundary layer-vortex shedding, separation-stall noise, and *turbulent boundary layer-trailing edge noise*, which is the source of interest here. The key features of these categories of airfoil self-noise are described in detail by Brooks, Pope, & Marcolini [4]. The turbulent boundary layer-trailing edge noise, which is the dominant source of wind turbine noise, is attributed to unsteady pressure fluctuations in the turbulent boundary layer being scattered by the trailing edge. For the remainder of this thesis, the phrase “trailing edge noise” refers specifically to turbulent boundary layer-trailing edge noise unless otherwise stated. A brief discussion on the relevant theory is given here to contextualize the description of existing trailing edge noise control techniques, as well as provide some insight into how the finlets and rails may be able to reduce trailing edge noise.

Trailing edge noise occurs when the coherent structures in a turbulent boundary layer are scattered by the trailing edge (see figure 1.1). With the development of Lighthill’s aeroacoustic analogy in 1952 [15], researchers had a strong foundation for studying practical acoustic problems like trailing edge noise.

The development of trailing edge noise theories started with Ffowcs-Williams and Hall in 1970 [16], who solved Lighthill’s equation to develop an analytical expression for the far-field sound spectrum produced by a semi-infinite, flat, swept plate in a uniform flow. By assuming a cylindrical eddy of radius δ centered on the edge, the far-field sound intensity was found

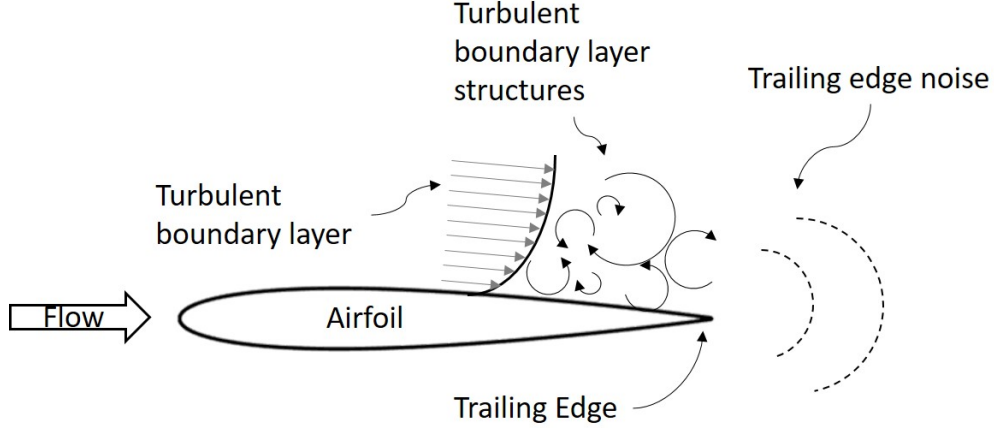


Figure 1.1: Idealized schematic of turbulent boundary layer-trailing edge noise.

to be proportional to the fifth power of the velocity, shown in equation 1.1. Here, ρ is the fluid density, U is the freestream velocity, c is the speed of sound, and R is the distance between the source and field points. In this case, δ can also be thought of as the turbulence lengthscale.

$$I \sim \rho U^3 \left(\frac{U}{c} \right)^2 \frac{\delta^2}{R^2} \quad (1.1)$$

This result suggests that the trailing edge noise scales on the fifth power of the velocity, and that the noise may be reduced by decreasing the turbulence lengthscale or moving turbulent sources away from the edge, e.g. decreasing δ or increasing R in equation 1.1. This was the first example given of a U^5 dependence for trailing edge noise, which is considerably different than that of an eddy far from the edge, which has the same U^8 dependence as free turbulence. Additionally, much work in the area of trailing edge noise control (discussed further in the following section) is based on the idea of reducing the turbulence lengthscale. Lastly, in the development of equation 1.1, Ffowcs Williams and Hall [16] showed that trailing edge noise has a cardioid directivity, emanating primarily in the upstream direction, with the cardioid cusp on the trailing edge.

Following this work, Amiet [17] proposed a theory to predict the trailing edge noise that would use the upstream wall pressure fluctuation spectra and an airfoil response function. This was done under the assumptions that the turbulence is statistically stationary as it moves past the trailing edge, and that a given surface pressure fluctuation frequency, ω , has a single value for the convection velocity, U_c , and wavenumber, K_x . Equation 1.2 gives the far-field sound spectrum, S_{pp} , for an overhead observer, where the parameters of interest in this discussion are the spanwise lengthscale, $l_y(\omega)$, and the surface pressure spectrum, $S_{qq}(\omega, 0)$. The term \mathcal{L} is a generalized lift function, and the remaining terms are geometric

parameters (excepting the angular frequency, ω). It is worth noting that Amiet provided an updated correction to this lift function two years later [18]. The key point of this discussion of Amiet’s theory is that: by measuring the surface pressure spectrum and associated spanwise lengthscale, one can adequately predict the far-field sound spectrum. This is an advancement over the sound pressure spectrum formulation by Ffowcs-Williams and Hall [16], which required knowing the two-point velocity spectrum near the edge, an impractical quantity to measure. The last observation to be made regarding Amiet’s theory is that the expression for the far-field spectrum can be manipulated such that the result is consistent with the findings by Ffowcs-Williams and Hall [16], including the cardioid directivity.

$$S_{pp}(x, 0, z, \omega) = \left(\frac{\omega b z}{2\pi c_0 \sigma^2} \right)^2 l_y(\omega) d|\mathcal{L}|^2 S_{qq}(\omega, 0) \quad (1.2)$$

$$l_y(\omega) = \frac{1}{S_{qq}(\omega, 0)} \int_0^\infty S_{qq}(\omega, y) dy \quad (1.3)$$

1.4 Experimental Validation of Trailing Edge Noise Theory

Some years later, Brooks, Pope, & Marcolini [4] measured the self-noise of airfoils over a large range of conditions and developed empirical correlations that are widely used as prediction tools. For completeness, a brief review of their findings is given here. Aerodynamic and aeroacoustic measurements were performed on NACA 0012 with varying chords and trailing edge thicknesses for freestream velocities up to 71.3 m/s. The airfoils were tested for angles of attack (α) between zero degrees and 25.2 degrees in both heavily tripped and untripped cases. Aerodynamic measurements were carefully performed to characterize the boundary layer parameters (boundary layer thickness, δ , displacement thickness, δ^* , and momentum thickness, θ). Based on the measured data, curve fits were given to estimate these parameters as functions of chord-based Reynolds number (Re_c) at $\alpha = 0^\circ$, denoted by the subscript 0. Expressions were given for the nondimensional parameters δ_0/c , δ_0^*/c and θ_0/c as functions of chord-based Reynolds number Re_c for the tripped and untripped cases. When $\alpha \neq 0^\circ$, the suction and pressure side thicknesses (subscripts s and p, respectively) can be estimated using the $\alpha = 0^\circ$ values and the nonzero angle. One can also directly specify the displacement thickness based on simulations or experiments.

The acoustic data they present was “edited” carefully to only examine trailing edge noise (details of the editing process were given in their appendix [4]). The spectra, corrected for shear layer diffraction and trailing edge noise directivity, were then presented as 1/3-octave Sound Pressure Levels (SPL) for every angle of attack and freestream combination. The data were used to establish scalings that were crucial for developing the prediction methods that form the key contribution of the paper and are often used in research today. The total

predicted SPL in a 1/3-octave form is:

$$SPL_{TOT} = 10 \log \left(10^{SPL_\alpha/10} + 10^{SPL_s/10} + 10^{SPL_p/10} \right) \quad (1.4)$$

This form captures the effects of the different boundary layer properties on the suction and pressure sides at varying angles of attack (SPL_s and SPL_p), as well as noise attributed to separation at higher angles of attack (SPL_α).

The pressure and suction side contributions can be decomposed as follows:

$$SPL_p = 10 \log \left(\frac{\delta_p^* M^5 L \bar{D}_h}{r} \right) + A \left(\frac{St_p}{St_1} \right) + (K_1 - 3) + \Delta K_1 \quad (1.5)$$

$$SPL_s = 10 \log \left(\frac{\delta_s^* M^5 L \bar{D}_h}{r} \right) + A \left(\frac{St_s}{St_1} \right) + (K_1 - 3) \quad (1.6)$$

In the first term, M is the freestream Mach number, L is the wetted span, r is the observer distance from the trailing edge, and $\bar{D}_h(\Theta, \Phi)$ is the (cardioid) directivity function dependent on the angle measured from the upstream chordline, Θ , and the lateral angle Φ . The second term makes use of the 1/3-octave spectral shape, modeled as a shape function A , which depends on the pressure side Strouhal number, $St = f \delta_p^* / U$, and an estimated peak Strouhal number, St_1 , corresponding to the maximum scaled SPL value. The $(K_1 - 3)$ term is included to capture the peak scaled SPL value, corresponding to St_1 . The ΔK_1 term is used to adjust the pressure side contribution at nonzero angles of attack.

The separation noise term can be decomposed as follows, where B , K_2 , and St_2 are analogous to A , K_1 , and St_1 . These predictions can be (and have been) used for non- NACA 0012 cases, but care must be taken when interpreting those results, as this method is semi-empirical with 0012 data.

$$SPL_\alpha = 10 \log \left(\frac{\delta_s^* M^5 L \bar{D}_h}{r} \right) + B \left(\frac{St_s}{St_2} \right) + K_2 \quad (1.7)$$

A similar procedure was done for trailing edge bluntness- vortex shedding noise, pictured in figure 1.2. The predicted SPL spectrum in 1/3-octave form is given in equation 1.8.

$$SPL_{BLUNT} = 10 \log \left(\frac{h M^{5.5} L \bar{D}_h}{r^2} \right) + G_4 \left(\frac{h}{\delta_{avg}^*}, \Psi \right) + G_5 \left(\frac{h}{\delta_{avg}^*}, \Psi, \frac{St'''}{St'''}_{peak} \right) \quad (1.8)$$

Here, h is the trailing edge thickness, and Ψ is the solid angle, in degrees, between the sloping surfaces upstream of the trailing edge. Note that for a flat plate, $\Psi = 0^\circ$, and for a

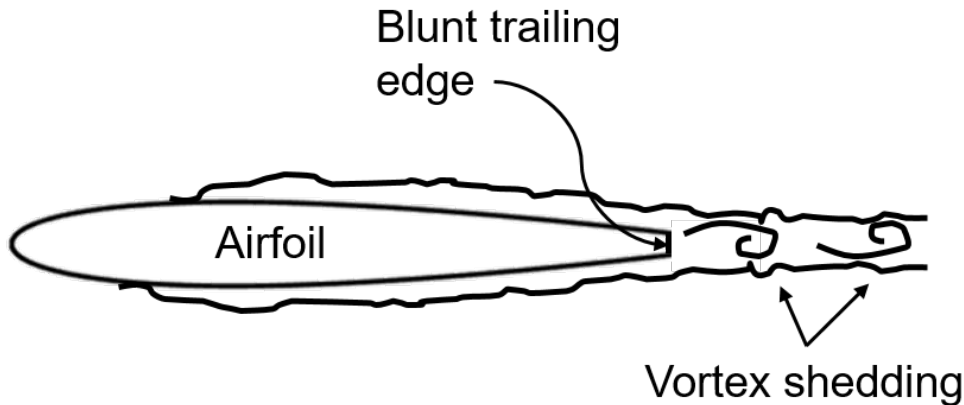


Figure 1.2: Idealized schematic of trailing edge bluntness - vortex shedding noise.

NACA 0012 airfoil, $\Psi = 14^\circ$. Brooks, Pope, and Marcolini used the notation $St''' = fh/U$ to distinguish the Strouhal number using trailing edge thickness from the definition given earlier for turbulent boundary layer-trailing edge noise, which used the displacement thickness as the lengthscale. Similarly, St'''_{peak} is an estimate of what the peak Strouhal number should be based on Ψ, h , and the average displacement thickness on both sides of the airfoil, δ_{avg}^* . This is analogous to the terms St_1 and St_2 defined previously. Similarly, G_4 is a model to determine the peak power spectral density, analogous to K_1 , and G_5 is a model to estimate the power spectral density shape, analogous to A .

1.5 Trailing Edge Noise Control

Numerous experimental and theoretical studies have been done to develop ways to reduce trailing edge noise. Trailing edge blowing is one such method that was examined as early as 1973 by Scharton, Pinkel, and Wilby [19]. Modifying the physical geometry of the edge to reduce the span-wise correlation of incoming turbulence is another common technique. This can be accomplished with a serrated trailing edge, for example. Howe [14] gave a concise theoretical model to predict the trailing edge noise attenuation based on the geometry of the serrations. Starting his analysis with a flat plate of zero angle of attack, he showed that the frequency spectrum of the noise could be reduced by $10 \log_{10} \left(\frac{Ch}{\lambda} \right)$ dB, where h is the serration amplitude, λ is the span-wise wavelength, and C is a constant approximately equal to 10. For the ratio $h/\lambda \approx 1$, Howe predicted attenuation of approximately 8 dB. Experimental studies on trailing edge serrations have found the attenuation to be closer to 3-4 dB [20].

Another area of interest in trailing edge noise reduction is the idea of porous trailing edges. Herr *et al.* [21] describe the development of a database to identify the underlying mechanisms

and scaling laws for the attenuation provided by porous, brush-type extension. Their findings suggest that the attenuation may be attributed to the viscous damping of the pressure fluctuations in the turbulent boundary layer. They also found that the trailing edge noise spectra scale better on the fifth power of velocity and with Strouhal number based on the chord length, rather than the standard displacement thickness approach. Geyer *et al.* [22] conducted a thorough experiment on the performance of porous airfoils (not just the trailing edge) and found that up to 10 dB of attenuation in the low- to mid-frequencies is possible. The attenuation is a strong function of the material flow resistivity.

These existing methods are typically aimed at reducing the scattering efficiency of the physical trailing edge, by introducing serrations or porous materials. In essence, these can be thought of as ways to either decrease the magnitude of the pressure fluctuations (for example, through viscous damping with porous materials), or the spanwise lengthscale. As shown in section 1.3, both of these approaches should result in decreased far-field sound levels. However, the existing methods can be difficult to implement and require careful design to avoid hurting the intended aerodynamic performance. An alternative approach that could achieve similar noise reductions to existing technologies without changing the physical airfoil edge would be desirable.

1.6 Bio-Inspired Finlets and Rails

This is the approach taken by Clark *et al.* [1, 2, 23], by developing devices that manipulate the incoming boundary layer as an owl wing might. In section 1.2, the canopy work of Clark *et al.* [7] was discussed, where it was shown that the owl-inspired canopies realized 25 to 30 dB attenuation of the surface pressure fluctuations. Based on these findings, novel surface treatments were designed to replicate the unidirectional canopies in a practical manner for an airfoil. The idea was that, based on trailing edge noise theory (see section 1.3 for a brief review), if the surface pressures near an airfoil trailing edge could be similarly reduced, there will be a corresponding decrease in trailing edge noise. This section gives a review of trailing edge noise control studies directly related to the owl-inspired finlets and rails.

1.6.1 Pilot Study- Clark *et al.* [1]

In the pilot study, over 20 different designs were tested, and the most effective ones provided up to 10 dB of noise reduction. This thorough experiment sparked a new line of inquiry in trailing edge noise control techniques. The measurements were made in the Virginia Tech Stability Wind Tunnel Anechoic Configuration, with tensioned Kevlar sidewalls that contain the bulk flow and allow sound to pass through to port and starboard anechoic chambers, where microphones could be placed. A standard DU96-W180 wind turbine airfoil was used, with trip tape applied to the 5% and 10% chord locations on the suction and pressure sides,

respectively. Sound measurements were made with a 117-channel phased microphone array, which allows for beamforming processing methods. Results were presented for a freestream of 60 m/s, or a chord Reynolds number of 3 million. For all treatments, far-field sound and lift measurements were made at angles of attack between -4 and 16 degrees, including the zero-lift angle (-2.5 degrees) and stall (approximately 11 degrees). Treatments were applied to both sides of the airfoil unless otherwise noted.

Figure 1.3 shows a schematic of the bio-inspired “finlets” and “rails” tested by Clark *et al.* [1]. The treatments were additively manufactured on a substrate faired to the trailing edge surface with thin metal tape. The treatments were designed to mimic the unidirectional canopies [7] as closely as possible, with the cylindrical rail elements more closely replicating the fibers. Because of the geometric complexity of the rails, as well as their comparable performance to the finlets, the ensuing literature focused mainly on finlets. They focused on varying the distance from the airfoil surface to highest point on the treatment (height), wall-to-wall distance between adjacent treatments (spacing), individual protrusion thickness, and distance from the airfoil edge to the end of the treatment (extension). The parameters are similarly defined in this thesis (see chapter 2, figure 2.17). A useful parameter not explicitly given is the leading edge angle, defined as Λ in equation 1.9, where h is the maximum treatment height and L_h is the distance from the leading edge of the treatment to the location of maximum height. The leading edge angle as defined here gives a measure of the “abruptness” of the geometric change the flow must travel across, and was one of the parameters varied during the experiments described in chapters 3 and 4. In Clark *et al.* [1], the following leading edge angles were tested: $\Lambda = 1.1, 2.3, 2.5, 4.5,$ and 9.9 degrees.

$$\tan \Lambda = h/L_h \quad (1.9)$$

The baseline finlet they tested (4 mm spacing, 4 mm height, 0.5 mm thickness, 0.5 mm substrate, 10 mm extensions, $\Lambda = 2.3$ degrees) had no detrimental effect on the airfoil lift, and actually increased the lift slightly at post-stall angles of attack. The acoustic results were presented for unstalled attack angles from -2.5 degrees (zero lift) to 6.9 degrees, as no difference was noted post-stall. At the zero-lift angle, beamform maps at 3 kHz showed reductions in trailing edge noise of up to 10 dB relative to the untreated case. The corresponding integrated spectra showed reductions starting at approximately 2 kHz and continuing up to 5 kHz. The noise reduction was hypothesized to be due to a reduction in surface pressure fluctuations, much like the canopies, and a decrease in the spanwise correlation lengthscale. Of note is the fact that *all* the variants on the baseline finlet had similar or better trailing edge noise attenuation. The following parametric considerations were observed:

- **Spacing.** Generally, the attenuation increased as the finlet spacing decreased. This is consistent with the expectation that the spacing essentially limits the maximum possible spanwise correlation lengthscale. There appeared to be a lower limit at which the finlets began to act as a blunt trailing edge. This limit was believed to exist

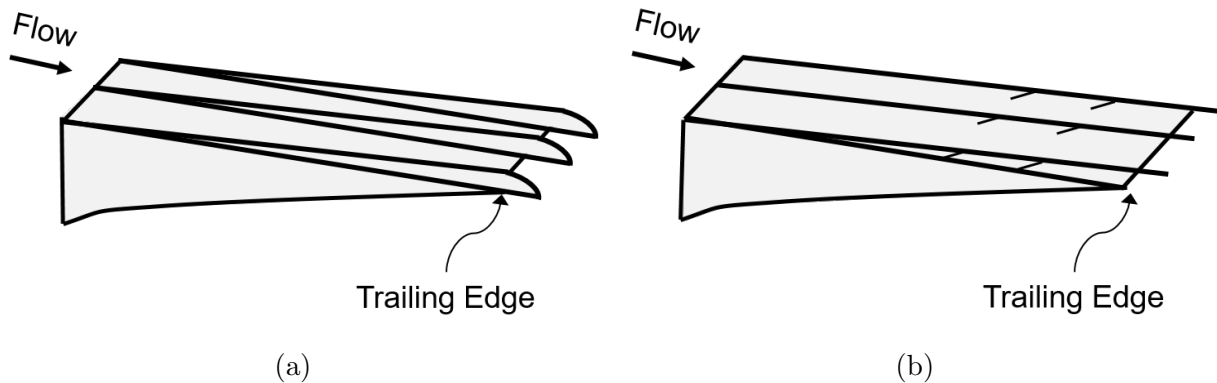


Figure 1.3: Schematic of treatments tested by [1] on the trailing edge of a DU96-W180 airfoil. **a)** Finlets, **b)** Rails.

somewhere between 1-4 mm, as the 1 mm spaced finlets led to a marked increase in low frequency noise, near 650 Hz.

- **Height.** The taller, 8 mm finlets ($\Lambda = 4.5^\circ$) led to greater noise reduction, attributed to the fact that they would cut further into the boundary layer leading to a stronger effect on the correlation lengthscale. They suggested that better attenuation at high angles of attack might be possible with taller finlets to account for the thicker boundary layer. Drag measurements were taken with 8 mm tall finlets, and the resulting increase in drag was found to be proportional to the increase in wetted area, conceivably a “best-case” scenario.
- **Thickness.** No clear pattern emerged for finlets with the same spacing and different thickness. This would indicate that the spacing is the more important parameter, and that there is some flexibility in selecting the thickness to make the treatments more robust.
- **Suction vs. Pressure Side.** The attenuation was highest when both sides of the airfoil were treated. It was hypothesized that the suction-side boundary layer was the dominant noise contributor for the cases tested.
- **Extensions.** Comparisons were made between finlets that ended at the trailing edge, and finlets with 10 mm extensions. Both were effective, but the finlets with *no* extensions actually performed better. This finding was important, as it confirms that the underlying mechanism isn’t necessarily modifying the edge scattering efficiency, like serrations, but a modification in the incoming boundary layer turbulence. This would also suggest that this boundary layer manipulation concept may be used in combination with existing trailing edge noise control technology like serrations.

The rail performance was quite similar to that of the finlets. The notable exceptions were that near stall, the rails significantly outperformed the finlets, and that 8 mm tall rails actually

performed worse than the 4 mm tall rails, possibly because of the larger gaps underneath the protrusions. Both of those designs successfully reduced the trailing edge noise between 2-4 kHz (the tall rails increased high-frequency noise at lower angles of attack). Overall, this experiment was very well-documented and successfully demonstrated the performance benefits and limitations of these bio-inspired treatments.

1.6.2 Experimental and Theoretical Analysis- Clark *et al.* [2]

The experiment just described had only far-field noise and mean surface pressure (lift) data. In a follow-up experiment, unsteady surface pressures were measured in the finlet channels in combination with mean surface pressures and far-field noise. The effects of chordwise finlet placement and skew angle were also examined, and a mathematical model based on vortex theory was also given to better understand finlet performance. As before, the experiment was performed on a DU96-W180 airfoil in the Virginia Tech Stability Wind Tunnel, with a trip strip placed on the 5 and 10% chord locations on the suction and pressure sides. Knowles microphones with a noise floor near 52 dB were used for the unsteady pressure measurements, so results were presented for a freestream of 50 m/s, or a chord Reynolds number of 2.5 million. Acoustic measurements were again made with a 117-channel microphone array.

In this experiment, only finlets similar to those in figure 1.3a were used. Spacing was kept constant at 4 mm, the thickness was generally 1 mm due to manufacturing constraints, and the height was generally 8 mm. In some cases, finlets with a height of 16 mm were used to investigate the suction-side performance at high angles of attack. The main differences in this experiment was that the airfoil trailing edge featured a 1.6 mm deep pocket at the trailing edge to house the finlet substrate, and the elimination of the finlet extensions. The substrate pocket was filled to ensure a smooth surface for the untreated trailing edge measurements.

Experimental Results

Beamform maps confirmed the acoustic findings in Clark *et al.* [1], and up to 12 dB attenuation was seen for the untripped case using the baseline finlets (8 mm height, 4 mm spacing, 1 mm thickness). This was the first time that finlets were shown to work on an untripped airfoil. The unsteady surface pressure spectra were very different for the pressure and suction sides. On the pressure side, the fluctuations were actually increased in the presence of the finlets. On the suction side, the finlets achieved up to 15 dB reductions above 2 kHz, where most of the far-field noise attenuation occurred. This surface pressure attenuation was similar to the performance of the unidirectional canopies over rough surfaces, the motivation for finlets [7]. The coherence results between adjacent pairs of Knowles microphones were mixed. Generally, the effect of the finlets was frequency dependent, meaning that below some frequency (dependent on angle of attack) the coherence was reduced, and above that frequency the coherence increased. However, the frequency at which the maximum coherence

occurred was usually smaller with finlets.

The drag findings were consistent with those seen previously [1], where the drag was found to be proportional to the wetted area. The 1 mm thick finlets, (twice that in the previous study) slightly decreased the lift over the range of attack angles tested.

Placing the finlets upstream of the edge (at 95 and 85% chord) produced a minimal change in far-field noise attenuation seen with finlets in the standard orientation, but the unsteady surface pressure attenuation was up to 20 dB, greater than that measured for finlets applied directly at the edge. The finlets were also placed in a “reversed” configuration, with the highest point facing upstream, and an increase in far-field noise was seen. This would suggest that the finlets are most effective at low leading edge angles, Λ . Using the taller, 16 mm finlets on the suction side was more effective at reducing noise at high angles of attack than the 8 mm finlets, confirming the idea that the finlets should be sized based on the local boundary layer thickness. However, there was a corresponding increase in drag. Interestingly, the lift penalty was similar for both 8 mm and 16 mm tall finlets. The finlets were shown to be robust to changes in flow direction, as there was significant noise attenuation present even for finlets skewed by 10 degrees relative to the flow direction. The best performance, however, was when the finlets were aligned with the flow (no skew).

The key experimental findings were as follows:

- **Acoustic Performance.** The results from Clark *et al.* (2017) [1] were confirmed, and the finlets proved effective on an untripped airfoil as well.
- **Unsteady Surface Pressures.** Attenuation with finlets was, to some degree, frequency independent. Reductions were seen at some frequencies, and actually increased in some low-frequency cases. Coherence results for adjacent microphones were similarly mixed.
- **Geometric Considerations.** The finlet profile should be designed to rise smoothly out of the airfoil surface e.g. low Λ . No detrimental effects were observed when placing the finlets upstream of the trailing edge. Combined with the observation that the tallest finlets proved effective at high angles of attack, this would suggest that the finlets can be sized based on the local boundary layer height. The finlets were also largely insensitive to skew angles, as they still achieved noise reductions. This may have practical benefits for field testing.

Mathematical Modeling

A mathematical model based on vortex sound theory was also given, to explain the performance that could be achieved by lifting the eddies away from the edge. They used a rigid plate with a porous cylinder at the trailing edge to represent the finlets, and investigated the noise produced as an undistorted line vortex passed over the edge. Results showed that

moving the vortices further away from the edge would result in noise reduction, consistent with Amiet's theory [17]. The model also showed that longer finlets (i.e. finlets with a lower sweep angle) would have better acoustic performance, consistent with the experimental findings from the reversed finlet case. It was noted that measurements of the upstream vorticity distribution would be helpful in developing a more robust model.

1.6.3 Related Experiments

Single hot-wire and surface pressure fluctuation measurements downstream of finlets on a flat plate were presented by Afshari *et al.* [24]. The key distinction between that study and the experiment described in this thesis is that their experiment was not conducted in an anechoic facility, meaning no direct far-field measurements could be made. Additionally, their finlet design was significantly different than those used by Clark *et al.* [1, 2], with leading edge angles of 28.3, 30.7, 35.3, meaning there could have been significant noise scattering off the finlet treatments. This was demonstrated in Clark *et al.* [1], where placing the finlets in a reversed orientation led to an increase in far-field noise. Lastly, the finlet trailing edges were placed upstream of the edge, at 86% chord, and the hot-wire measurements were made at 97.6% chord. However, their results serve to contextualize the discussion in chapter 3 of this thesis. They found that the finlets decreased the mean velocity in the boundary layer and tended to increase the turbulence intensity relative to the untreated trailing edge within the first 40% of the boundary layer thickness. The power spectral densities of the velocity fluctuations showed that the energy was reduced near the wall with either increasing finlet height or decreasing finlet spacing. Surface pressure fluctuation spectra measured about 67 mm downstream of the finlets were presented for frequencies between 200 and 4000 Hz, showing that the magnitude could be reduced by up to 8 dB near 4000 Hz. These results are consistent with the findings presented by Clark *et al.*, where placing the finlets upstream of the trailing edge led to significant reductions in the magnitude of the fluctuations. Afshari *et al.* [24] reported that the reduction in surface pressure increases with increasing finlet height and spacing. The spanwise lengthscales were reduced relative to the untreated flat plate between about 200-1800 Hz for finlets with 2 mm spacing. Generally, increasing the height and decreasing the spacing served to decrease the lengthscale. A decrease in spanwise lengthscale was also found in analysis by Clark [25]. Afshari *et al.* [24] also reported a decrease in convection velocity when the finlets were applied. Cross-correlations were presented for simultaneous surface pressure and hot-wire measurements made at 97.6% chord, but it is unclear how the presence of the hot-wire probe may have affected the surface pressure fluctuations. Afshari *et al.* [26] also reported unsteady surface pressure measurements for finlet designs conceptually similar to configurations F6^b and F7^c in Clark *et al.* [1], but with significantly steeper leading edge angles, which may lead to increased self-noise due to scattering off the finlets.

1.7 Technical Justification and Contributions of this Thesis

The preceding sections served to motivate the need for trailing edge noise control techniques, focusing on wind energy applications. Existing methods of noise control were introduced in section 1.5, where it was shown that they are aimed at modifying the physical geometry, or scattering efficiency, of the trailing edge. Although these approaches are effective, they can be difficult to retrofit to existing structures. Additionally, careful design is required to avoid adversely impacting the aerodynamic performance. For these reasons, researchers began to look for ways to manipulate the incoming boundary layer turbulence before it impacts the trailing edge. Inspiration was drawn from the silent flight of owls, which had been studied periodically for engineering applications until about the last decade, when researchers began to study owl-inspired solutions to noise control in depth. In particular, this thesis builds on the promising foundation laid by Clark *et al.* [7, 1, 2, 23], where the owl-inspired noise control devices termed “finlets,” and “rails,” were shown to consistently reduce trailing edge noise for variety of designs and test conditions. Because the experimental goals were to establish and document the acoustic performance, no flow measurements were taken. Afshari *et al.* [24] (reviewed in section 1.6.3) reported hot-wire measurements for finlets on a flat plate; however, for the reasons given in section 1.6.3, there remained a need for a thorough experiment to not only document the flow effects, but relate them to the physical processes which may be responsible for trailing edge noise reduction.

Thus, the primary objectives of this thesis are: to document the flow effects of the bio-inspired treatments, and to relate those flow changes to the reduction in far-field sound.

1.7.1 Achievements

Key contributions associated with this research:

- Measured the flow field immediately downstream of bio-inspired finlets and rails applied to a mock trailing edge.
- Identified the development of a mixing layer at the top of the bio-inspired treatments that may be causing a phenomenon known as shear sheltering.
- Demonstrated that the bio-inspired treatments significantly reduce far-field noise, and that the magnitude of the noise reduction appears to be correlated with the mixing layer characteristics.
- Validated design guidelines for bio-inspired treatments effective at reducing trailing edge noise.

- Developed the mock trailing edge used as a testbed for the bio-inspired treatments. Clearly characterized the acoustic and aerodynamics associated with the mock trailing edge for future research.
- Investigated the acoustic performance of the Anechoic Wall Jet facility, documenting the signal-to-noise ratio as a function of observer location for commonly used microphone arrays.
- Presented portions of this work at AIAA SciTech 2017.

The novel contributions of this thesis are the flow measurements downstream of the treatments and the analysis comparing the data to related literature and simulations([1, 26]). A hypothesis for the trailing edge noise attenuation based on the the concept of shear sheltering is proposed, as well as some design guidelines for these bio-inspired treatments. The application of these treatments to a sharp forward step is also discussed.

Chapter 2

Experimental Methods

2.1 Anechoic Wall Jet

This experiment was conducted in the Virginia Tech anechoic wall jet (shown in figures 2.1 - 2.2), a well-documented facility [6]. The variable-speed, 15 horsepower blower that powers the flow is housed in an anechoic enclosure, and connects to the settling chamber with a flexible hose. The chamber is also acoustically treated and contains baffles to prevent a direct acoustic path to the test section. Flow exits the 12.7 mm high, 1219 mm wide nozzle and enters the test chamber (flow shown as the blue line), growing into a fully-developed wall jet over the smooth wall on which the test articles are placed. The horizontal wall is 3058 mm long and 1600.2 mm wide, and its centerline is coincident with the center of the nozzle. The downstream edge of the plate has a circular 152.4 mm-diameter Plexiglass fairing attached to it to promote the Coanda effect and minimize any noise scattering.

The jet-exit speed can be varied from 20-60 m/s within ± 0.1 m/s, using the dynamic pressure based on the total pressure in the settling chamber and the static pressure at the nozzle. The uncertainty was computed by assuming a perfect gas and performing a “jitter” analysis, perturbing the inputs and recording the response. The dynamic pressure is measured with a ± 3.75 kPa-range Setra 239 pressure transducer. The flow temperature is measured with a thermocouple placed at the edge of the nozzle exit, connected to an Omega DP86T analog-output temperature display. Uncertainty in the thermocouple was estimated to be 0.1 degrees Celsius.

The origin of the Cartesian coordinate system, shown in figures 2.1 - 2.2, is placed at the spanwise center of the nozzle exit plane (on the wall), with the positive x -axis in the stream-wise direction, along the flow, and the positive y -axis as the wall upward normal. The positive z -axis, in the spanwise direction, completes the right-handed coordinate system.

The acoustic treatment in the test section consists of 89 mm egg crate acoustic foam on the

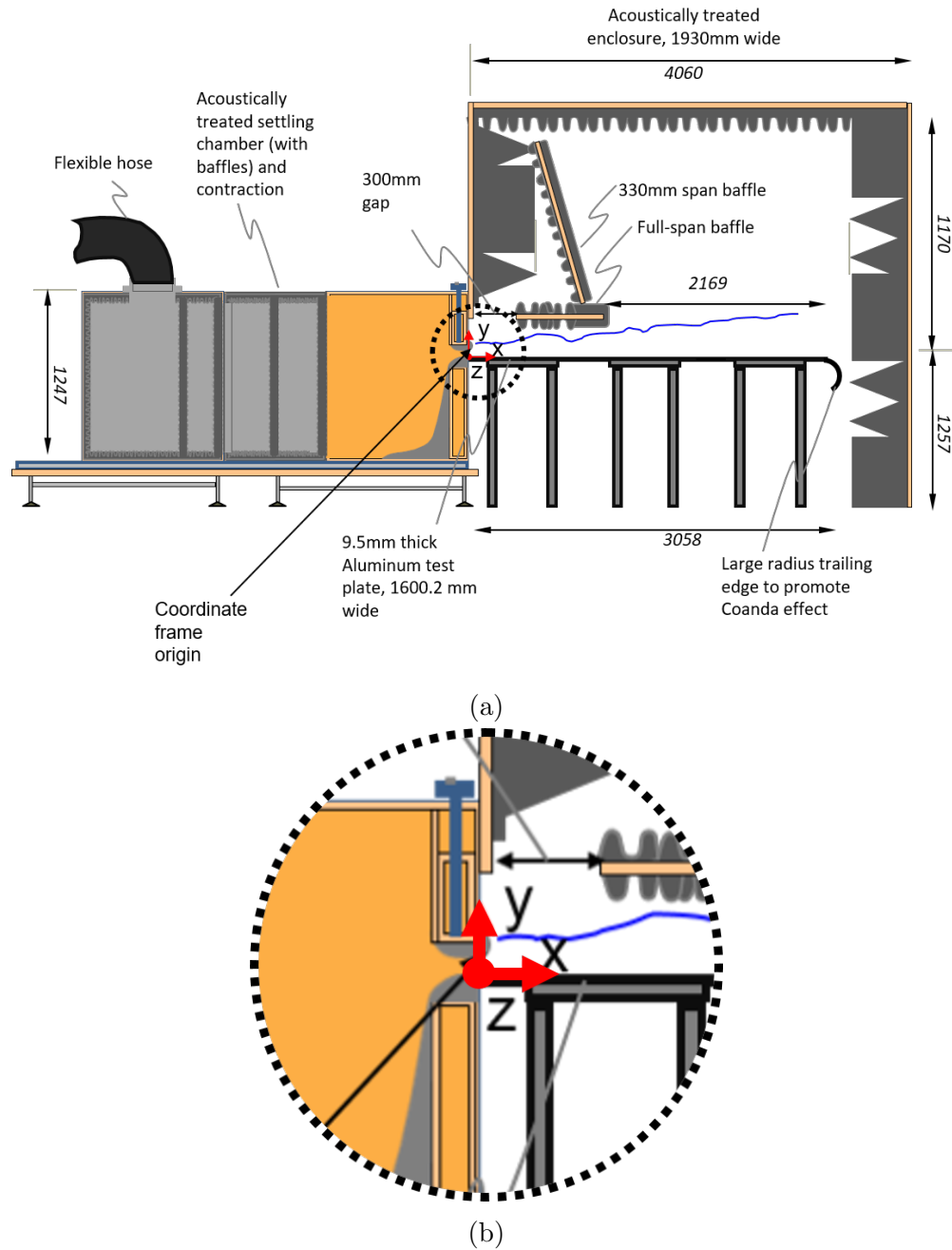


Figure 2.1: (a) Side-view schematic of the Virginia Tech Anechoic Wall Jet. Flow is from left to right. Dimensions are in millimeters. (b) Inset from figure 2.1a showing the coordinate system. The origin is on the smooth wall surface, on the spanwise center of the smooth wall. The x -direction is aligned with the flow, and the y -direction is the wall upward normal. The z -direction completes the right-handed coordinate system.

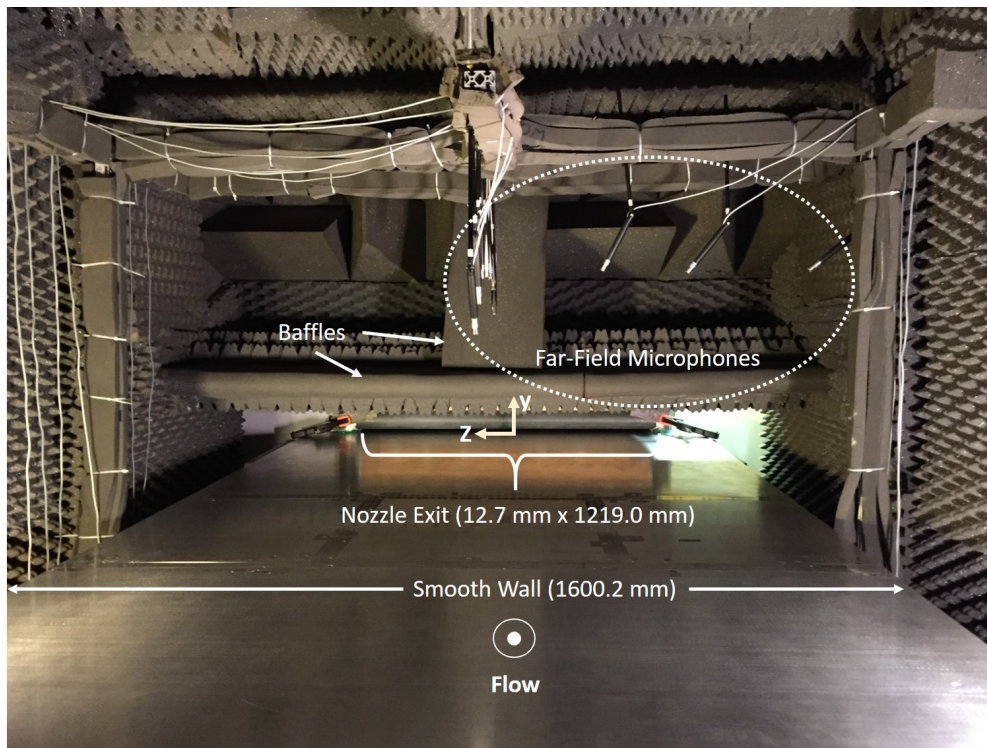


Figure 2.2: Wall jet interior, looking upstream. Coordinate system origin is on the smooth wall surface at the smooth wall centerline. The x -direction is aligned with the flow (out of the page). Far-field microphones shown in dashed circle.

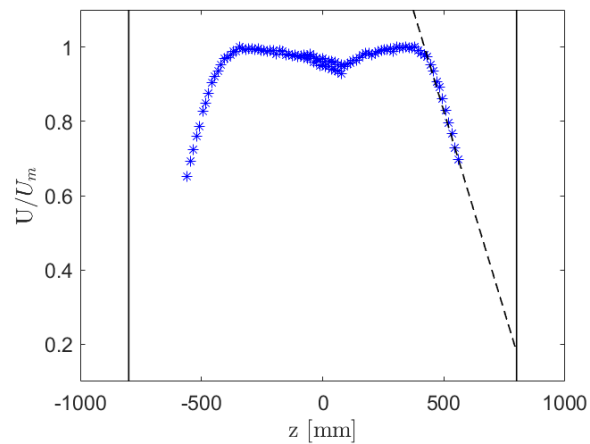


Figure 2.3: Spanwise velocity variation, normalized on the maximum velocity in the boundary layer, U_m . Data measured by Ian Clark, *, estimated decay, dashed line, wall edges, solid line. Probe was located at $x = 1257.3$ mm, $y = 6.35$ mm.

ceilings and side walls, and 457 mm wedges on the upstream and downstream walls. The egg crate foam is effective at damping noise above 1900 Hz, and the wedges damp noise above 188 Hz. The chamber has a 50mm gap around the bottom (not shown) through which the flow can exit the section to the lab atmosphere.

The two-dimensional region of the flow, where the speed is considered constant in the spanwise direction, is approximately 800 mm wide, symmetric about the x -axis. This was proven in 2007 [27], and validated in 2015 [5] by measuring the mean velocity profile along the span of the smooth wall, after the facility was slightly modified. Results from the 2015 measurement [5] are shown in figure 2.3. The measurement was taken at $x = 1257.3$ mm, $y = 6.35$ mm, and traversed along the spanwise (z) direction from about $z = -500$ mm to $z = 500$ mm, using the same coordinate system described above. The velocity deficit on the wall centerline was attributed to a surface imperfection in the wall, which has since been replaced. The flow exhibits symmetry across the jet centerline (coincident with the wall centerline e.g. symmetric about $z = 0$); this is expected to be the case with the current smooth wall configuration. The velocity is normalized on the maximum velocity in the boundary layer, U_m , defined further in the next section. The two-dimensional flow region, where the flow is relatively uniform ($U/U_m > 0.95$), is about 800 mm wide. Outside this region, the flow velocity appears to decay linearly. Using a first-order approximation for the decay, the velocity at side edges of the wall is about $18\%U_m$. Because of this, no aerodynamic or acoustic contamination is expected from the edges of the wall.

2.1.1 Flow Structure

Because this is a wall-jet facility, a brief discussion about wall jets in still air is warranted to clearly define the flow structure over a smooth wall. Launder *et al.* [3] wrote an extensive review on wall jet experiments, and the nomenclature used here is generally consistent with their own. A plane wall jet is shown in figure 2.4. The freestream velocity, U_∞ , is pictured here as nonzero to demonstrate the general concept; in the VT Anechoic Wall Jet, $U_\infty = 0$, since the fluid is exhausted into still air. The biggest difference between a wall jet and a typical boundary layer one might see on a flat plate in an open jet, for example, is the presence of the large shear layer. The wall jet has a clear velocity peak, U_m , and the distance from the wall to this point is considered the boundary layer thickness, δ . The half height, $y_{1/2}$, is the height at which the velocity has decayed to $U_m/2$. The jet velocity, U_j , is measured at the nozzle exit plane, which has a height b . Note that the x and y coordinates are consistent with the system shown in figures 2.1 - 2.2.

Wall jet parameters in the two-dimensional flow region for the smooth wall configuration can be estimated using the Wygnanski *et al.* [28] power law relations (shown in equations 2.1-2.5), with the coefficients for this facility derived in a previous measurement [5], included in table 2.1 for reference.

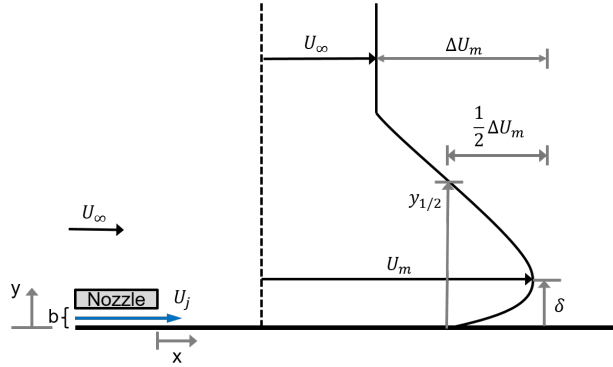


Figure 2.4: Wall jet nomenclature based on Launder *et al.* [3]. The velocity profile has a maximum U_m occurring at $y = \delta$, the boundary layer thickness. For the VT Anechoic Wall Jet, a jet of air at $U = U_j$ is exhausted from a nozzle of height b into still air, meaning $U_\infty = 0$. Flow is from left to right.

$$\frac{U_m}{U_j} = A_U Re_b^{n+1} Re_x^n \quad (2.1)$$

$$\frac{\delta^*}{b} = A_D Re_b^{p-2} Re_x^p \quad (2.2)$$

$$\frac{y_{1/2}}{b} = A_Y Re_b^{m-2} Re_x^m \quad (2.3)$$

$$\delta = A \delta^* \quad (2.4)$$

$$\theta = B \delta^* \quad (2.5)$$

Knowing the jet velocity commanded to the blower, U_j , the nozzle height, b , and the distance from the nozzle exit to the test article, x , one can compute the Reynolds numbers based on jet velocity and nozzle height (Re_b), or based on jet velocity and distance (Re_x). Knowing

Table 2.1: VT Anechoic Wall Jet Power Law Coefficients [5]

A_U	1.6814
A_D	0.0063
A_Y	0.015
A	18.2966
B	0.8357
n	-0.4702
p	0.9099
m	1.0651

these quantities, estimates of the wall jet parameters can be made with equations 2.1-2.5. Specifically, these Wygnanski relations yield estimates for the following: boundary layer thickness, δ , displacement thickness, δ^* , momentum thickness, θ , half-height, $y_{1/2}$, and the maximum velocity in the boundary layer, U_m . These estimates were helpful in sizing the bio-inspired treatments, interpreting acoustic data, and confirming flow measurements. Sample estimated wall jet parameters at the trailing edge location, $x = 1397$ mm, are included in table 2.2 (the trailing edge is described explicitly in the next subsection). The tabulated values were obtained by averaging the jet velocity, flow temperature, and pressure over 41 different measurements at each speed in order to characterize the test conditions. Each of these averaged quantities was used as an input to obtain the estimated parameters. The nominal jet velocity, U_{ref} , is the velocity commanded to the blower, while the measured jet velocity, U_j , measured flow temperature, T_f , are used to compute the appropriate jet Mach number, M (assuming perfect air). The remaining tabulated values are computed with the power law relations.

2.2 Mock Trailing Edge

A “mock” trailing edge was developed to produce trailing edge noise and act as a testbed for the bio-inspired noise treatments. The term “mock” is used here to emphasize the fact that the flow only passes over one side of the trailing edge, and the edge was close to a wall. A schematic of the mock trailing edge, including the dimensions, is shown in figure 2.5, and a side view of the fabricated piece is shown in figure 2.6. The mock trailing edge was made from two 12.7 mm thick pieces of aluminum each with a length of 114.3 mm, span of 485.78 mm and a $t_{TE} = 0.76$ mm thick trailing edge, limited only by manufacturing concerns. The length was chosen to accommodate the length of owl-inspired noise treatments tested in the past [1, 2]. The trailing edge was placed at $x = 1397$ mm. The only design constraint on the total span of the mock trailing edge was that the tips needed to be sufficiently far outside the high-velocity 2-D flow. The full span of the mock trailing edge, then, was 971.55 mm, ensuring the ends were outside the 2-D region (as discussed previously) and immersed in a

Table 2.2: Smooth wall boundary layer parameters, $x = 1397$ mm. Measured values, to the left of the break, were averaged over 41 experimental runs at each speed. Estimated values, using Re_x Wygnanski’s relations (equations 2.1-2.5, table 2.1) are right of the break.

U_{ref} [m/s]	U_j [m/s]	T_f [K]	M	$Re_x * 10^6$	U_m [m/s]	δ [mm]	δ^* [mm]	θ [mm]	$y_{1/2}$ [mm]
20	20.01	296.66	0.06	1.70	6.56	18.54	1.01	0.85	99.92
30	30.00	296.70	0.09	2.55	10.07	17.23	0.94	0.79	105.33
40	39.98	296.98	0.12	3.40	13.65	16.37	0.89	0.75	109.32
50	50.01	297.56	0.14	4.23	17.30	15.73	0.86	0.72	112.50
60	60.00	298.17	0.17	5.06	20.98	15.23	0.83	0.70	115.15

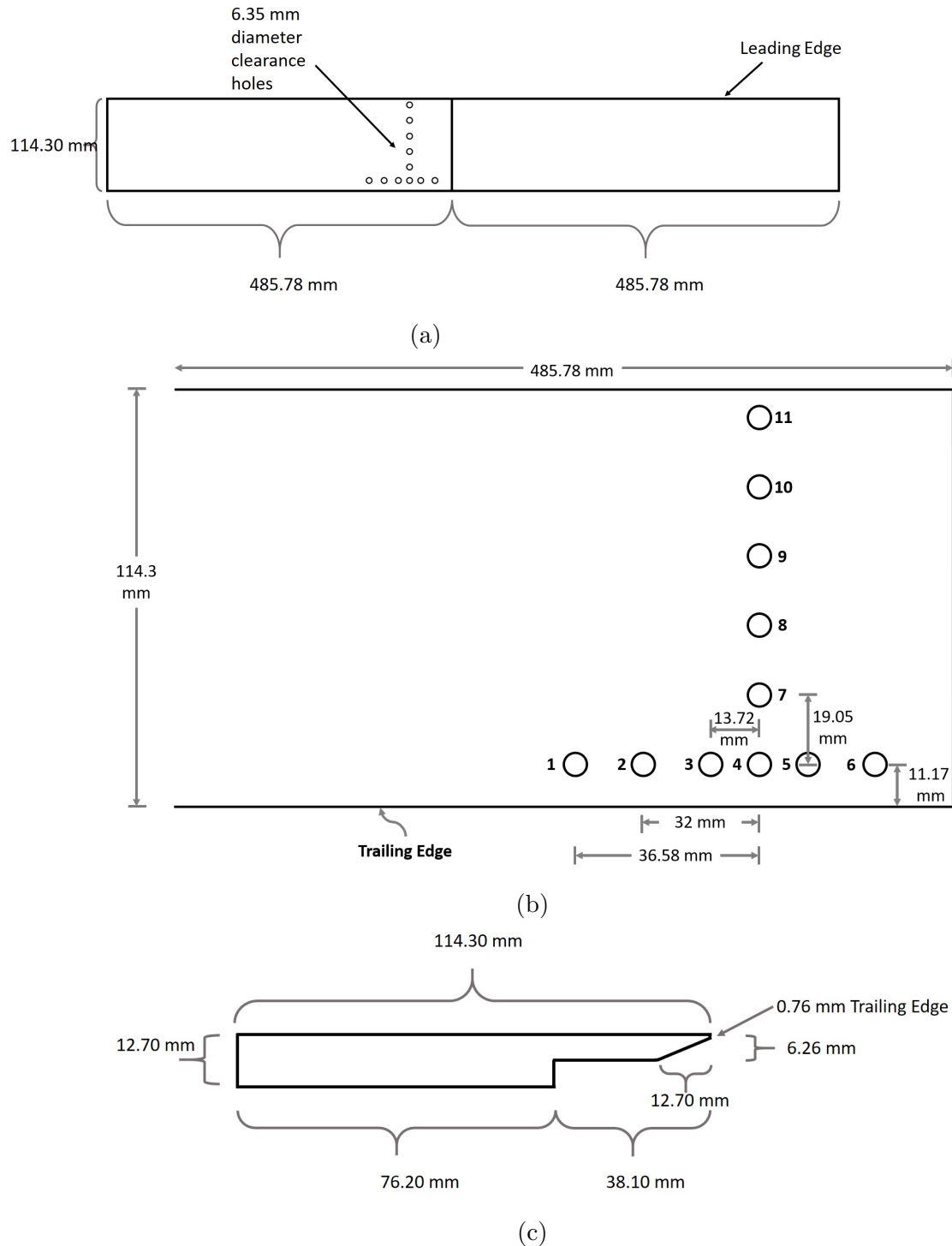


Figure 2.5: Schematic of the mock trailing edge piece, including dimensions. (a) Top view. Clearance holes are for mounting surface pressure fluctuation microphones flush with the trailing edge surface. (b) Dimensions and numbering scheme for the surface pressure fluctuation microphone positions. See figure 2.5a for locations relative to entire trailing edge piece. (c) Side view, showing the 0.76 mm trailing edge.

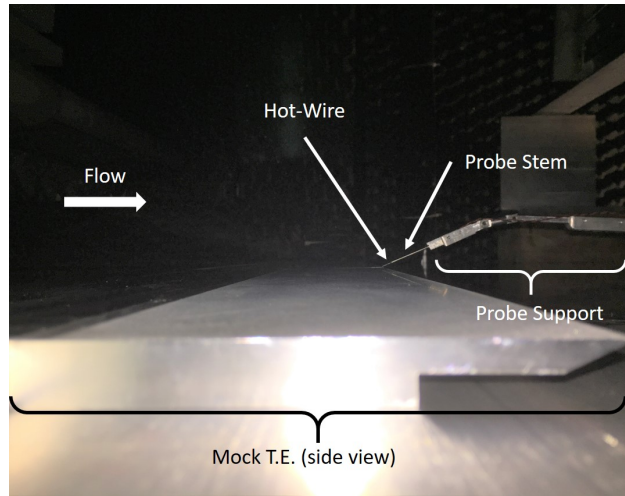
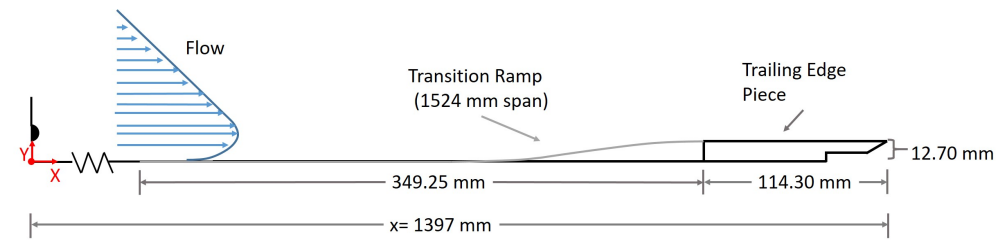


Figure 2.6: CTA probe relative to the mock trailing edge. The figure can be thought of as being in the $x - y$ plane, where x is along the flow and y is the wall upward normal.

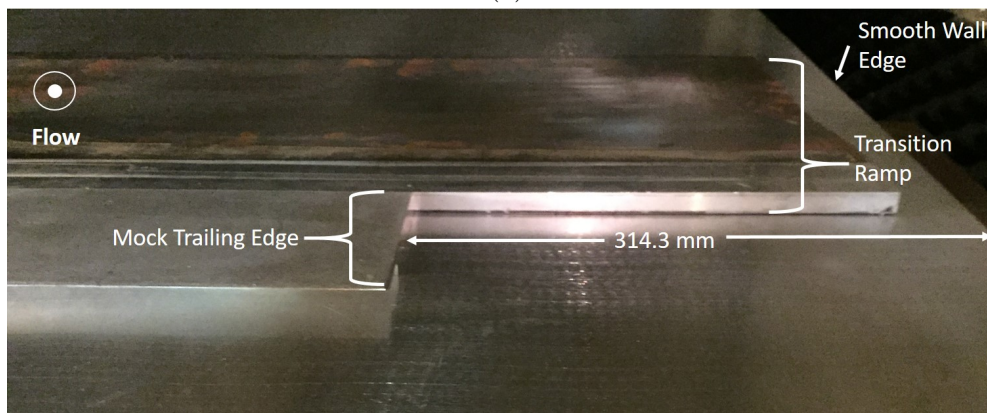
flow on the order of $U/U_m=0.8$. Additionally, since the flow measurements were taken within 10 mm of the mock trailing edge centerline (collinear with smooth wall centerline), aerodynamic contamination due to the spanwise tips of the trailing edge was not a concern. The acoustic effect of the tips will be discussed presently.

The 6.35 mm diameter clearance holes, which extend through the entire trailing edge piece and were aligned with equal-sized holes in the wall, were used for mounting surface pressure fluctuation microphones. The hole pattern was chosen to give flexibility in choosing the relative distances between sensors, which was important in maximizing the data available for computing the stream- and spanwise length scales of the turbulent pressure fluctuations. With the modular design, the holes can be placed near the center of the test section or near the outer edge, based on whether or not surface pressure measurements are being performed. The hole placement relative to the trailing edge is shown in figure 2.5b. The joint between the two trailing edge pieces, as well as any unused holes, were taped over with 0.08 mm thick (3.1 mil) packaging tape.

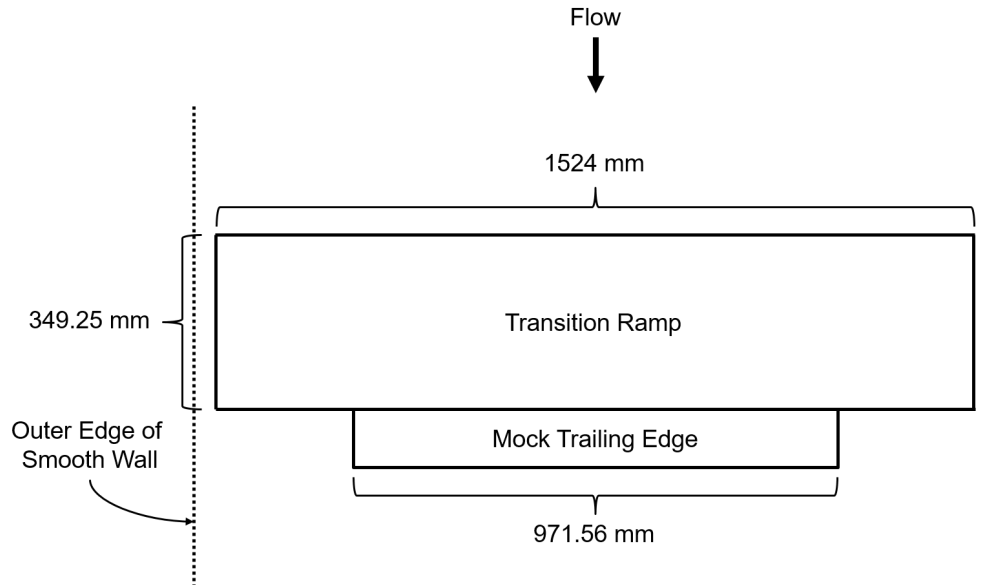
A 349.25 mm long, 12.7 mm high metal transition ramp (1524 mm span), with the shape of a shallow inflection, was attached upstream of the leading edge of the test piece to allow the boundary layer to grow smoothly toward the trailing edge and prevent separation associated with a forward step. A schematic of this is shown in figure 2.7a. A scaled-down, 3.2 mm-high ramp with a similar profile was used by Devenport *et al.* [29]. In that experiment, hot-wire measurements showed that the aerodynamic effect of the ramp was minimal, slightly increasing the maximum speed U_m by up to 1% of U_j . The aerodynamic effect of the 12.7 mm ramp is shown to be on the same order of magnitude in section 3.2, within the experimental uncertainty. Additionally, any flow variation due to the transition ramp will be accounted for in the analysis, as the treated trailing edge profiles will be compared to profiles measured



(a)



(b)



(c)

Figure 2.7: (a) Schematic of the 349.25 mm long transition ramp attached to the leading edge of the test article (side view). (b) Top view schematic of the transition ramp-trailing edge assembly. (c) Transition ramp attached upstream of the mock trailing edge, to ensure smooth boundary layer growth. The gap between the end of the mock trailing edge and the ramp edge did not need to be treated, as this is well outside the 2-D jet region.

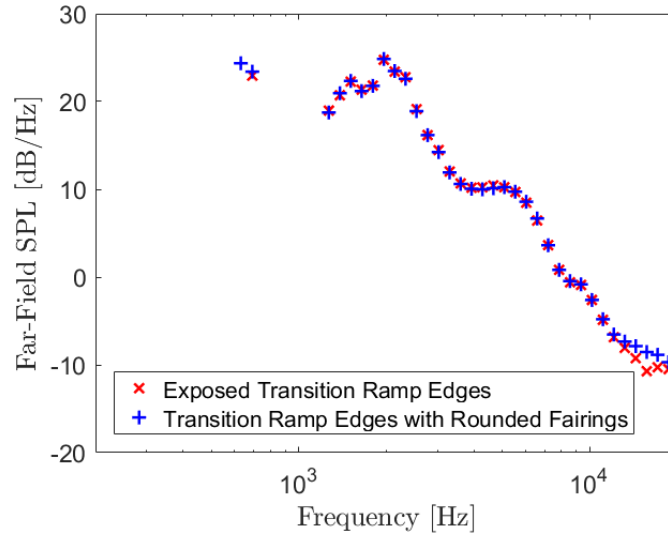


Figure 2.8: Far-field spectra for $U_j=60$ m/s (measured at $\theta=123.5^\circ$, see following section for microphone setup details) showing the acoustic impact of the exposed outer edges of the transition ramp. Comparisons were made using rounded endpieces and a full-span trailing edge piece. Spectra are shown using different symbols for clarity.

from the surface of the untreated trailing edge.

Specifically, the leading edge of the ramp was attached to the wall with 0.1 mm thick (4.6 mil) aluminum foil tape, such that the ramp centerline was collinear with the x -axis. Note that the ramp had a span of 1524 mm, 552.44 mm longer than the assembled trailing edge piece. This is shown with the top view schematic in figure 2.7c. As a result of the difference in span between the trailing edge and the transition ramp, a 276.22 mm-wide portion of the ramp trailing edge was left exposed on either side. This exposed portion was outside the high-speed, two-dimensional portion of the wall jet described previously. Hence, the aerodynamic impact of these exposed portions on the mock trailing edge is negligible.

Care was taken to ensure that the sharp backstep created by the exposed portions of the transition ramp (see figure 2.7b) did not contaminate the acoustic measurements. The far-field Sound Pressure Level (SPL) spectra for the mock trailing edge-transition ramp combination are shown in figure 2.8. Data are shown for $U_{ref} = 60$ m/s, measured by a microphone at $\theta = 123.5^\circ$, above the wall jet centerline. A detailed explanation of the microphone array is given in the following section, as are the details of the SPL calculations. Examining figure 2.8, it is clear that adding rounded fairings to the exposed ramp to smooth the sharp backstep made no difference to the noise throughout almost the entire frequency range. In fact, they actually slightly increased the noise at high frequencies, by a maximum of 2 dB at about 15 kHz. Figure 2.8 is included here to show that the the acoustic effects of the exposed portions of the transition ramp are negligible. This minimal acoustic impact is

consistent with the initial expectation that the exposed parts of the transition ramp would not contaminate any far-field measurements. For trailing edge noise scaling on U^6 , the reduced speed at the edges of the plate means that the radiated sound would be about 6 dB lower than the trailing edge noise emitted in the 2-D region.

2.3 Far-Field Sound Measurements

The far-field sound was measured using 1/2-inch Bruel and Kjaer (B&K) 4190 microphones connected to B&K 2669L preamplifiers, pictured in figure 2.2. The 4190 microphones have a flat frequency response for a 0° incidence angle. A flat frequency response is desirable because it means the microphone is not distorting the measurement outside of a specified frequency and amplitude tolerance. For example, at higher frequencies, reflections and diffractions can cause a pressure increase in front of the microphone diaphragm resulting in a (misleading) increased output voltage if not accounted for. The diaphragm inertia could also reduce the output voltage in a potentially misleading way. Having a flat frequency response implies that the microphone has been designed to minimize these sources of interference. This microphone unit (comprised of the 4190 microphone and 2669L preamplifier) has a ± 2 decibel (dB) variation in sensitivity over the frequency range of 3.15-20,000 Hz.

The dynamic range is 21.4-162 dB, which can be thought of as the difference between the noise floor and the highest Sound Pressure Level (SPL) the microphone can handle. Typically, the noise floor is expressed as the equivalent sound pressure level due to inherent noise, which can be thought of as the acoustic sound that would produce the same microphone output as the microphone self-noise. For the B&K unit, the noise floor is A-weighted. The upper limit on the dynamic range is generally determined by the level where a given amount of total harmonic distortion appears. The B&K unit upper limit is given by a 3% distortion in SPL rounded to the nearest integer (the undistorted peak level will normally be 3 dB higher).

The combined sensitivity of the unit is -25.9 ± 0.2 dBV (with a 95% confidence level), where dBV is a decibel with respect to 1V/Pa. In terms of millivolts per Pascal, the sensitivity is 50.7 mV/Pa. The two are related as follows:

$$(Sensitivity)_{dBV} = 20 \log_{10} \frac{(Sensitivity)_{mV/Pa}}{1000 mV/Pa} \quad (2.6)$$

where 1000 mV/Pa is the standard reference output ratio.

The microphone units were connected to a six-channel B&K LAN XI 3050-A-60 module with a UA-2101-060 front panel. The 24-bit LAN XI module is used for microphone power, signal conditioning, and data acquisition. Input channels range from DC to 131 kHz. The front panel was necessary to convert the standard BNC connectors to seven-pin LEMO microphone connectors, designed to be used in conjunction with microphones that require an external 200 V polarization voltage.

The microphone units were placed into B&K UA-1317 microphone holders attached to an aluminum gantry wrapped in acoustic foam, pictured in figure 2.2. The gantry was clamped to a support structure underneath the wall, away from the edges of the plate. The microphones themselves were no closer than $y = 440$ mm from the wall surface, well outside the flow. The microphones were shielded from noise radiated at the nozzle exit by two baffles (horizontal and vertical) wrapped with acoustic foam. Recent work in this facility [5] has shown that the baffles do not adversely impact the flow.

In total, eight microphones were used to form a streamwise array, and four were used in the spanwise array, with one microphone at 90 degrees shared between both arrays as shown in figures 2.2 and 2.9. Because of the documented flow symmetry in this facility (described in the previous section), the spanwise array only covered half the span.

The streamwise microphone array consists of eight co-planar microphones along an arc with a constant, $R = 578$ mm radius, centered at the trailing edge location ($x = 1397$ mm) and contained in the $z = 0$ plane. The array is shown in figure 2.9a, where $\theta = 123.5^\circ$ corresponds to the upstream microphone, and $\theta = 51.5^\circ$ corresponds to the downstream microphone. Uncertainty in the radial distances was 3 mm. Note that θ is measured from the downstream direction, with $\theta = 0^\circ$ corresponding to the flow direction. The microphone at $\theta = 90^\circ$ is directly above the trailing edge, and is also part of the spanwise array. The spanwise array (figure 2.9b, where flow is directed out of the page) uses four co-planar microphones in the $x = 1397$ mm plane. All are pointed to the center of the streamwise array. The spanwise array observer angles (ϕ) are measured such that $\phi = 0^\circ$ points in the negative z-direction. Angular uncertainties were $\delta_\theta = 0.5^\circ$ and $\delta_\phi = 1^\circ$, and the uncertainty in the radial location was $\delta_R = 1.6$ mm

The experimental acoustic data will be presented as Sound Pressure Level (SPL) in units of dB/Hz. SPL is defined here as

$$SPL = 10 \log_{10} \left(\frac{G_{pp}}{p_{ref}^2} \right) \quad (2.7)$$

$$G_{pp} = \frac{2}{n_d f_s N_{rec}} \sum_{i=1}^{n_d} |X_i(f)|^2 \quad (2.8)$$

where G_{pp} is the one-sided power spectral density (units of Pa^2/Hz), normalized to 1 Hz bandwidth levels, and the reference pressure, p_{ref} , is $20 \mu\text{Pa}$. The spectra are calculated using the procedure given by Bendat & Piersol [30], shown in equation 2.8. Here, n_d is the number of records, f_s is the sampling frequency, N_{rec} is the number of samples per record, and $X_i(f)$ is the finite Fourier transform of each record. Essentially, to go from a time history of the signal (from a microphone, in this case) to the power spectral density, the time history was divided into n_d records of length N_{rec} . Then, each record was multiplied by a Hanning window with 50% overlap and the appropriate loss factor to prevent side-

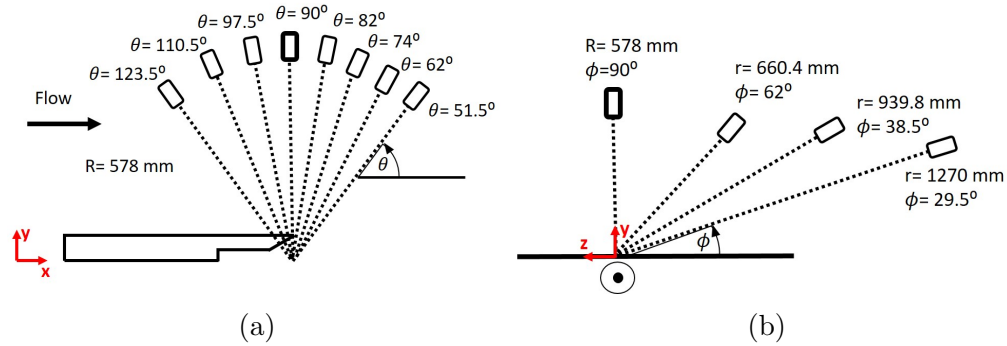


Figure 2.9: Far-field microphone observer angles relative to trailing edge (a) Streamwise far-field array observer angles, measured relative to the upstream horizontal. Bolded microphone is at $\theta = 90^\circ$, and is also part of the spanwise array. (b) Spanwise far-field array observer angles, measured relative to the vertical. Bolded microphone at $\phi = 90^\circ$ is also part of the streamwise array.

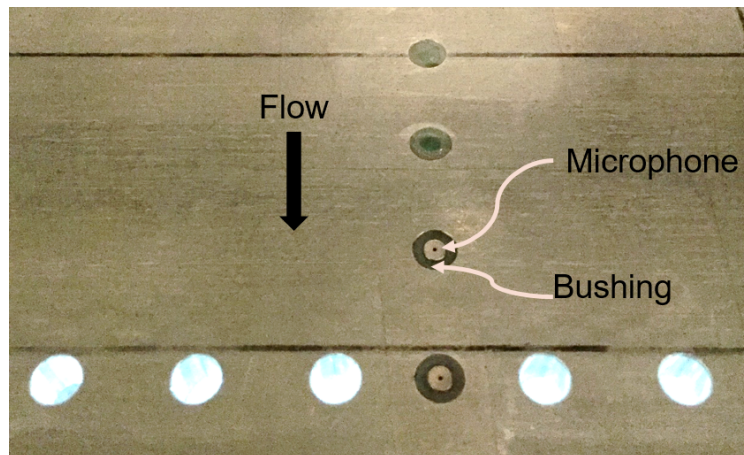


Figure 2.10: Top view of two B&K 4138 microphones mounted flush with the smooth wall surface to measure unsteady surface pressure fluctuations.

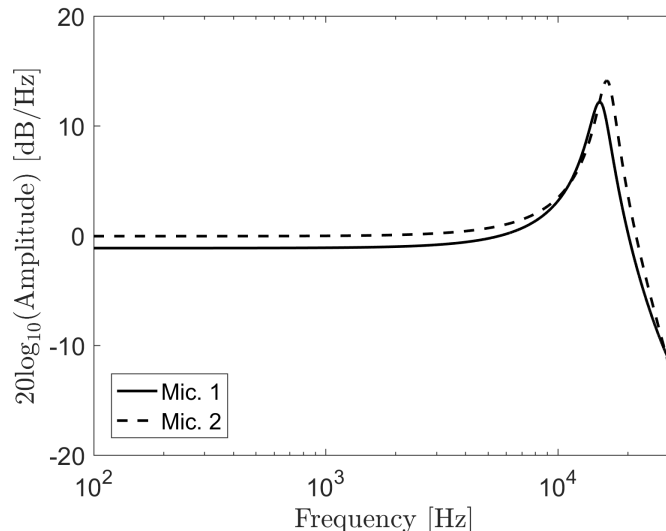


Figure 2.11: Amplitude response of the B&K 4138 microphones with pinhole caps used to measure unsteady surface pressure fluctuations.

lobe leakage and preserve the frequency resolution, and transformed with a Fast Fourier Transform (FFT). Finally, the sum of the square of the FFT magnitude for each record is computed ($\sum_{i=1}^{n_d} |X_i(f)|^2$) and scaled as in equation 2.8. The spectra were calculated using $n_d = 512$ and $N_{rec} = 8192$ samples per record.

2.4 Surface Pressure Fluctuation Measurements

Surface pressure fluctuations were measured with B&K 4138-A-015 (1/8-inch) microphones connected to type 2670 preamplifiers. The combined microphone-preamplifier unit is commercially available, assembled in a clean room. Per the manufacturer, the unit has a flat frequency response (± 2 dB) from 6.5 to 140 kHz. The dynamic range is 52.2 to 168 dB. The 95% confidence level sensitivity is -65 dBV, or 0.56 mV/Pa, as defined in equation 2.6. In these experiments, the microphones were housed in additively manufactured 6.35 mm diameter bushings and carefully mounted to be flush with the surface of the test article, as in figure 2.10. In spite of this, the uncertainty in the microphone y -positions was ± 0.5 mm. Each microphone was modified with a 0.5 mm pinhole cap to reduce the sensing area, and, consequently, the spatial averaging. A 0.5 mm diameter has been demonstrated to be small enough to resolve fluctuations up to 20 kHz [6]. The signals were recorded with the same LAN XI module and sampling characteristics as the far-field microphones. Note that the unsteady surface pressure data will be presented as SPL (units of dB/Hz) in the same manner as the far-field noise data, described in the previous section.

Because of the modified pinhole cap, these microphones had to be calibrated to identify their frequency response. The calibrations were performed by Liselle Joseph (described most recently in [31]), and are included in this thesis for completeness. The microphones were calibrated in an anechoic chamber using an Agilent E1432 digitizer and a University Sound ID60C8 speaker to emit white noise. A B&K 4138 1/8th-inch microphone with a standard salt-and-pepper cap, like the ones used in the far-field noise measurements, was used as a reference microphone to calibrate the speaker output. The amplitude response of the calibrated microphones used in the experiments described in this thesis are shown in figure 2.11. Two B&K 4138 microphones were used to measure the unsteady surface pressure fluctuations. Referring to figure 2.5b, the microphones were placed in various locations (positions 1 through 9) to give multiple relative distances for a correlation analysis. The different combinations are given in table 2.4.

2.5 Constant-Temperature Anemometry

2.5.1 Calibration

Flow measurements were made using a Constant Temperature Anemometry (CTA) technique with a single wire. As air flows over the wire, changing its thermal resistance, the anemometer must change the voltage supplied to the wire in order to maintain a constant temperature. Those voltage fluctuations can be monitored and converted to corresponding velocity fluctuations. The single wire allows for measurement of the mean velocity and turbulence quantities in the direction normal to the wire. It is important to perform velocity calibrations with the probe prior to any measurements, to ensure that the voltage fluctuations are interpreted correctly.

The calibration setup was external to the wall jet, and is shown in figure 2.12. The single-wire probe, an Auspex Corporation model AHWU-100, was connected to a Dantec StreamLine Constant Temperature Anemometer (CTA) analog system with a 90N10 frame. The wire itself is 5-micron-diameter Tungsten, with a resistance of approximately 825 Ohms per foot. The probe itself was placed in the exit plane of the calibration jet, powered by a 5 horsepower Baldor M3613T motor connected to a high-pressure blower (Cincinnati Fan HP-4C17). Air leaves the blower and passes through a flexible hose before reaching a 228.6 mm-long, 165.1 mm-diameter Plexiglass settling chamber, and exits through a 44.45 mm-long conical nozzle (24.5 mm-diameter flow passage). The flow temperature and dynamic pressure were measured with the same equipment described in section 2.1. The reference temperature probe for the CTA system was attached to the probe mount.

The hot-wire signal was recored with a National Instruments 9215 DAQ, sampled at 51.2 kHz for 16 seconds, until 100 records (with 8192 samples per record) were acquired. The calibration jet velocity was varied from 10.5-30.5 m/s, to encompass the expected velocity at the

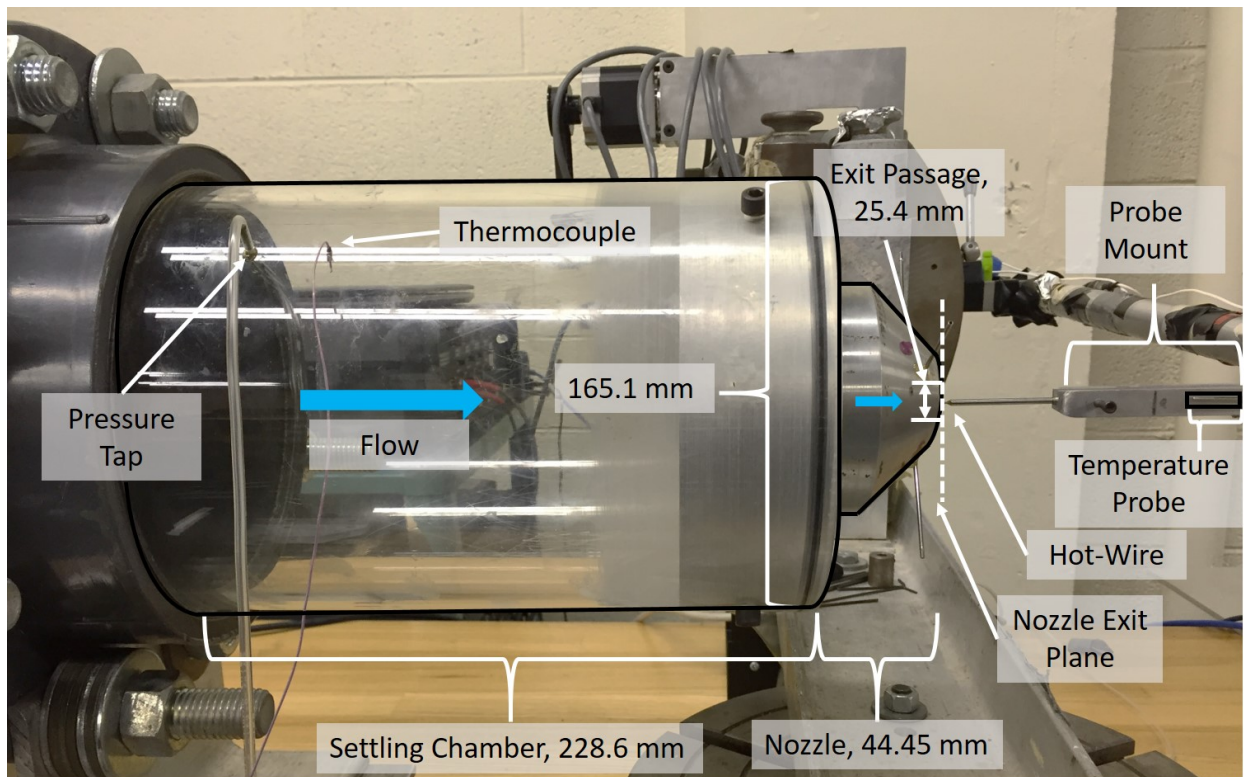


Figure 2.12: Close-up of the setup used to calibrate the jet. Flow travels from left to right, as indicated with thick arrows, through the Plexiglass settling chamber and the conical nozzle (both are outlined in black). The dashed line indicates the nozzle exit plane.

measurement location (see table 2.2).

$$E^2 = A + BU_j^n \quad (2.9)$$

The standard formulation of King’s law, given in equation 2.9, was used to convert the voltages to velocities. Here, E is the voltage, A and B are the calibration constants, $n=0.45$, and U is the measured flow velocity. The calibration constants can be found with a least-squares fit to U^n versus E^2 . Using the calibration constants, King’s law can be applied to approximate velocity in the unknown flow at the hot-wire. The calibrations used in this thesis are shown in figure 2.13a, where different symbols are used to denote the different calibration runs. The “inverse” calibration curves are shown in figure 2.13b, which were used to estimate the system sensitivity $\partial U/\partial E$ for the uncertainty analysis. Temperature variation was less than 1 degree Celsius, maintained by heating the inflow to the calibration jet at low speeds and reducing or removing the heater as the motor naturally heated up at higher speeds. This variation is shown in figure 2.13c. Temperature variation in the wall jet was on the order of 2 degrees Celsius. Corrections for this variation were done with the method described by Bearman [32].

2.5.2 Measurement

Once calibrated, the probe was placed in the wall jet system, shown in figure 2.14. The two-axis traverse system consists of an aluminum frame and two Compumotor 557-83-MO stepper motors with threaded rods for motion along the y - and z - axes. Each motor was controlled by a Parker PDX13 motion controller. The aluminum traverse frame was clamped firmly to the wall to minimize vibration. The probe support, shown in figures 2.6 and 2.15a, was approximately 240 mm long, in order to minimize the upstream interference of the traverse system, without extending far enough that probe vibration would be a serious factor. Visual inspection while the tunnel was operating at its maximum speed confirmed that vibration was not a problem. The reference temperature probe was fixed to the side of the probe mount. The entire structure could be manually picked up and moved to different streamwise locations; for this experiment, it was fixed to the smooth wall such that the the probe could be placed near the trailing edge location, $x = 1397$ mm. Unless otherwise noted, the hot-wire probe was located 3 ± 1 mm downstream of the trailing edge, at $x = 1400$ mm. The relative probe location and traverse profile are shown in figure 2.15. The vertical grid had measurements every 0.25 mm for $0 \leq \tilde{y} \leq h + 2$ mm, followed by 6.35 mm increments above that, until a maximum of $\tilde{y} = 120.4$ mm.

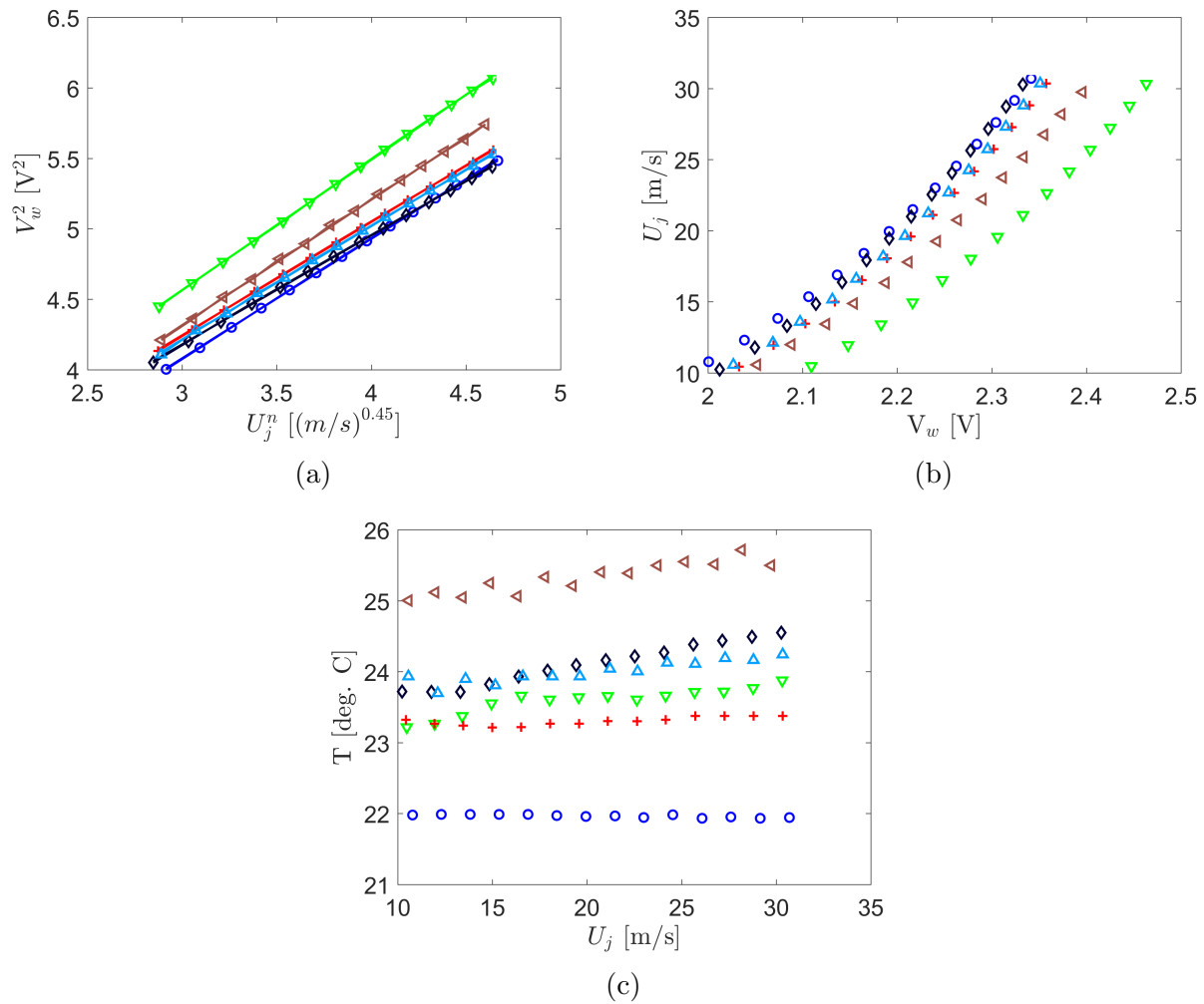


Figure 2.13: Calibration results for the CTA hot-wire system. Different markers-color combinations indicate data for each unique calibration used in acquiring the result presented in chapter 3. **(a)** King's Law fit (solid line) to the measured data, used to identify the A and B constants. **(b)** Inverse calibration curve, used to estimate the sensitivity $\partial U/\partial E$ for uncertainty analysis. **(c)** Variation in calibration flow temperature.

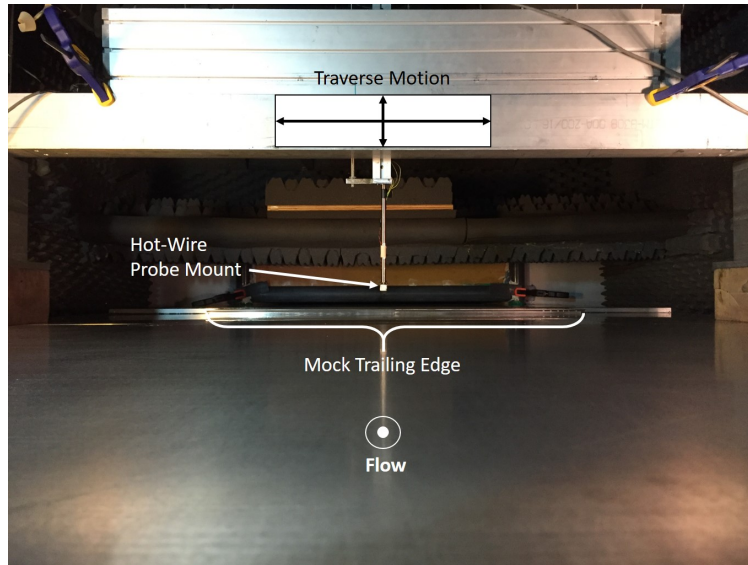
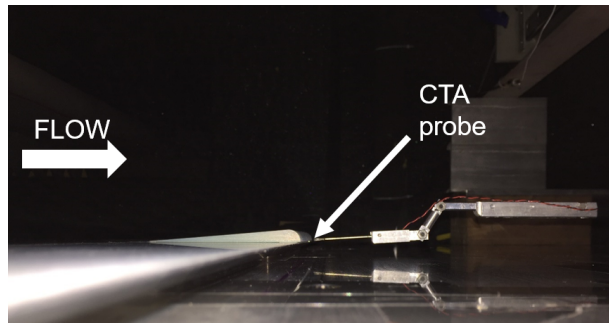


Figure 2.14: CTA set-up in the wall jet. Stepper motors and threaded rod for z -axis motion are not pictured. Figure is in the $y - z$ plane.

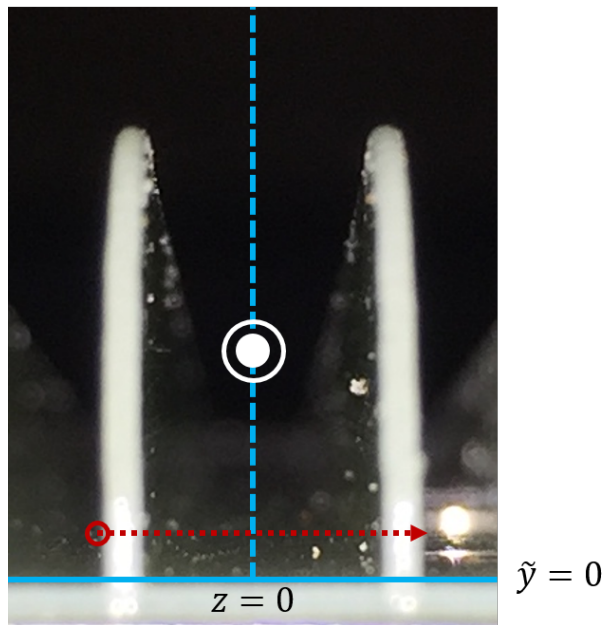
High-Frequency Contamination

A large, high-frequency spike was present in the hot-wire signals throughout all measurement runs, leading to artificially high turbulence intensities. This spike was present regardless of the specific probe-wire combination in use. The narrowband power spectral densities of the velocity fluctuations, $G_{uu}(f)$ are shown up to the Nyquist frequency in figure 2.16 for three different probe locations. The spectra were computed using by breaking the time series into 100 discrete records, windowing each record with a Hanning window, and averaging the Fast Fourier Transform of each record with 50% overlap, as shown in equation 2.8. Due to experimental time constraints, auxiliary measurements to correct for the high-frequency contamination could not be made. Thus, turbulence intensities were computed as shown in equation 2.10, by integrating the power spectral density up to 7000 Hz, before the high-frequency spike. Note that integrating the power spectral density gives the variance, or mean-square, of the quantity. Since turbulence intensity involves the root-mean-square, the square root of the integral is required. For reference, a vertical black line has been added to figure 2.16 at the cutoff frequency of 7000 Hz, not to be confused with the power spectral density.

$$\text{T.I.} = u'/U_m = \left[\int_{6.25}^{7000} G_{uu}(f) df \right]^{1/2} / U_m \quad (2.10)$$



(a)



(b)

Figure 2.15: **(a)** Hot-wire probe location relative to the finlets **(b)** Schematic of the probe traverse profile. Vertical measurements are made along the channel centerline (vertical dashed line), and spanwise measurements are made from the outside of the left finlet to the outside of the adjacent one (horizontal arrow).

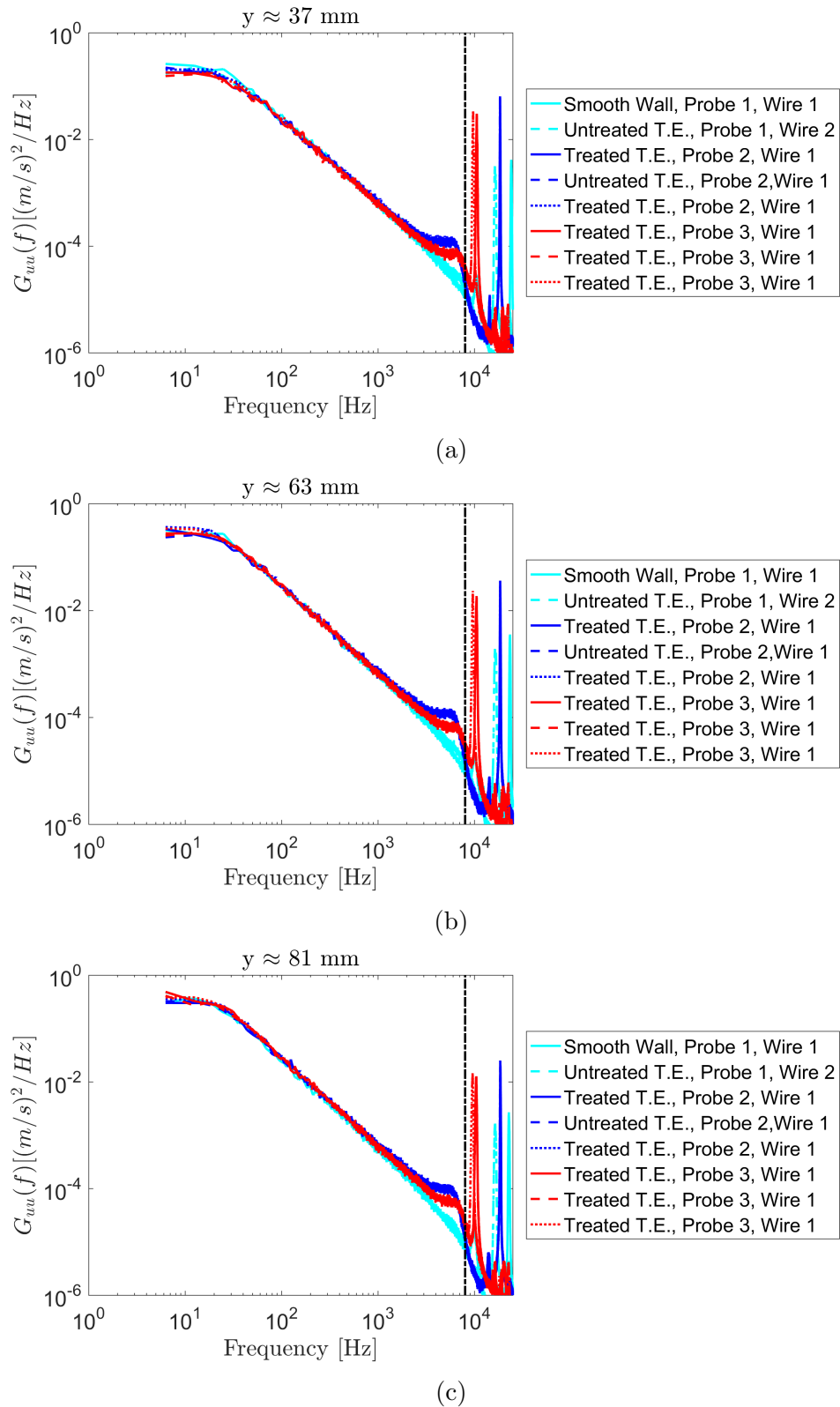


Figure 2.16: Turbulence spectra for each measurement run, with the probe located at (a) $y \approx 37$ mm, (b) $y \approx 63$ mm, and (c) $y \approx 81$ mm. The vertical black line (dash-dot) has been included to show the cutoff integration frequency (7000 Hz), and does not represent data.

2.6 Trailing Edge Treatments

In this study, the focus is on owl-inspired trailing edge treatments for passive noise control, such as those first described in Clark *et al.* [23], termed “rails” and “finlets.” All but one treatment examined here are of the finlet variety, and a finlet schematic is shown in figure 2.18a. Each finlet treatment was additively manufactured (3D-printed) on a 0.5 mm-thick, 114.3 mm-long, 228.6 mm-span substrate layer made of an ABS (Acrylonitrile-Butadiene Styrene) polymer, using a Connex3 polyjet printer. For hot-wire measurements, only one 228.6 mm span treatment was applied to the center of the mock trailing edge. Multiple pieces were used to treat the full trailing edge span for far-field and surface pressure measurements. The fins themselves are $L = 101.6$ mm long, with a perimeter consisting of a straight line that runs from the leading edge to a quarter circle of radius h tangent to the trailing edge. This radius will be referred to throughout the paper as the *treatment height*, since it corresponds to the maximum height, and is one of the geometric parameters varied in the study.

$$\tan \Lambda = \frac{h}{(L - h)} \quad (2.11)$$

In varying the height, the *leading edge angle*, defined in figure 2.18a and equation 2.11 as Λ , was also varied. For finlets, the angle is defined using the ratio of the height, h , and the distance to the maximum height, $L - h$. Note that this is the same angle as defined in chapter 1 for the studies by Clark *et al.* [1, 2]. For the Rail treatment, the angle is defined including the 10 mm extension, e.g. $h/(L + 10\text{mm})$. Quantifying this leading edge angle will be helpful in comparing treatments where the treatment length is varied. The leading 12.7 mm of the substrate were intentionally left flat to fair the finlet to the trailing edge surface with 0.1 mm thick foil tape.

This design was selected to match the proven “F0” and “F8” finlet treatments used in the recent airfoil experiment by Clark *et al.* [1]. In that study, the F8 treatment reduced the integrated noise levels (from 1500-5000 Hz) by 5.4 dB at the zero-lift angle of attack. At 3 kHz and $\alpha = -2.5^\circ$, the F8 treatment reduced the noise by about 10 dB. The drag increased by 10% relative to the clean airfoil, proportional to the increase in wetted area associated with adding the finlets. Lift curves for the “F0” case showed that the finlets had no effect until post-stall, where the lift was actually increased slightly. Using slightly thicker finlets with the same profile slightly decreased the lift curve [2].

Because of its well-documented, robust performance, this design was used as the Baseline finlet in this experiment. A close-up image of the finlet treatments used here, as well as the nomenclature used to describe the treatments, is shown in figure 2.17. The height, h , refers to the distance from the substrate surface to the highest point of the treatment. The thickness, t , refers to the thickness of a single finlet, and the channel spacing, s_c , is defined as the wall-to-wall distance within a channel. These parameters are all constant within a single finlet design; for example, adjacent channels would have the same s_c , t , and h . The

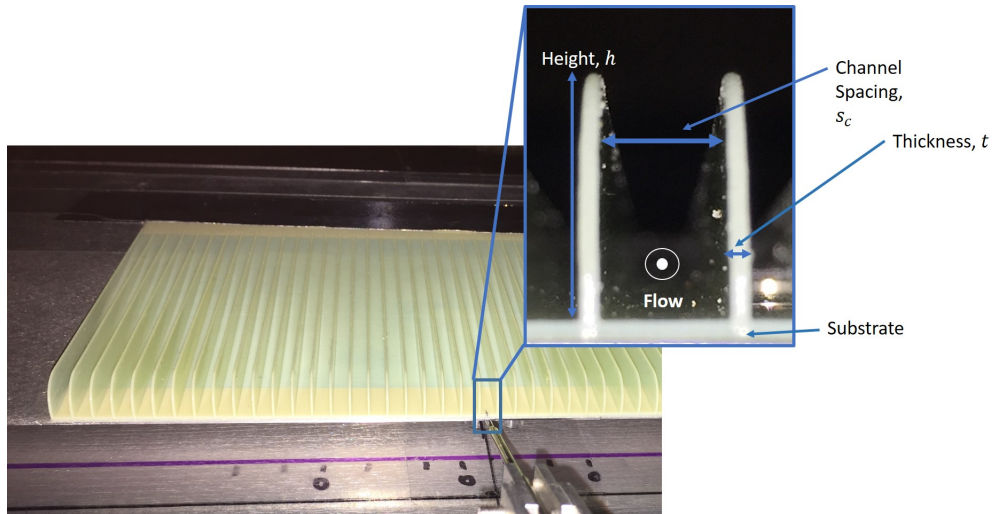


Figure 2.17: Baseline finlet treatment applied to the mock trailing edge, with a hot-wire probe downstream. The inset image shows the nomenclature used for the finlet and rail treatments.

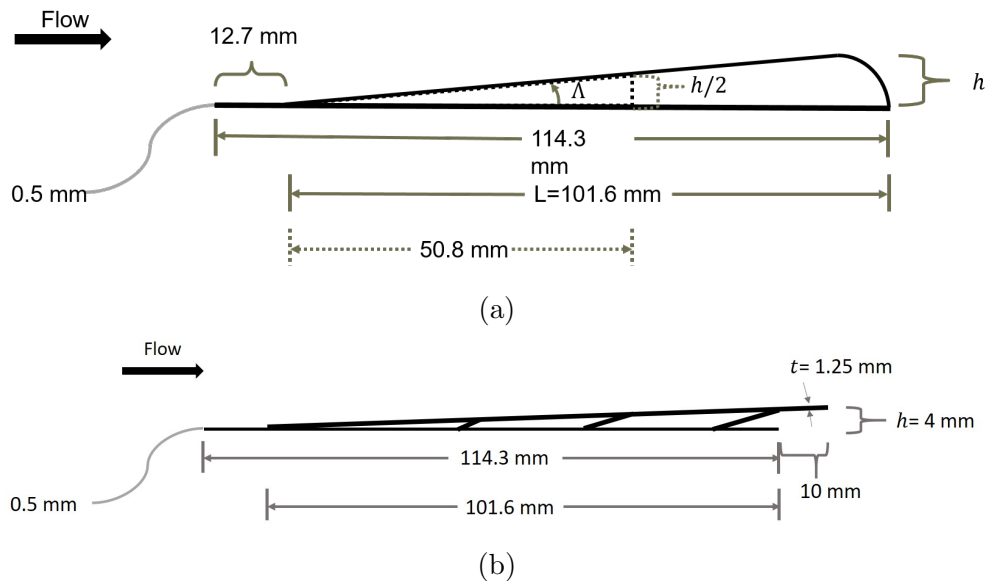


Figure 2.18: **(a)** Side view of the finlet treatment design. The treatment height, h , was one of the parameters varied in the study. The dashed lines are used to indicate the location and dimensions of the “mid-plane” finlets used to document the flow along a channel. Mid-plane pieces were only made for the Baseline and Short finlet designs. **(b)** Rail treatment, with the same design parameters as the “R0” treatment described in Clark *et al.* [1].

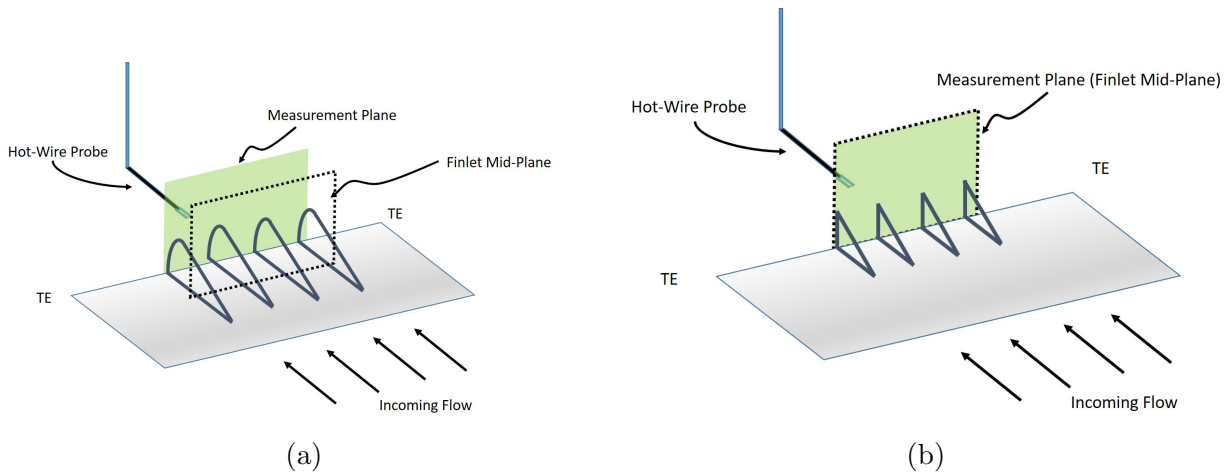


Figure 2.19: Schematic of the hot-wire measurements downstream of (a) the full Baseline finlet, and (b) the mid-plane of the Baseline finlet.

Baseline finlet design was 8 mm tall, with 4 mm spacing and 0.5 mm thickness (consistent with “F8” in Clark *et al.* [1]). Based on manufacturing constraints, the finlets could not be any thinner than 0.5 mm. This thickness was chosen because of its prevalence in previous finlet studies, where it was shown that thickening the finlets decreased lift when applied to an airfoil[2]. The rest of the finlets tested here were modified versions of the Baseline case, either by varying the height, spacing, or thickness. The modified designs were named “Short,” “Dense,” and “Thick,” respectively. The Short finlets had h reduced to 4 mm, keeping the other parameters the same as the Baseline case (consistent with “F0” in Clark *et al.* [1]). The 8 mm tall F8 finlets were reported to be about 2 dB quieter than the 4 mm F0 finlets throughout the same frequency range [1].

The effect of finlet thickness on the acoustic and aerodynamic performance was also investigated by Clark *et al.* [2], varying this parameter from 0.5 mm to 1 mm. The 1 mm-thick finlets tended to reduce the lift compared to the untreated case, particularly at high angles of attack, in contrast to the 0.5 mm finlets. To further characterize the effect of finlet thickness, the Thick finlets in this experiment were designed to have a thickness of $t= 1$ mm, twice that of the Baseline finlet case.

$$OAR = \frac{s_c}{s_c + t} \quad (2.12)$$

The Dense finlet spacing, $s_c= 2$ mm, was chosen to ensure that the open-area ratio (OAR) was the same as the Thick finlet; thickness was reverted to 0.5 mm for this design. The open-area ratio, defined in equation 2.12, was 0.89 for both the Baseline and Short finlet treatments, whereas the Thick and Dense treatments have an OAR of 0.8. Additional motivation for testing finlets with 2 mm spacing is found in Clark *et al.* [1], where it was hypothesized that a certain minimum spacing between 1-4 mm would cause the treatment to behave like a solid,

blunt trailing edge and shed vortices. The relevant design parameters for each treatment are summarized in table 2.3. It’s important to emphasize that no flow measurements had been reported.

The Rail treatment consists of a series of swept cylindrical protrusions (diameter $t = 1.25$ mm) with a spacing of $s_c = 2.5$ mm, and a 10 mm extension beyond the substrate trailing edge. The rails are held up by three different cylindrical supports, also with a 1.25 mm diameter. A schematic is shown in figure 2.18b. The main differences between the rails and the finlets are that the rails do not have any curvature to their upper edges, and that there are small gaps between the main rail protrusion and the substrate. This design was chosen to more closely mimic owl hairs, replicating the “R0” design tested previously [1], which matched the F0 performance. The integrated levels (1500-5000 kHz) were reduced by 3.9 dB (compared to 4 dB for the F0 finlets) and the attenuation was also about 10 dB at 3 kHz [1]. The OAR is 67%, designed to closely approximate that seen in the canopy of a Great Gray owl feather [1]. The Rail design parameters are also included in table 2.3.

Mid-Plane of the Baseline Finlet

To reveal the flow structure as a function of distance along the finlets, measurements were made at the mid-plane of the Baseline finlet treatment. This was done by printing just the leading 50% of the Baseline treatment and placing it at the trailing edge. The dimensions of the “mid-plane” piece are shown using the dotted lines in figure 2.18a. Figure 2.19 shows a schematic of the hot-wire measurement downstream of the full Baseline treatment and at its mid-plane. This was done to simulate traversing the probe along a finlet channel. In doing this, the implicit assumptions are that the effects of the rounded treatment trailing edge are not communicated upstream, and that treatment performance is not highly sensitive to the location of the treatment leading edge. There is some evidence of this in the recent acoustic measurements by Clark *et al.*, where finlets were placed at 85% chord, and no significant change in the attenuation was reported [1]. The mid-plane treatments described here were only used for flow measurements, not acoustics.

Table 2.3: Treatment Design Parameters

Treatment	Height, h [mm]	Spacing, s_c [mm]	Thickness, t [mm]	O.A.R. [%]	L.E. Angle, Λ
Baseline	8	4	0.5	89	4.9°
Short	4	4	0.5	89	2.3°
Dense	8	2	0.5	80	4.9°
Thick	8	4	1	80	4.9°
Rail	4	2.5	1.25	67	2.1°

2.7 Experimental Uncertainty

Jet Velocity

Uncertainty in the wall jet and CTA calibration jet were estimated to be 0.5% and 1%, respectively. These values were estimated by assuming a perfect gas and perturbing the ambient temperature, ambient pressure, and dynamic pressure in equation 2.13 and observing the response. To be conservative, the quoted relative uncertainties were estimated by normalizing the perturbation response on the lowest tested flow speed.

$$U = \sqrt{\frac{2qRT}{P}} \quad (2.13)$$

Microphone Measurements

As mentioned in chapter 2, both the far-field and surface pressure fluctuation microphone units were sampled at 65536 Hz for 32 seconds. The one-sided power spectral density, G_{pp} , was computed using a Hanning window with 50% overlap and 8192 samples per record, giving approximately $N_{rec} = 512$ records. The uncertainty in dB can be estimated as follows. Starting with the definition of SPL given in equation 2.7, we can express this in terms of \log_e as in equation 2.14.

$$\text{SPL} = \frac{10}{\log_e(10)} \left(\frac{G_{pp}}{p_{\text{ref}}^2} \right) \quad (2.14)$$

Differentiating this expression with respect to the autospectrum, G_{pp} , (assuming the uncertainty in the reference pressure $\delta_{p_{\text{ref}}=0}$), the uncertainty can be written as:

$$\delta_{\text{SPL}} = \left| \left(\frac{\partial \text{SPL}}{\partial G_{pp}} \right) \delta_{G_{pp}} \right| \quad (2.15)$$

where $\delta_{G_{pp}}$ is the uncertainty in the spectral estimate. At 95% confidence, the spectral uncertainty is

$$\delta_{G_{pp}} = \frac{2G_{pp}}{\sqrt{N_{\text{rec}}}} \quad (2.16)$$

Now, with

$$\frac{\partial \text{SPL}}{\partial G_{pp}} = \frac{10}{\log_e(10)} \frac{1}{G_{pp}}$$

we can substitute this result along with equation 2.16 into equation 2.15 to obtain an uncertainty of

$$\delta_{\text{SPL}} = \frac{20}{\sqrt{N_{\text{rec}}} \log_e(10)} = 0.38 \text{ dB}$$

Conservatively, then, the uncertainty in both the far-field and surface pressure SPL will be assumed to be 0.5 dB. For the background-subtracted far-field SPL spectra, the uncertainty is estimated to be 2 dB based on the signal-to-noise ratio, and this will be the cutoff used for presenting background-subtracted data.

Hot-Wire Measurements

The y - and z - locations of the probe were measured with a Gaertner Scientific Corporation optical tool (serial number 3408-A) placed at the downstream end of the smooth wall. With this instrument, the probe locations reported here have an uncertainty of ± 0.5 mm. Because of this uncertainty, the probe could not be aligned exactly downstream of the trailing edge (12.7 mm above the wall). In some cases, data near the edge ($12.7 < y < 13.2$ mm) could not be recorded. However, this does not detract from the experimental findings, and the flow near the tops of the treatments was resolved well.

The relative uncertainty in the mean hot-wire velocity was found to be $\pm 3.1\%$ using the method described by Jorgensen [33]. The reported uncertainty is based on a combined standard uncertainty multiplied by a coverage factor of 2, providing a level of confidence of about 95%. This uncertainty includes contributions in the calibration jet velocity, King's law fit, analog-digital conversion, temperature variation, and the averaging process. Contributions from the ambient pressure, humidity, and probe angular position relative to the x -axis were neglected. The uncertainty due to temperature variations and analog-digital resolution were assumed to have a square distribution. The dominant sources of uncertainty were the calibration jet speed and the temperature variation, less than 2 degrees Celsius (recall that the temperature variation is corrected with the method of Bearman [32]).

The relative uncertainty in the turbulence intensity values was found to be $\pm 4.36\%$, by combining uncertainty in the mean velocity with the averaging uncertainty in the root-mean-square. As before, the reported uncertainty was based on a combined standard uncertainty multiplied with coverage factor of 2, for a confidence interval of approximately 95%. These uncertainties are conservative and represent an upper limit. For reference, the averaging uncertainties in the mean and root-mean-square are given in equations 2.17 and 2.18, respectively. The number of samples is denoted by N , the mean quantity is given by \bar{a} , and the root-mean-square is denoted as $\sqrt{\hat{a}'^2}$. The hat is used indicate the estimated quantity.

$$\delta(\hat{\bar{a}}) = \frac{2\sqrt{\hat{a}'^2}}{\sqrt{N}} \quad (2.17)$$

$$\delta \left(\widehat{\sqrt{a'^2}} \right) = \frac{\sqrt{2}\sqrt{a'^2}}{\sqrt{N}} \quad (2.18)$$

2.8 Test Plan

The test plan is summarized in table 2.4. Far-field sound, hot-wire, and surface pressure fluctuations were made for the clean wall, untreated trailing edge, and treated trailing edge. Note that hot-wire measurements were made independently of the acoustic measurements, as the traverse system self-noise would contaminate the findings. Only the center 228.6 mm of the mock trailing edge were treated. Surface pressure fluctuation measurements were made with two microphones placed at various positions listed in the table, corresponding to figure 2.5b. The far-field and surface pressure measurements were made for jet speeds ranging from 20-60 m/s in 10 m/s increments, using multiple treatments pieces to cover the full span of the mock trailing edge.. The hot-wire measurements were made at $U_{ref} = 50$ m/s. Hyphens are used in the table to indicate conditions that were not measured.

Table 2.4: Experiment test plan, showing the test cases, jet speeds at which data was taken, and positions of surface pressure instrumentation, referencing figure 2.5b.

Test Case	Far-Field	Hot-Wire	Surface Pressure Fluctuations	
			<i>Speed</i>	<i>Position</i>
Clean Wall	20-60 m/s	50 m/s	20-60 m/s	5-6, 5-4, 5-3, 5-2, 5-1, 4-7, 4-8, 4-9
Untreated T.E.	20-60 m/s	50 m/s	20-60 m/s	5-6, 5-4, 5-3, 5-2, 5-1, 4-7, 4-8, 4-9
T.E. with Baseline Finlet	20-60 m/s	50 m/s	20-60 m/s	5-6, 5-4, 5-3, 5-2, 5-1, 4-7, 4-8, 4-9
T.E. with Baseline Finlet at Mid-Plane	-	50 m/s	-	-
T.E. with Thick Finlet	20-60 m/s	50 m/s	20-60 m/s	4-7, 4-8, 4-9
T.E. with Dense Finlet	20-60 m/s	50 m/s	-	-
T.E. with Short Finlet	-	50 m/s	-	-
T.E. with Short Finlet at Mid-Plane	-	50 m/s	-	-
T.E. with Rail	-	50 m/s	-	-

Chapter 3

Results and Discussion

3.1 Far-Field Noise

3.1.1 Facility Acoustic Performance

Before presenting the results for the mock trailing edge, it is useful to examine in detail the background performance of the wall jet facility without the mock trailing edge assembly installed. Note that the terms “background” and “smooth wall” will be used interchangeably. Examining the background noise spectra at a given speed will help illustrate the expected trends for measurements in this facility and motivate the way ensuing acoustic results are presented. The spectral background levels at each measured velocity are shown in figure 3.1 for the center-plane microphone at $\theta = 123.5^\circ$. Throughout the experiment, a total of nine repetitions of the smooth wall acoustic measurements were made for each flow speed, 20-60 m/s in 10 m/s increments. All nine are over-plotted in figure 3.1. This was done to confirm that the wall jet was behaving as expected, and the results serve to highlight the preciseness and repeatability of measurements. For a given speed, the SPL generally does not vary by more than about 0.75 dB. The figure illustrates that the anechoic facility is a very stable testing environment.

The integrated sound levels for all nine repetitions at each speed are shown in figure 3.2 as a function of nominal jet velocity, U_{ref} , along with the classical dipole (U_{ref}^6) and quadrupole (U_{ref}^8) acoustic source scalings. The integration was done for two distinct low- and high-frequency ranges (200-700 Hz, figure 3.2a, and 700-20000 Hz, figure 3.2b), to clarify the contribution of the shear layer to the background noise levels. As would be expected based on the broadband spectra, the integrated low-frequency levels are consistently higher than the corresponding high-frequency levels, generally by 12-15 dB. In both cases (figures 3.2a - 3.2b), the integrated levels are strongly quadrupole in nature above $U_{ref} = 30$ m/s, varying by no more than 2 dB from the U_{ref}^8 scaling. This may suggest that background noise is

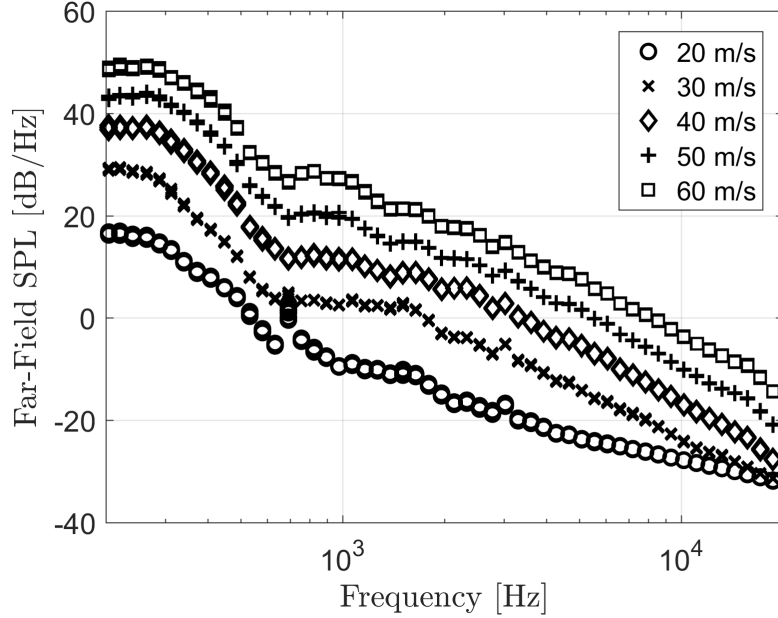


Figure 3.1: Far-field sound spectra for the clean wall cases, as measured by the microphone at $\theta = 123.5^\circ$. Nine different repetitions were performed for each speed.

primarily due to turbulence. For the lower speeds, the background levels are near or below the $1/f$ electrical noise of the microphone unit, seen in the spectra for $U_{ref} = 20 - 30$ m/s in figure 3.1. This would explain the deviation from the U^8 curve in figure 3.2b at the lowest speeds.

The directivity patterns based on the stream- and spanwise observer locations are shown in figure 3.3 for a representative case at $U_{ref} = 50$ m/s, the speed at which hot-wire measurements were performed. Figures 3.3a-3.3b show the narrowband SPL spectra between 200 Hz and 20000 Hz, and figures 3.3c-3.3d show the integrated SPL between 700 Hz and 20000 Hz. The integrated SPL is defined in equation 3.1, where G_{pp} is the one-sided power spectral density, df is the corresponding frequency spacing, p_{ref} is the reference pressure (20 μ Pa) and the limits of integration are chosen to be f_0 and f_1 in units of Hz.

$$10 \log_{10} \left(\frac{1}{p_{ref}^2} \int_{f_0}^{f_1} G_{pp}(f) df \right) \quad (3.1)$$

First, examining the spectra as a function of spanwise microphone location (figure 3.3b), it becomes clear that the noise does not vary appreciably above about 1000 Hz; below that, the biggest change as ϕ is decreased (moving in the $+z$ direction), is by about 5 dB at 300 Hz. The directionality in the streamwise direction is much more pronounced (figure 3.3a). As the angle θ is decreased (moving in the downstream direction), two distinct low- and high-

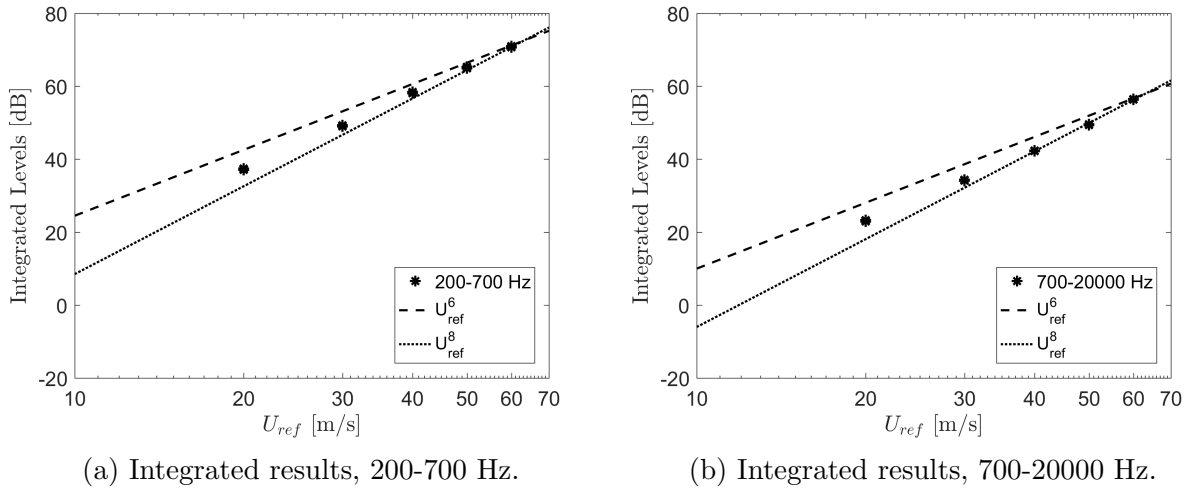
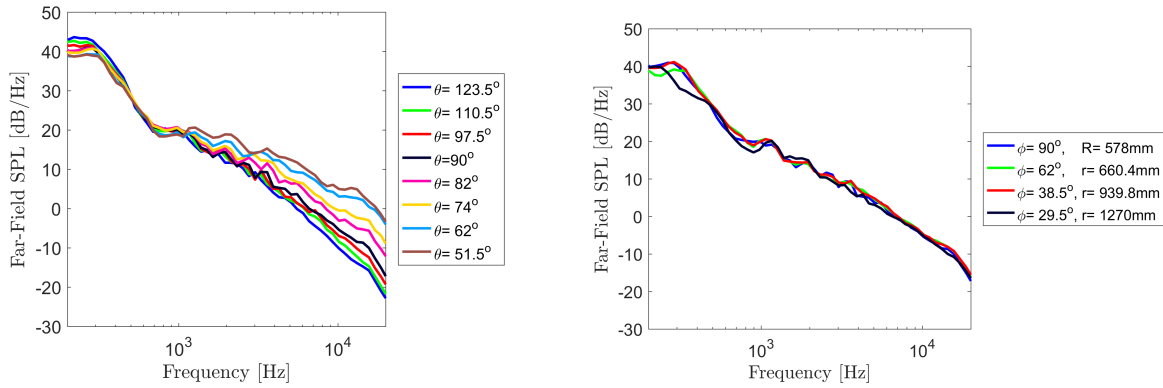


Figure 3.2: Integrated sound levels for the clean wall cases, measured by the microphone at $\theta = 123.5^\circ$. Nine different repetitions were performed for each speed and included in the figures, demonstrating the repeatability of the acoustic measurements in this facility. Simulated quadrupole (U_{ref}^8) and dipole (U_{ref}^6) results are included for reference.

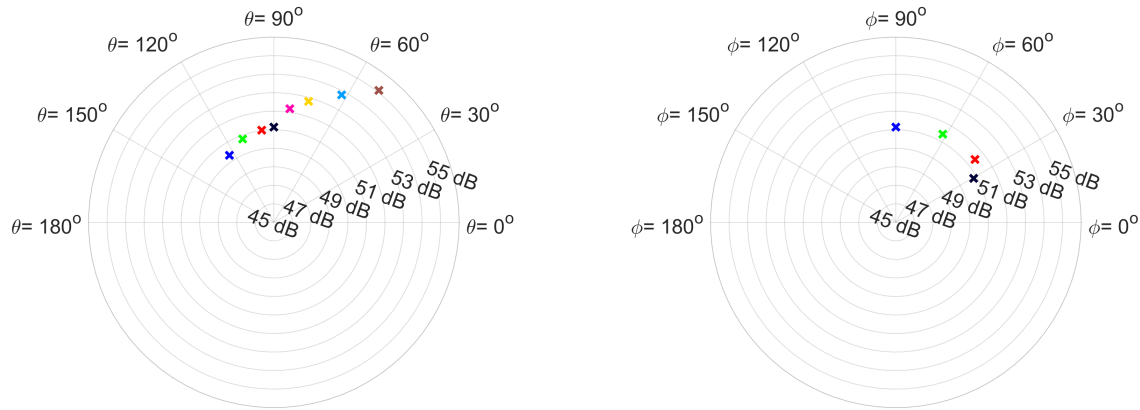
frequency patterns emerge. Below about 700 Hz, the noise decreases by up to about 4.5 dB as the observer moves downstream (as θ decreases). Above 700 Hz, the noise *increases* with decreasing θ . The difference in noise level measured by the upstream ($\theta=123.5$ degrees) and downstream ($\theta=51.5$ degrees) microphones increases strongly with frequency. For example, at 2000 Hz, the difference in SPL is roughly 7 dB; at 10000 Hz, the difference is almost 15 dB.

This can be explained by considering the facility configuration. The microphones are shielded from nozzle noise by the vertical and horizontal baffles pictured in 2.2. Because the microphones in the streamwise array are in the same plane, they experience similar background noise levels. Within the streamwise array, the upstream $\theta = 123.5^\circ$ microphone is least exposed to the nozzle noise. This explains the significant directionality above about 700 Hz. Below that, the noise is dominated by the shear layer created when a wall jet is exhausted into still air. Thus, to get a more accurate picture of the background noise directionality, the integrated levels are shown in figures 3.3c-3.3d, where the integration was performed between 700 and 20000 Hz to neglect the shear layer effects. Including the shear layer noise would skew the results toward the low-frequency behavior. As expected based on the spectra, the background noise measured by the streamwise array increases by about 5 dB as θ decreases. For this reason, the acoustic results will only be shown for $\theta = 123.5^\circ$, where the background noise is lowest, except when analysis of the directivity is needed. The spanwise levels only vary by about 1 dB.



(a) Streamwise directivity, background spectra.

(b) Spanwise directivity, background spectra



(c) Streamwise directivity, integrated back-ground spectra.

(d) Spanwise directivity, integrated background spectra.

Figure 3.3: Far-field sound directivity pattern for the background (smooth wall) configuration, shown for $U_{ref} = 50$ m/s. Note that the streamwise array of eight microphones has a constant $R=578$ mm radius. **(a-b)** Far-field spectra as a function of stream- and spanwise observer angle, respectively. **(c-d)** Integrated spectra ($f_0 = 700$ Hz to $f_1 = 20000$ Hz) as a function of stream- and spanwise observer angles, respectively. Angles are consistent with the coordinate systems defined in figure 2.9.

3.1.2 Untreated Trailing Edge Noise

Figure 3.4 shows the noise spectra produced by the untreated mock trailing edge as well as the background, smooth wall noise. There are two distinct peaks created by the trailing edge, between 1-3 kHz, and 4-8 kHz. The first peak, centered around 1.9 kHz, is generally about 6-9 dB louder than the clean wall. The second peak, centered around 5.5 kHz, is generally about 5 dB louder than the clean wall. The remaining spectra will be presented with the background noise subtracted, using the smooth wall sound spectrum at the corresponding jet speed. This ensures that the background noise from the shear layer and nozzle exit is removed and makes interpreting the results more intuitive. Subtracted data is only presented when the signal-to-noise ratio is greater than 2 dB. For reference, the signal-to-noise ratio (SNR) for the untreated trailing edge at $U_{ref} = 50$ m/s is shown in figure 3.5, with the 2 dB cutoff indicated by a horizontal, dotted line. The microphone at $\theta = 123.5^\circ$ consistently has the highest SNR, as expected. Further, using a 2 dB cutoff would suggest that background subtracted results should generally only be expected for frequencies above 1500 Hz. Note that the SNR is significantly worse in the spanwise array. The trends are consistent with the background noise as presented in figures 3.3c-3.3d .

To examine the noise peaks more closely, the sound spectrum at $U_{ref} = 40-60$ m/s is compared to a trailing edge noise prediction using the method of Brooks, Pope, and Marcolini [4] described in Chapter 1. Since the Brooks, Pope, and Marcolini predictions were presented in 1/3-octave form, they have been scaled to narrowband (1 Hz bandwidth) spectra for comparison with the measured data. Although the semi-empirical prediction method was developed for a NACA 0012 airfoil, specifying $\alpha = 0^\circ$ and using the displacement thicknesses in table 2.2 allows for simulation of the mock trailing edge noise. The mock trailing edge piece was modeled as a flat plate, and the prediction input parameters are given in table 3.1. Note that the observer angle is entered using the coordinate system with $\theta = 0^\circ$ pointing upstream, consistent with the prediction method development. The simulations are made for the microphone at $\theta = 123.5^\circ$ in figure 2.9 based on the above discussion showing that the signal-to-noise ratio here was highest.

The prediction velocity was chosen to be the local U_m as given by the Wygnanski relations in table 2.2, as was the displacement thickness. The choice to use U_m rather than U_{ref} was appropriate given that for a wall jet, the velocity decays appreciably with increasing x . Distance from the trailing edge to the observer was assumed to be the streamwise array radius, $R = 578$ mm.

In essence, choosing to use this prediction tool with the inputs in table 3.1 is equivalent to choosing to make the following assumptions: the presence of the transition ramp and trailing edge piece do not drastically alter the parameters estimated with Wygnanski's method in table 2.2, that U_m is the representative speed at the trailing edge, that the microphone at $\theta = 123.5^\circ$ points directly at the trailing edge (see figure 2.9a). The predicted noise levels are compared to the measured noise spectra in figure 3.6 for $U_{ref} = 40, 50, \text{ and } 60$ m/s. Note that the measured data have been background subtracted. The TBL-TE predictions (dotted

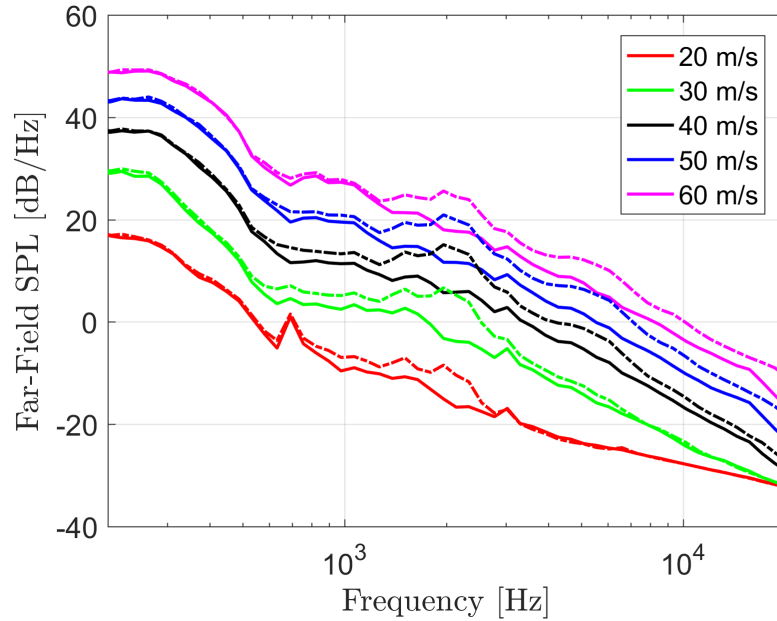


Figure 3.4: Clean wall (solid) and untreated trailing edge (dash-dot) far-field sound spectra are shown for all measured speeds. The legend shows the colors corresponding to each speed. The microphone is at $\theta = 123.5^\circ$.

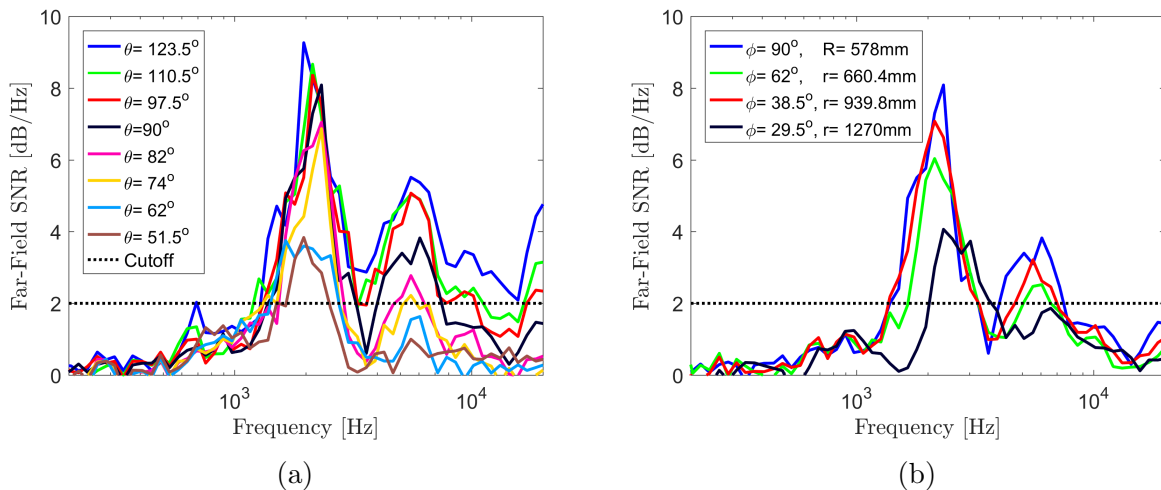


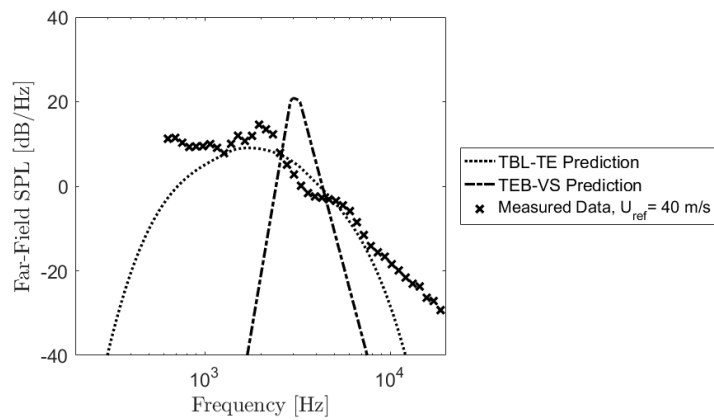
Figure 3.5: Signal-to-Noise ratio using the untreated trailing edge and background noise levels in the (a) streamwise direction, and (b) spanwise direction. Levels are shown for $U_j = 50$ m/s

Table 3.1: Brooks, Pope, and Marcolini [4] trailing edge noise (TBL-TE and TEB-VS) prediction parameters.

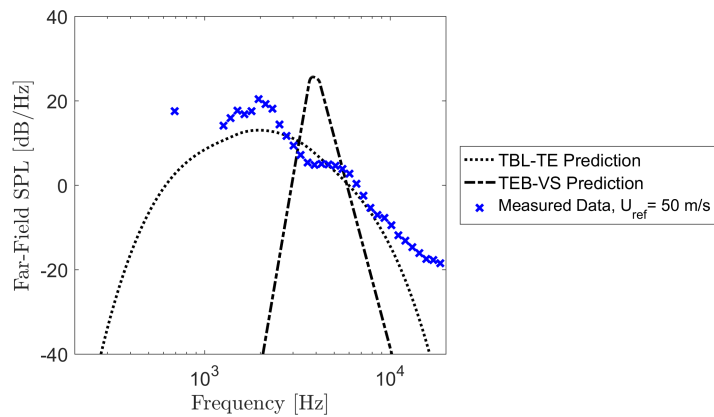
Chord [mm]	114.3
Span [mm]	971.55
α [deg.]	0
Sound speed [m/s]	340
Kinematic Viscosity [m^2/s]	$1.6482 \cdot 10^{-5}$
Observer angle, $180-\theta$ [deg.]	56.5
Lateral directivity, ϕ [deg.]	90
Distance from TE to observer [mm]	578
U_m [m/s]	13.65, 17.3, 20.98 (table 2.2)
Displacement thickness [mm]	0.89, 0.86, 0.83 (table 2.2)
Trailing edge thickness, t_{TE} [mm]	0.76
h/t_{TE}	0.85, 0.88, 0.92

Table 3.2: Brooks, Pope, and Marcolini [4] Predicted Peak Frequencies.

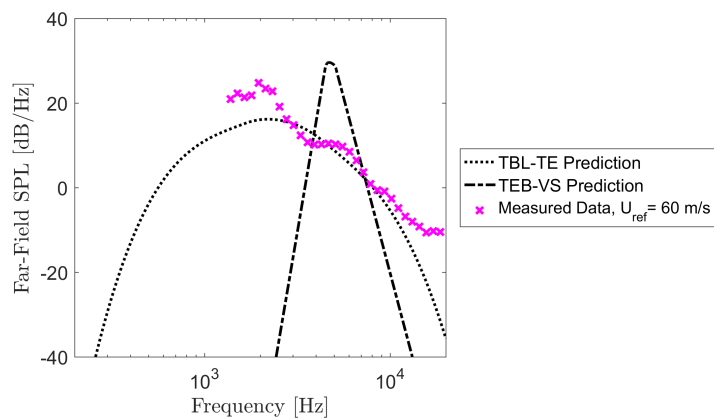
U_{ref} [m/s]	U_m [m/s]	TBL-TE f_{peak} [Hz]	TEB-VS f_{peak} [Hz]
40	13.65	1720	3010
50	17.3	1960	3840
60	20.98	2200	4690



(a)



(b)



(c)

Figure 3.6: Comparison of measured, background-subtracted far-field noise spectra (\mathbf{x}) and a BPM prediction [4] for turbulent boundary layer-trailing edge noise (TBL-TE, dotted line) and trailing edge bluntness-vortex shedding noise (TEB-VS, dash-dot) at $\alpha = 0^\circ$ for **(a)** $U_{ref} = 40$ m/s, **(b)** $U_{ref} = 50$ m/s, **(c)** $U_{ref} = 60$ m/s. Additional simulation inputs are given in table 3.1.

line) show little agreement with the measured data for any of the velocities presented ($U_j=40-60$ m/s). The peak SPL levels are dissimilar; equally important, the spectral shapes do not align well. This may be due in part to the simplifying assumptions made and the nature of the prediction, developed for a NACA 0012 airfoil. However, it does not appear that the noise generated by the mock trailing edge is true “trailing edge noise” in the way it was presented in section 1.3, chiefly because the frequency associated with the first noise peak is constant. A similar analysis was performed for the second noise peak, centered about 5.5 kHz, under the initial belief that it may be trailing edge bluntness-vortex shedding (TEB-VS) noise. The trailing edge thickness, t_{TE} , is 0.76 mm, and the ratio h/t_{TE} is shown in table 3.1 for each U_j . The corresponding Brooks, Pope, and Marcolini prediction for TEB-VS noise is also shown in figure 3.6 with the dash-dot line. Here, the SPL are significantly over-predicted, and the predicted spectral shape is not consistent with what was measured. As with the previous noise peak, this is likely due to the fact that the frequency associated with the second noise peak (about 5.5 kHz) does not change with flow speed. For reference, the expected peak frequencies for TBL-TE and TEB-VS at each speed are shown in table 3.2. Note that U_m was used as the characteristic velocity in the Brooks, Pope, and Marcolini [4] predictions. The behavior of the untreated trailing edge noise peaks is seen more clearly in figure 3.7. The SPL values increase with increasing U_{ref} , and the peak frequencies don’t change, remaining constant at approximately 2 kHz and 5.5 kHz. Note that the simulations in figure 3.6 were done starting at $U_{ref}=40$ m/s because the signal-to-noise ratio was greater than 2 dB at higher frequencies.

Any velocity dependence in the measured spectra should become apparent when scaling the spectra, as shown in figure 3.8. The nondimensional frequency is taken to be the Strouhal number, defined in equation 3.2 (using the trailing edge thickness t_{TE} as the lengthscale rather than δ^* made no difference). In this manner, the scaling which preserves the integrated levels is presented in figure 3.8, where the power spectral density is normalized on the square of the local dynamic pressure at the trailing edge, $q_{TE} = \rho U_m^2$, multiplied by the local Mach number, M_{TE} . Scaling the pressure in this manner preserves the U^5 effects first pointed out by Ffowcs-Williams and Hall [16] and confirmed by Brooks, Pope, and Marcolini [4]. The full spectral scaling, with all terms included, is shown in equation 3.3. Practically speaking, this is simply the SPL, $10 \log_{10}(G_{pp}(f)/p_{ref}^2)$, normalized on some function of dynamic pressure, $10 \log_{10}\left(\frac{p_{ref}^2}{(qM_{TE})^2}\right)$, and multiplied by the *inverse* of the parameters used to nondimensionalize the frequency, $10 \log_{10}(U_m/\delta^*)$.

$$St = f\delta^*/U_m \quad (3.2)$$

$$\text{Scaled SPL} = 10 \log_{10} \left(\frac{G_{pp}}{p_{ref}^2} \frac{p_{ref}^2}{(\rho U_m^2 M_{TE})^2} \frac{U_m}{\delta^*} \right) \quad (3.3)$$

The last step is done to ensure that the integrated, nondimensionalized sound level is pre-

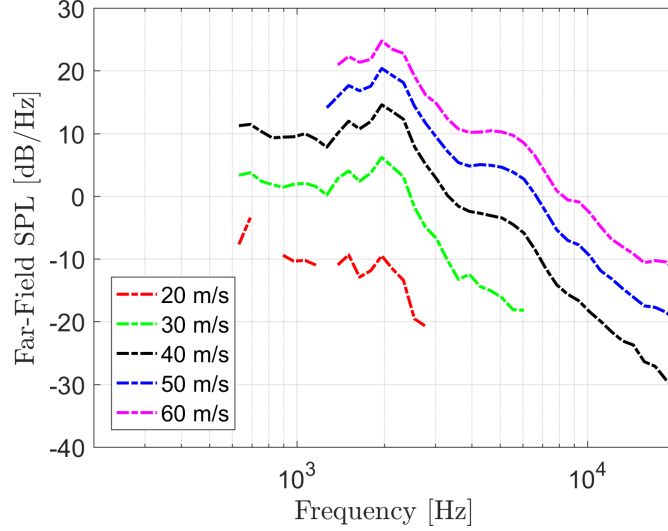


Figure 3.7: Background-subtracted trailing edge noise as a function of U_{ref} , measured with the microphone at $\theta = 123.5^\circ$. Data presented only where the signal-to-noise ratio exceeds 2 dB.

served i.e. so that integrating the scaled power spectral density as in equation 3.4 results in $p_{ms}/(\rho U_m^2 M_{TE})^2$. Equivalently, from a discrete perspective, what this means is that since the goal is to have the summation result in $p_{ms}/(\rho U_m^2 M_{TE})^2$, changing the frequency spacing from Δf to $\frac{\delta^*}{U_m} \Delta f$ implies that the spectral values must be changed by the corresponding factor U_m/δ^* . Here, p_{ms} is the mean-square pressure.

$$\frac{p_{ms}}{(\rho U_m^2 M_{TE})^2} = \int_{-\infty}^{\infty} \frac{1}{(\rho U_m^2 M_{TE})^2} G_{pp}(f) df = \int_{-\infty}^{\infty} \frac{1}{(\rho U_m^2 M_{TE})^2} \frac{U_m}{\delta^*} G_{pp}(f) d\left(\frac{f \delta^*}{U_m}\right) \quad (3.4)$$

Note that the local Mach number, is defined as M_{TE} in equation 3.5, where the ratio of specific heats is assumed to be $\gamma = 1.4$, the ideal gas constant for air is taken to be $R_{air} = 287 \text{ J}/(\text{kg}\cdot\text{K})$, and T is the jet flow temperature.

$$M_{TE} = U_m / \sqrt{\gamma RT} \quad (3.5)$$

In figure 3.8, the peak scaled SPL values vary by about 1.5 dB for $U_{ref} > 30 \text{ m/s}$. The peak Strouhal numbers do not agree. This is to be expected, since figure 3.7 showed that the peak frequencies were constant. Overall, these findings suggest that the noise generated by the mock trailing edge is at least partially influenced by the geometry, e.g. by interference between directly radiated sound and reflections off the wall. This could be explained in further detail through ray tracing or constructing a suitable Green's function. However, the

stated goal of the thesis is to identify the flow effects caused by the finlets and relate those changes to any reduction in far-field noise. In this context, it is sufficient to state that the noise generated by the untreated trailing edge has been clearly identified (figures 3.4-3.8) and briefly examine the trailing edge directivity before exploring any noise attenuation caused by the finlets and rails tested here.

The directivity of the sound from the untreated trailing edge at $U_{ref}=50$ m/s is shown in figure 3.9. No clear pattern emerges in the streamwise direction, particularly for $\theta < 90^\circ$ above about 3 kHz, where the SNR falls below the 2 dB cutoff for the background subtraction. In the spanwise direction, the effects from the low SNR also make it difficult to interpret the results. Near 2 kHz, the spectra appear to (loosely) follow the spanwise directivity of the smooth wall, where the measured SPL decreases with decreasing ϕ i.e. as the observer is moved away from the jet centerline.

3.1.3 Finlet Effects on Far-Field Sound

Figures 3.10a-3.10c show the background-subtracted noise spectra for the untreated and treated trailing edge measured by the microphone at $\theta = 123.5^\circ$ at $U_{ref} = 40, 50,$ and 60 m/s, respectively. Below these speeds, the signal-to-noise ratio (SNR) with the treatments applied is too low to draw effective conclusions. Even at $U_{ref}=40$ m/s (figure 3.10a), it is difficult to distinguish the between the background noise and noise from the trailing edge with the Baseline finlets. Because the background-subtracted data is only presented where the SNR is above 2 dB, the far-field spectra for the Baseline finlets on the trailing edge appear “choppy” because of frequencies corresponding to low SNR. In spite of this, there are some important observations to be made. First, for the velocities presented here, the Baseline, Thick, and Dense finlets were all effective at reducing the trailing edge noise. Note that the full span of the trailing edge was treated. As mentioned previously, the spectrum for the trailing edge with Baseline finlets applied is difficult to differentiate from the background noise at $U_{ref}=40$ m/s. The treated spectra with the Dense and Thick finlets are extremely similar at this speed. It is unclear why, at $U_{ref}=40$ m/s, the Dense finlets produce less attenuation than the Baseline finlets and as much as the Thick finlets (figure 3.10a). At higher speeds (figures 3.10b-3.10c) the Dense finlets clearly outperform the Baseline and Thick finlets. Part of the difficulty in explaining the differences in treated spectra between figure 3.10a and figures 3.10b-3.10c lies in the design parameters listed in table 2.3. The three designs used in acoustic measurements (Baseline, Thick, and Dense) had the same height, 8 mm. The Baseline and Thick finlets (blue and cyan, respectively), had the same spacing (4 mm) but different open-area ratios (89% and 80%). The results at $U_{ref}=40$ m/s in figure 3.10a might suggest that a larger open-area ratio is more effective (the Dense finlets also had an open-area ratio of 80%), and a better indicator of acoustic performance than the spacing. However, this is inconsistent with the findings at higher speeds (figures 3.10b-3.10c). There, it would appear that the spacing is the dominant parameter, as the Dense finlets (2 mm spacing) are more effective than the both the Baseline and Thick designs. Because the hot-

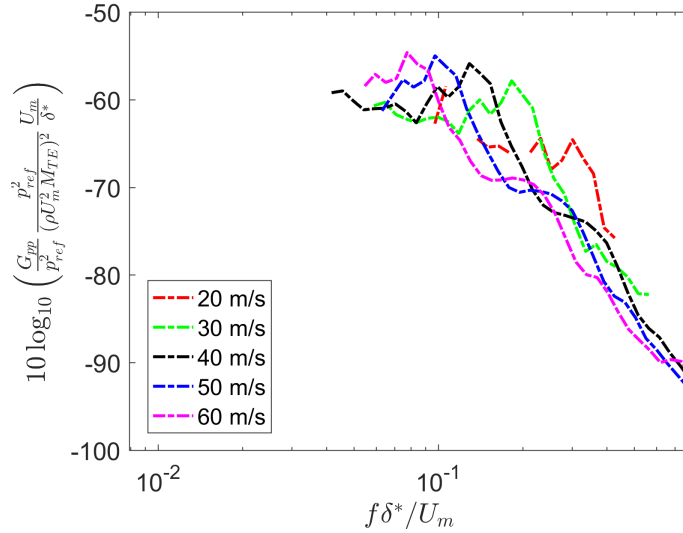


Figure 3.8: Background-subtracted far-field sound spectra for the untreated trailing edge, measured by the stream-wise microphone at $\theta = 123.5^\circ$.

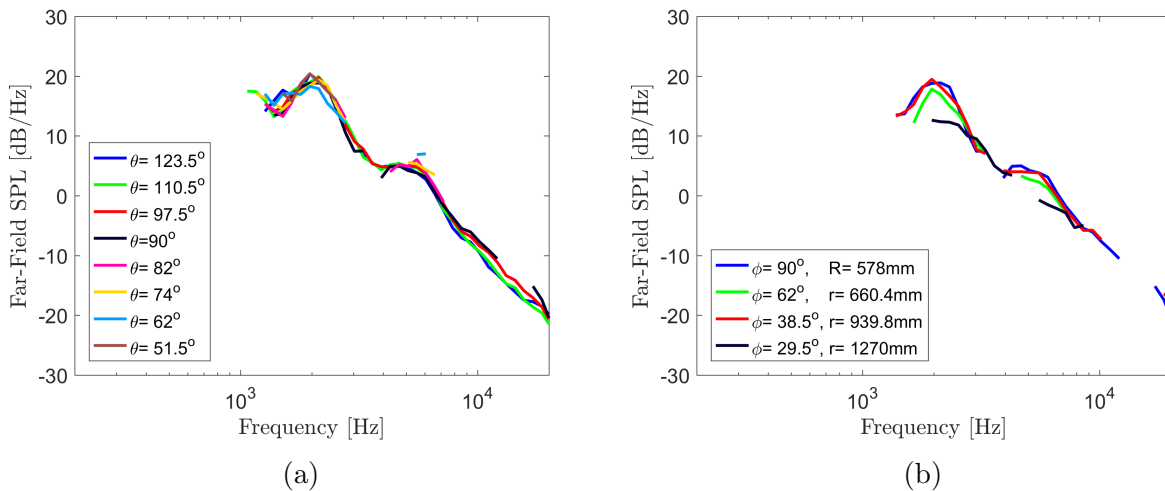
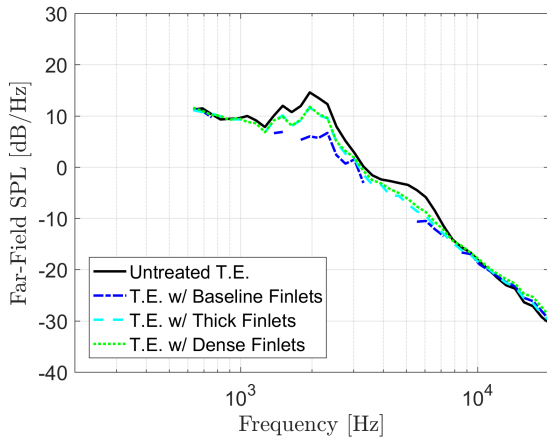
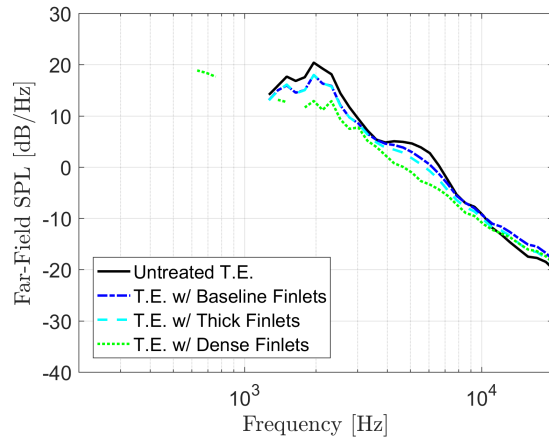


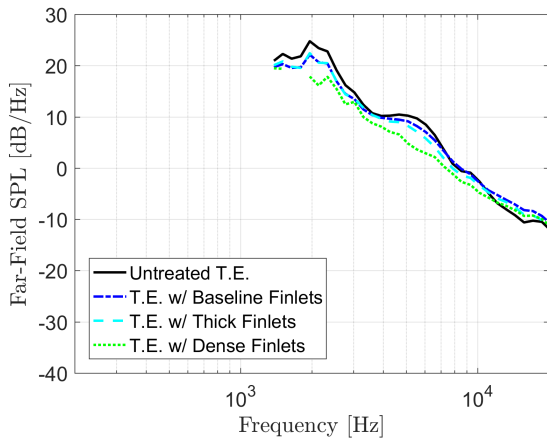
Figure 3.9: Far-field directivities in the **(a)** streamwise, and **(b)** spanwise directions for $U_{ref}=50$ m/s. Spectra have been background-subtracted and are only shown where signal-to-noise ratio is greater than 2 dB.



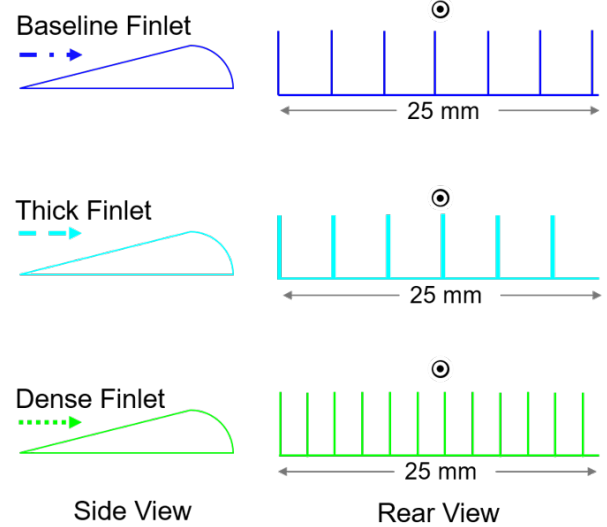
(a) Far-field sound spectra, $U_{ref} = 40$ m/s.



(b) Far-field sound spectra, $U_{ref} = 50$ m/s.



(c) Far-field sound spectra, $U_{ref} = 60$ m/s.



(d) Corresponding treatment geometry

Figure 3.10: Background subtracted far-field sound spectra for the mock trailing edge with and without Baseline, Thick, and Dense finlets applied, measured at $\theta = 123.5^\circ$. Data is only shown where the signal-to-noise ratio exceeds 2 dB. (a) $U_{ref} = 40$ m/s, (b) $U_{ref} = 50$ m/s, (c) $U_{ref} = 60$ m/s, (d) Relative treatment geometries, shown as side view (flow direction denoted by arrow) and rear view (flow is directed out of page). Dimensions given in figure 2.3

wire measurements were performed at $U_{ref} = 50$ m/s, the remaining analysis of the treated far-field spectra will be devoted to the case at $U_{ref} = 50$ m/s (figure 3.10b), in addition to the fact that the trends are similar to those seen in figure 3.10c for $U_{ref} = 60$ m/s.

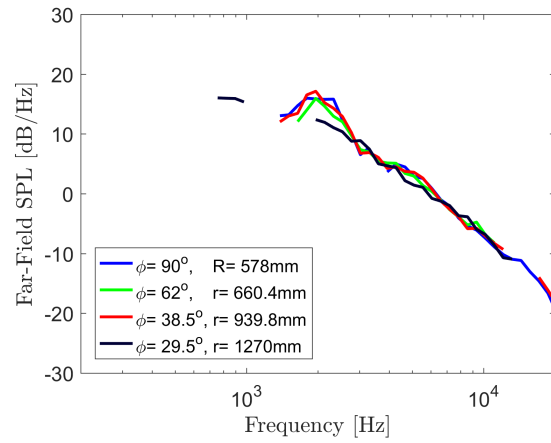
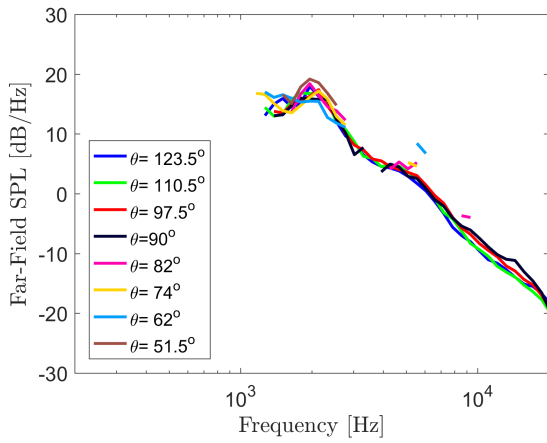
Each finlet design proved to be effective at reducing the trailing edge noise. Considering first the mid-frequency peak centered about 1.9 kHz, the noise is reduced by 2.4 dB with the baseline and thick finlets, and by 7.5 dB with the dense finlets. The second trailing edge noise peak, centered around 5.5 kHz, is reduced by 2.1 dB, 3.3 dB, and 7.2 dB with the Baseline, Thick, and Dense treatments, respectively. The effective frequency range of the finlets appears to be approximately 1.5-10 kHz; outside of this, they slightly increase the radiated sound (the lower limit on this effective frequency range is consistent with that reported by Clark *et al.* [1, 2]). At approximately 15 kHz, for example, the finlets add a maximum of about 2.7 dB. This noise increase is likely due to the 0.5 mm treatment substrate; auxiliary wall jet measurements performed by Ian Clark showed that a 0.5 mm thick piece of substrate spanning the 2-D flow region increased the noise relative to the smooth wall levels by up to about 5 dB at about 17 kHz. Within the effective frequency range (1.5-10 kHz), the baseline and thick finlets still exhibit the same spectral profile, with two distinct peaks. The Dense finlets, however, eliminate the second peak completely.

Examining the treated spectra more closely, some design considerations start to emerge. Clearly, a smaller spacing is desirable, as the Dense ($s_c = 2$ mm) finlets outperformed any other treatments. This also suggests that the spacing at which the finlets act like a blunt trailing edge is less than 2 mm. The thickness also has a noticeable impact, if not quite as significant. For example, between 1.2-3 kHz, there is virtually no difference between the spectra for the baseline and thick finlets. Above that range, the Baseline finlet is generally about 1 dB louder than the Thick finlet. Between 4-8 kHz, the Baseline and Thick finlets provide attenuation of about 2 and 3 dB, respectively. These findings imply that the spacing is the dominant parameter, and that for a fixed spacing, there is some potential to thicken the finlets, making them more robust for field work, although there may be a slight lift penalty when applied to airfoils [1].

Lastly, the SPL directivity for the treated trailing edge noise at $U_{ref} = 50$ m/s is shown in figures 3.11-3.13. As in the case of the untreated trailing edge directivity, the poor broadband SNR makes it difficult to identify any trends in the SPL directivity other than those associated with the smooth wall facility discussed at the beginning of this section. These trends were consistent across the various flow speeds.

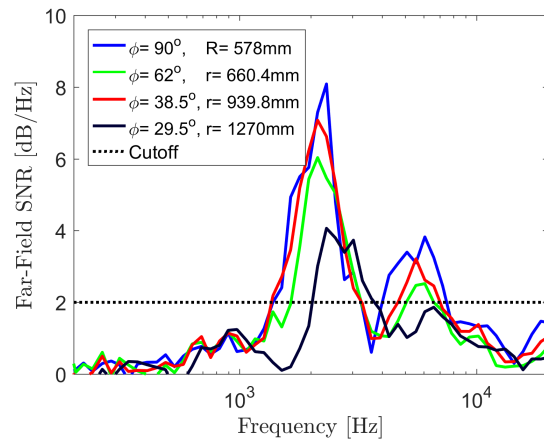
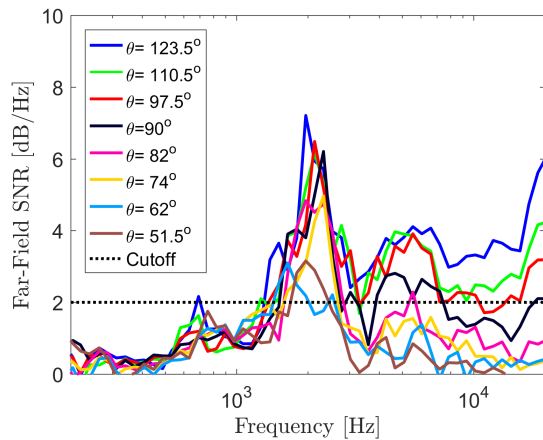
3.2 Hot-Wire Measurements

Since the acoustic results showed that the far-field sound shows some scaling with flow speed, it was not necessary to take hot-wire measurements at every flow speed. The results presented here are for a nominal jet exit velocity of 50 m/s, typically in terms of an adjusted



(a) Background-subtracted SPL spectra in the streamwise array, T.E. with Baseline finlet.

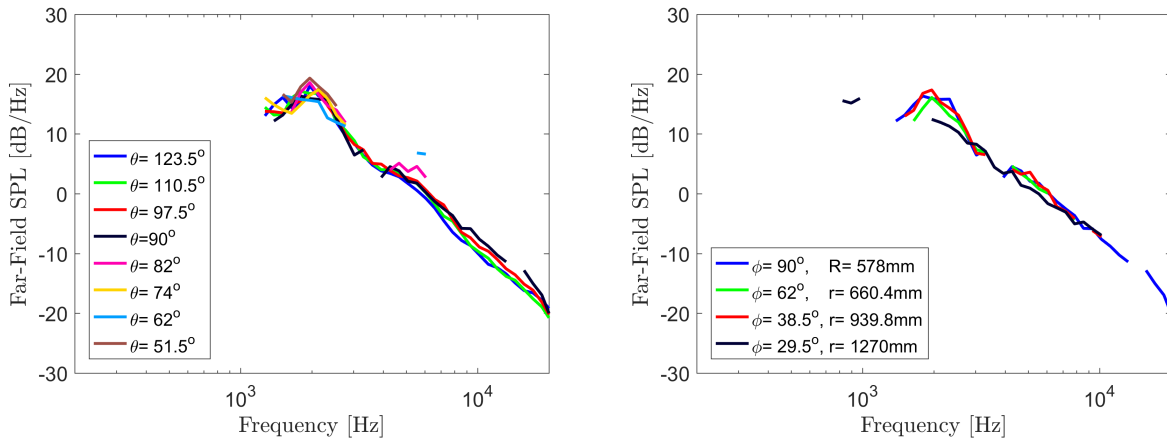
(b) Background-subtracted SPL spectra in the spanwise array, T.E. with Baseline finlet.



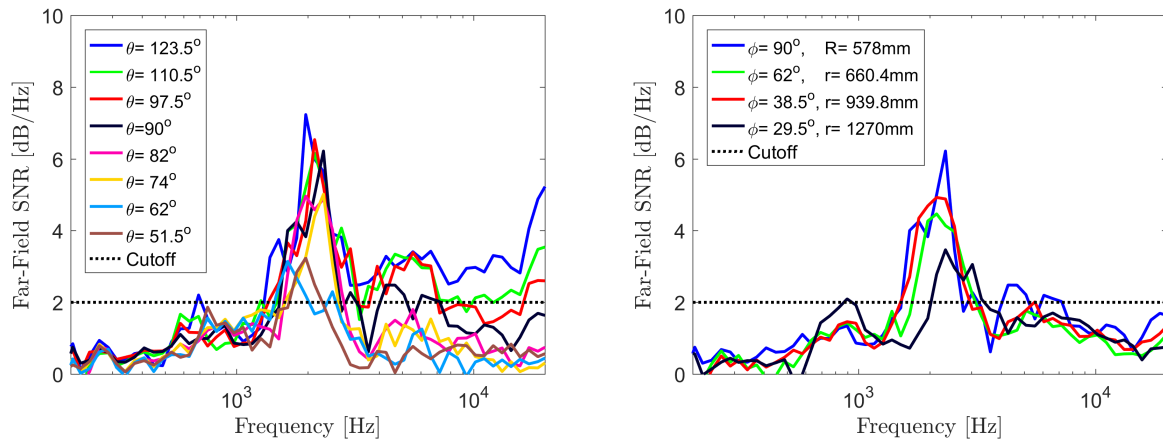
(c) Streamwise microphone array SNR, T.E. with Baseline finlet.

(d) Spanwise microphone array SNR, T.E. with Baseline finlet.

Figure 3.11: Signal-to-Noise Ratio (SNR) and background-subtracted SPL spectra at $U_{ref} = 50$ m/s for the trailing edge (T.E.) with Baseline finlets applied. Background-subtracted spectra are only shown for SNR > 2 dB. (a) SPL in the streamwise array, (b) SPL in the spanwise array, (c) SNR in the streamwise array, (d) SNR in the spanwise array.

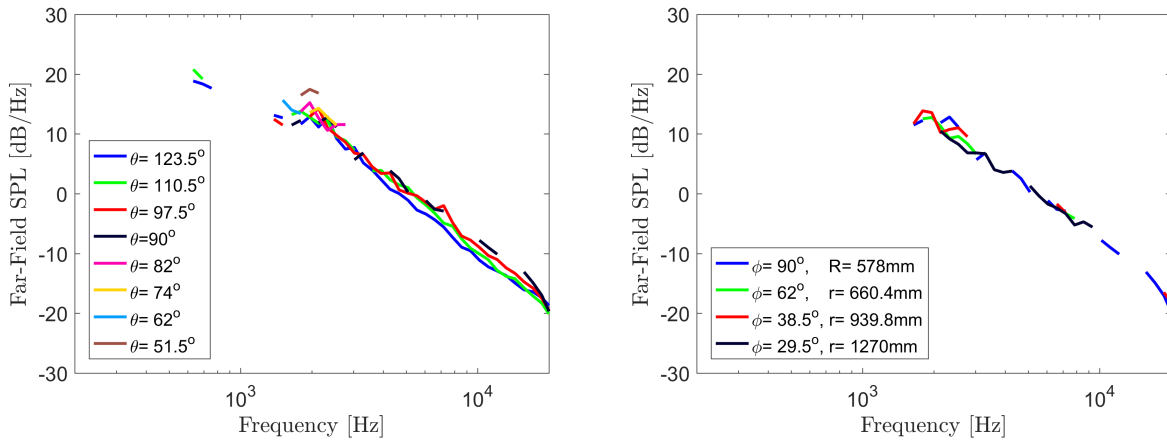


(a) Background-subtracted SPL spectra in the streamwise array, T.E. with Thick finlet. (b) Background-subtracted SPL spectra in the spanwise array, T.E. with Thick finlet.

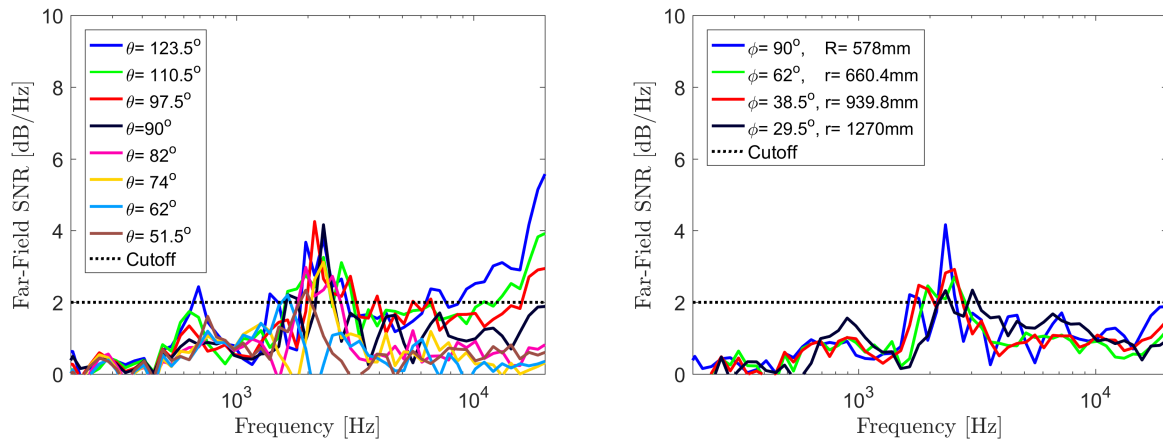


(c) Streamwise microphone array SNR, T.E. with Thick finlet. (d) Spanwise microphone array SNR, T.E. with Thick finlet.

Figure 3.12: Signal-to-Noise Ratio (SNR) and background-subtracted SPL spectra at $U_{ref} = 50$ m/s for the trailing edge (T.E.) with Thick finlets applied. Background-subtracted spectra are only shown for SNR > 2 dB. (a) SPL in the streamwise array, (b) SPL in the spanwise array, (c) SNR in the streamwise array, (d) SNR in the spanwise array.



(a) Background-subtracted SPL spectra in the streamwise array, T.E. with Dense finlet. (b) Background-subtracted SPL spectra in the spanwise array, T.E. with Dense finlet.



(c) Streamwise microphone array SNR, T.E. with Dense finlet. (d) Spanwise microphone array SNR, T.E. with Dense finlet.

Figure 3.13: Signal-to-Noise Ratio (SNR) and background-subtracted SPL spectra at $U_{ref} = 50$ m/s for the trailing edge (T.E.) with Dense finlets applied. Background-subtracted spectra are only shown for SNR > 2 dB. (a) SPL in the streamwise array, (b) SPL in the spanwise array, (c) SNR in the streamwise array, (d) SNR in the spanwise array.

coordinate, \tilde{y} , such that $\tilde{y} = 0$ is at $y = 12.7$ mm, the trailing edge surface. The x - and z -coordinates are unchanged (see figure 2.15).

3.2.1 Flow Near the Untreated Trailing Edge

The effect of the transition ramp-trailing edge piece on the mean velocity profiles is shown in figures 3.14a-3.14b, where profiles measured just downstream of the untreated mock trailing edge are compared with those measured on the smooth wall with the trailing edge removed. Results for three different experimental runs are included: a smooth wall case, measured at $x = 1398$ mm, $y = 3$ mm, $z = 0$, an untreated trailing edge case measured at $x = 1398$ mm, $y = 0.5$ mm, $z = 0$, and one untreated trailing edge case measured at $x = 1400$ mm, $y = 12.63$ mm, $z = 0$. The mean velocities are shown normalized on the measured jet velocity, U_j , to account for small variations in the jet speed, and will be presented in this manner throughout the chapter. To interpret figures 3.14a-3.14b accurately, one should note that the presence of the untreated trailing edge effectively shifts the boundary layer up to $y = 12.7$ mm, the trailing edge height (shown with a dashed line in figure 3.14a). For this reason, the best way to compare the velocity profiles is by comparing the maximum velocity, U_m , ignoring for now the vertical axis. Examining figure 3.14a, the smooth wall profile has a maximum $U_m/U_j \approx 38\%$ and $\delta = 14.9$ mm (note that for a wall jet, δ is the location where $U = U_m$). For the untreated trailing edge cases, the average normalized velocity maximum between the two runs was $U_m/U_j \approx 40\%$, occurring at $\delta = 14.1$ mm. The increase in the normalized velocity maximum with the addition of the untreated trailing edge is about 2 percentage points, likely due to the curvature in the ramp (as discussed in section 2.2). The untreated trailing edge profiles, measured with different probes, agree well. Note the area of almost zero flow below the trailing edge surface, motivating the use of the adjusted coordinate, \tilde{y} . In the ensuing section, treated cases will be compared to the untreated trailing edge, not the smooth wall, further justifying the use of \tilde{y} . Comparisons will be made using the untreated trailing edge profile shown with \mathbf{x} symbols in figure 3.14a, because of the finer resolution near the surface.

Using these profiles, the computed boundary layer parameters are shown in table 3.3 and compared to the Wygnanski estimates described in section 2.1.1. Values for the untreated trailing edge profiles were measured relative to the trailing edge surface. In the three runs discussed here, only the third case shown in figure 3.14a had the probe close enough to the surface ($y = 0.1$ mm) to adequately resolve the displacement and momentum thicknesses. From table 3.3, the measured smooth wall boundary layer thickness agrees well with the Wygnanski estimate. The untreated trailing edge has a slightly smaller boundary layer thickness, which could be attributed to flow acceleration over the transition ramp inflection point. Devenport *et al.* [6] reported an increase in U_m of $0.01U_j$ due to the presence of a 3.2 mm ramp with a similar curvature to the one used here. In figure 3.14b, the mean velocity is shown normalized on U_m and the half-height, $y_{1/2}$. This is typical in wall jet literature e.g. Launder *et al.* [3]. The Wygnanski estimate for $y_{1/2}$ was used to normalize the vertical

axis, since the the spatial resolution in the outer region was too poor to accurately measure the half-height. Doing so assumes that adding the transition ramp-trailing edge piece will not affect the outer region of the wall jet, near the half-height location. This assumption is shown to be valid when comparing the measured velocity profile and those presented in Clark [5]. The flow remains self-similar with the addition of the transition ramp-trailing edge, and the smooth wall profile agrees with the measurements presented in Clark [5].

The turbulence intensities are shown in figures 3.14c-3.14d in terms of the absolute coordinate y and in terms of the normalized coordinate $y/y_{1/2}$. This was done in order to facilitate a comparison with the turbulence intensity profiles reported by Devenport *et al.* [6] in this wind tunnel. Again, the Wygnanski estimate of $y_{1/2} = 112.5$ mm was used, for the reasons given above. As in figure 3.14a, note that the presence of the trailing edge effectively shifts the profile up by the edge height, 12.7 mm. Examining the turbulence intensities (neglecting the offset in the vertical direction), the profiles agree well within the experimental uncertainty, showing that the impact of the trailing edge on the turbulence intensity is negligible. For reference, the maximum in the outer region is about 20%, at about $0.6y_{1/2}$ away from the surface (smooth wall or trailing edge). This is consistent with the single-hot-wire results reported by Devenport *et al.* [6].

3.2.2 Treatment Effects on the Mean Flow Quantities

Examining the mean velocity and turbulence intensity profiles (measured at the centerline of a treatment channel, see figure 2.15) gives some insight into the general flow changes the treatments create. It was not necessary to treat the full span of the trailing edge to capture the relevant aerodynamics, so the treatments were placed on the center 228.6 mm, centered about $x = 0$. To begin the analysis, the full velocity and turbulence intensity profiles were plotted in figure 3.15 for all treated and untreated cases. Note that in this section, the figures will be shown as a function of the adjusted coordinate \tilde{y} , where $\tilde{y} = 0$ corresponds to the trailing edge top surface. As mentioned in the previous section, the mean velocities are normalized on U_j and the turbulence intensities are computed using U_m . Both quantities are unchanged in the outer region, meaning the flow changes are only felt near the surface. As such, the remaining figures will only be shown for $0 \leq \tilde{y} \leq 10$ mm; above this region, the flow returns to the untreated wall jet profile within the measurement uncertainty.

Table 3.3: Transition ramp effects on the boundary layer parameters, $x = 1397$ mm, $U_{ref} = 50$ m/s. Untreated trailing edge values are measured relative to the step surface.

	δ [mm]	δ^* [mm]	θ [mm]	$y_{1/2}$
Smooth Wall, Wygnanski	15.7	0.9	0.7	112.5
Smooth Wall, CTA	14.9	-	-	-
Untreated T.E., CTA	12.4	0.6	0.5	-

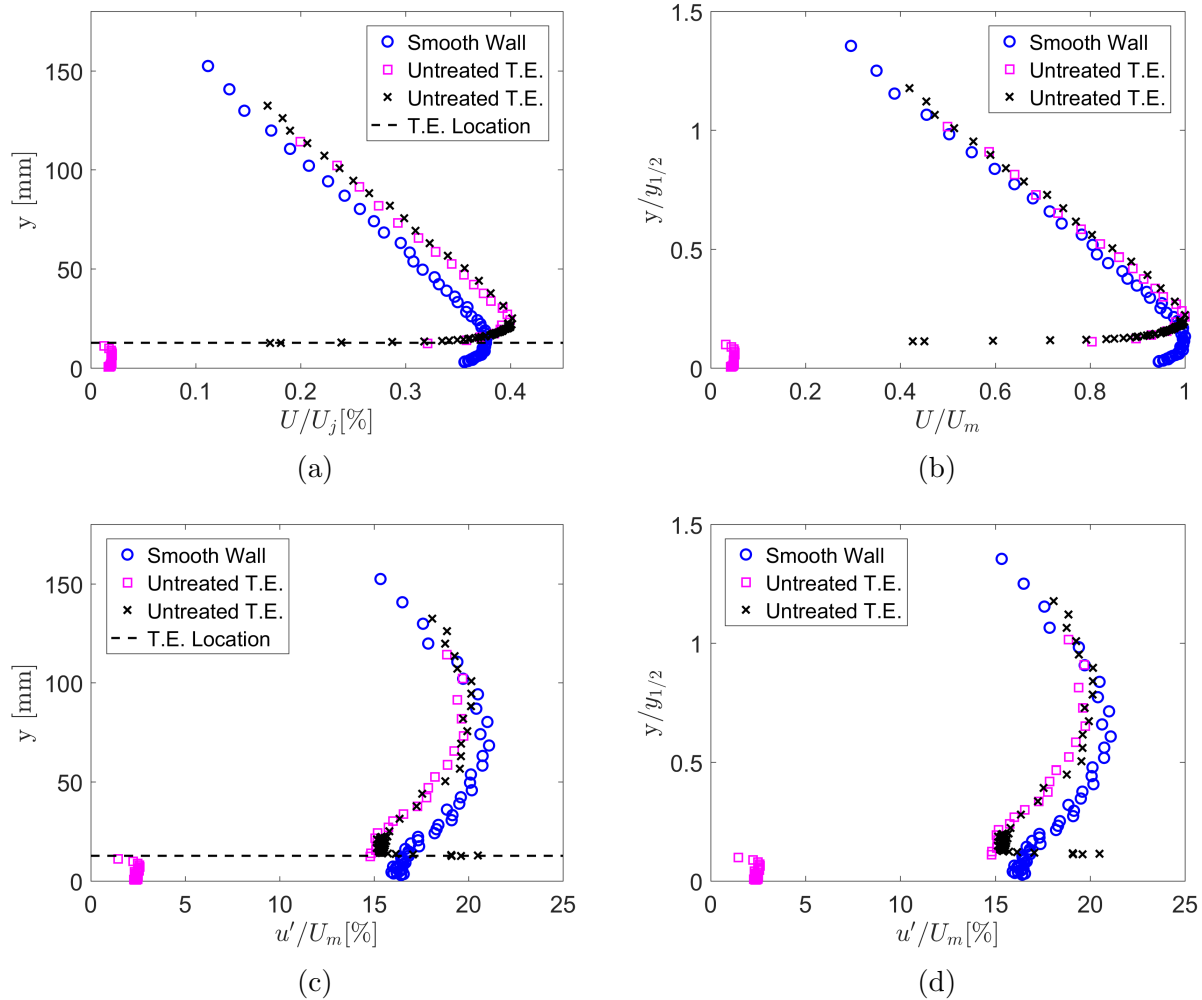


Figure 3.14: **(a)** Mean velocity profiles, normalized on the corresponding jet velocity, showing the effect of the transition ramp-mock trailing edge piece. Probe was in the $x - y$ plane at $x = 1398$ mm, $x = 1398$ mm, and $x = 1400$ mm (\circ , \square , and \times , respectively). Trailing edge location is shown with a dashed line. **(b)** Untreated trailing edge profiles normalized on U_m and $y_{1/2}$. The wall jet is self-similar, consistent with measurements in this facility presented Clark [5] and Devenport *et al.* [6] in this facility. **(c)** Turbulence intensity profiles showing the effect of the transition ramp-mock trailing edge. The root-mean-square of the fluctuations, u' , was computed by integrating the turbulence spectra up to 7 kHz, as described in section 2.5.2. **(d)** Turbulence intensities plotted versus $y/y_{1/2}$, in agreement with those presented by Devenport *et al.* [6].

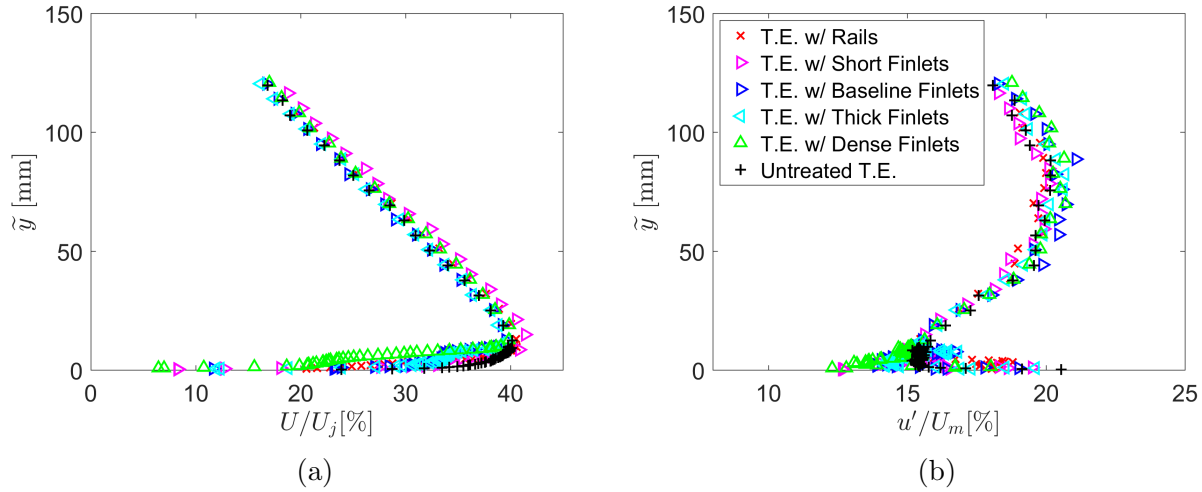


Figure 3.15: **(a)** Mean velocity profiles for the treated and untreated trailing edge cases, expressed as a percentage of U_j and plotted through the full wall jet region. **(b)** Turbulence intensity profiles for the treated and untreated trailing edge cases, plotted through the full wall jet region. Note that the turbulence intensity was found by integrating the spectra (section 3.2.3) up to 8 kHz.

Table 3.4: Mean width and standard deviation of the 95% confidence intervals on mean velocity, U/U_j , and turbulence intensity, u'/U_m shown in figures 3.16a-3.16d.

	$\bar{\delta}(U/U_j)$	$\sigma \left[\delta \left(\frac{U}{U_j} \right) \right]$	$\bar{\delta}(u'/U_m)$	$\sigma \left[\delta \left(\frac{u'}{U_m} \right) \right]$
Untreated	0.021	0.004	1.461	0.162
T.E. with Baseline Finlets	0.020	0.004	1.444	0.194
T.E. with Thick Finlets	0.020	0.004	1.444	0.185
T.E. with Short Finlets	0.019	0.005	1.466	0.190
T.E. with Dense Finlets	0.017	0.005	1.409	0.213
T.E. with Rails	0.021	0.004	1.492	0.150

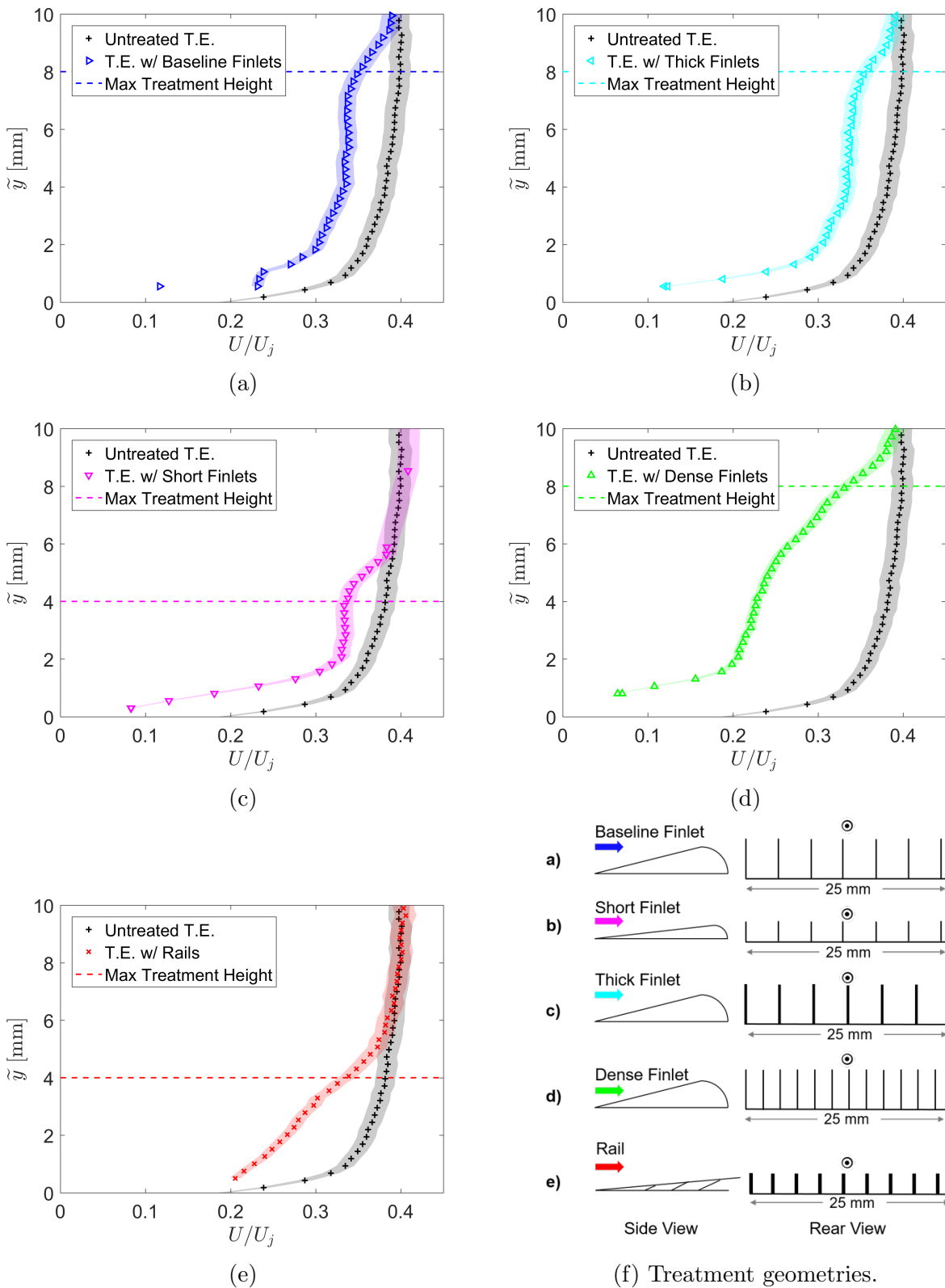


Figure 3.16: Normalized mean velocity profiles U/U_j for the treated and untreated trailing edge, measured at $x = 1400 \pm 1$ mm, $z = 0 \pm 0.25$ mm. Shaded areas represent the 95% confidence intervals. Horizontal lines indicate maximum treatment height. Legends are inset in figures a-e. (f) Relevant treatment geometries.

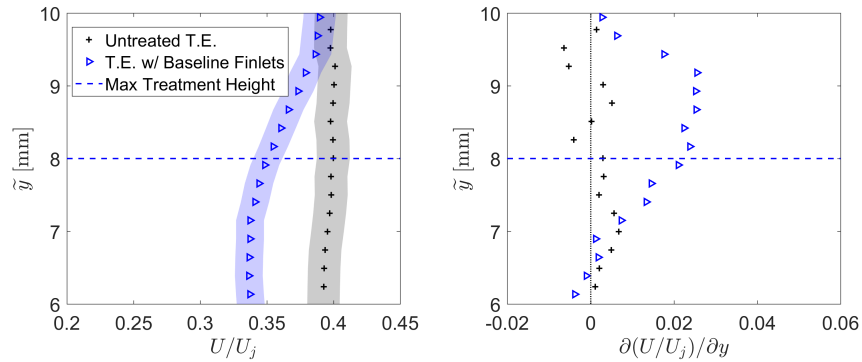


Figure 3.17: **(a)** Shear layer near the top of the Baseline treatment in figure 3.16a. Legend given in figure 3.16a. **(b)** Corresponding velocity gradient, with zero marked by the vertical line.

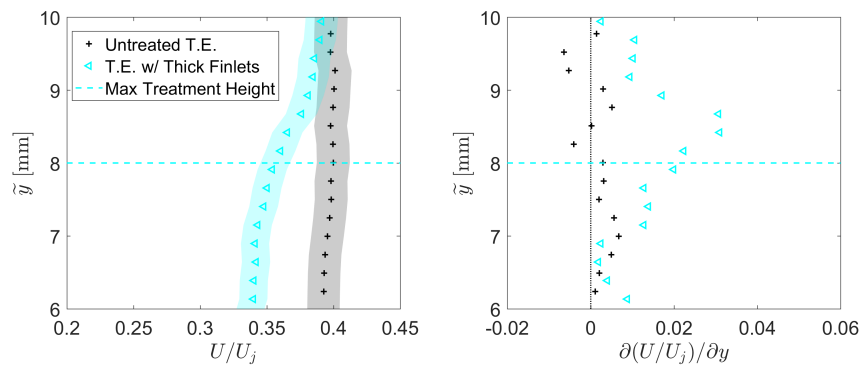


Figure 3.18: **(a)** Shear layer near the top of the Thick treatment in figure 3.16b. Legend is shown in figure 3.16b. **(b)** Corresponding velocity gradient, with zero marked by the vertical line.

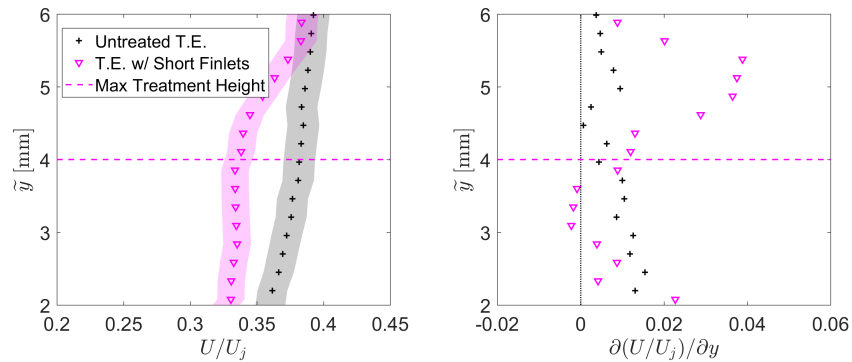


Figure 3.19: **(a)** Shear layer near the top of the Short treatment. Legend is shown in figure 3.16c. **(b)** Corresponding velocity gradient, with zero marked by the vertical line.

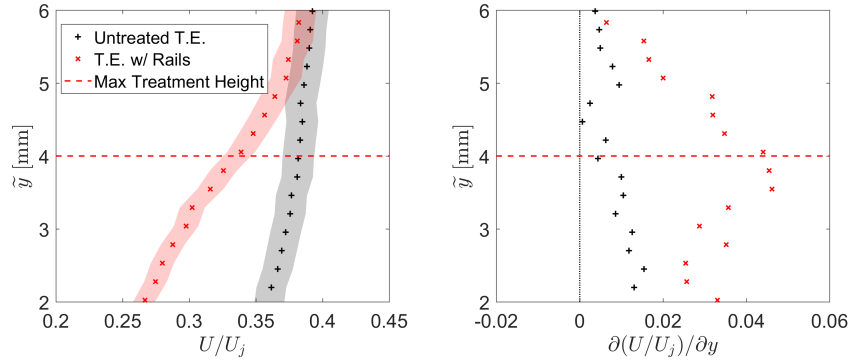


Figure 3.20: **(a)** Shear layer near the top of the Rail treatment. Legend is shown in figure 3.16e. **(b)** Corresponding velocity gradient, with zero marked by the vertical line.

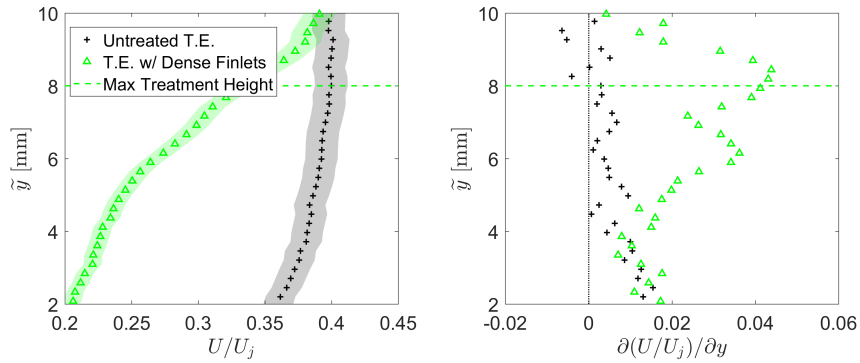


Figure 3.21: **(a)** Shear layer near the top of the Dense treatment. Legend is shown in figure 3.16d. **(b)** Corresponding velocity gradient, with zero marked by the vertical line.

Table 3.5: Boundary layer properties for the treated and untreated cases.

Treatment	L_M [mm]	L_M/h	$\frac{U}{U_j} _{\max}$	$\frac{\partial(U/U_j)}{\partial y} _{\max}$ [mm ⁻¹]	δ_ω [mm]	δ [mm]	δ^* [mm]	θ [mm]
Untreated	-	-	0.40	0.015	26.1	12.4	0.6	0.5
Baseline	2.6	0.3	0.40	0.026	15.5	12.5	1.6	1.2
Short	2.0	0.5	0.41	0.039	10.7	14.9	1.6	1.0
Thick	2.8	0.3	0.40	0.031	12.8	12.5	1.6	1.2
Dense	5.9	0.7	0.40	0.044	9.1	12.6	3.1	1.8
Rail	3.0	0.8	0.41	0.046	8.8	13.0	1.5	1.0

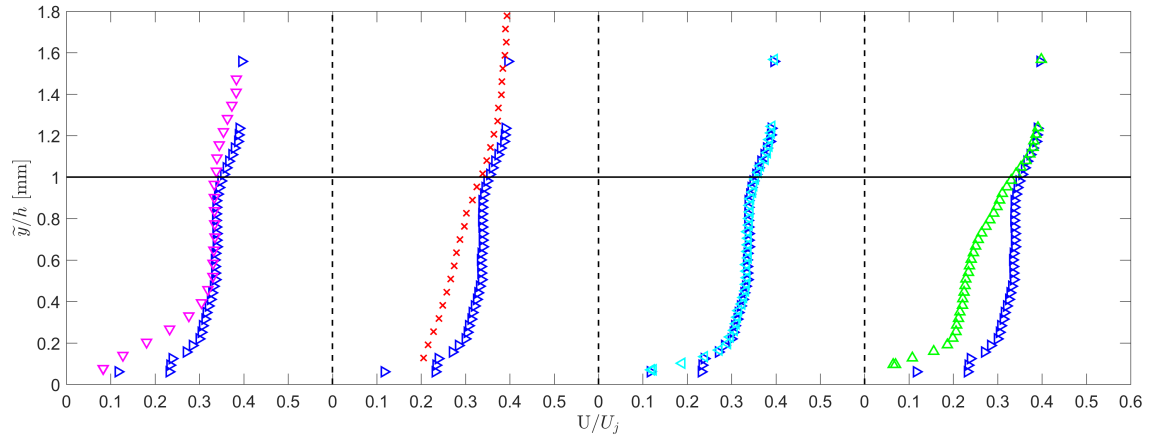


Figure 3.22: Comparison of normalized mean velocity profiles U/U_j between modified treatments and the Baseline finlet treatment applied to the trailing edge. Probe location is scaled on the treatment height, h . (a) Baseline and Short finlets, (b) Baseline and Thick finlets, (c) Baseline finlets and Rails, (d) Baseline and Dense finlets.

Figure 3.16 shows the mean velocity profiles for the untreated trailing edge and the different treatments, where figures 3.16a-3.16e correspond to the Baseline, Thick, Short, Dense, and Rail treatments, respectively, all compared to the untreated trailing edge. The profiles were measured 3 mm downstream of the trailing edge and finlet treatments. For the Rail treatment, however, the probe was located 13 mm downstream of the trailing edge due to the 10 mm extensions shown in figure 2.18b (this was still 3 mm downstream of the treatment, consistent with the finlet measurements). The dashed horizontal lines are used to indicate the individual treatment height, and the x-axis is normalized on the measured jet velocity. Lastly, the 95% confidence intervals, computed as described in section 2.7, are shown with shaded areas. For reference, the mean uncertainty interval widths and standard deviations are for $0 \leq \tilde{y} \leq 10$ mm are included in table 3.4.

The mean velocity profiles demonstrate two important features that may be contributing to the noise reduction. First, all treatments create a velocity deficit approximately up to the individual treatment height, after which the flow recovers to the same profile as the untreated case, typically after about 2 mm. The second feature is the formation of a shear layer, or mixing layer, near the top of each treatment, consistent with the canopy analogy in Clark *et al.* [7], for example. These features are also present in the hot-wire measurements presented by Afshari *et al.*, although they were not discussed in detail. The velocity deficit below the treatment heights will be considered first. Examining the treatments with a 4 mm spacing (Baseline, Thick, and Short, figures 3.16a-3.16c), they appear to have the same qualitative profile, with a relatively constant, $U/U_j \approx 0.35$ region below the finlet height. The reason for this constant-velocity region is unclear; however, one possibility is that the boundary layers growing on adjacent finlets have merged, creating a local velocity maximum until the mixing layer effects are felt. The Dense finlet (2 mm spacing, figure 3.16d) creates a much

larger velocity deficit, and has a smoother profile than the 4 mm-spaced finlets. The lack of a well-defined, constant-velocity region below the maximum treatment height may be due to the presence of the significantly thicker mixing layer. The Rail treatment (2.5 mm spacing, figure 3.16e) produces a profile similar to the Dense finlets, suggesting that the magnitude of the deficit is dependent on the treatment spacing. No constant-velocity region would be expected for the Rail velocity profile, as the Rail protrusions do not have a hard wall on which to grow a boundary layer (see figure 2.18b). The magnitude of the induced velocity deficit can be quantified using the displacement and momentum thicknesses, shown as δ^* and θ in table 3.5. All treated profiles lead to a significant increase in both δ^* and θ , by almost a factor of two. The Dense finlet, which qualitatively seems to create the largest velocity deficit, produces the largest treated δ^* and θ values. Lastly, it should be noted that the Dense finlet treatment (2 mm spacing) was also responsible for the most far-field noise attenuation, suggesting the magnitude of the velocity deficit may have an important role in trailing edge noise reduction. Due to experimental time constraints, no acoustic measurements were made with the Rail treatment, although its acoustic performance in a larger facility has been documented by Clark *et al.* [1].

Focusing now on the mixing layer, the area near the top of the treatments is shown more clearly in figures 3.17a-3.21a. Note that due to the differing treatment heights, the vertical limits are slightly different between figures 3.17 -3.21. The figures are shown in terms of \tilde{y} rather than in normalized coordinates \tilde{y}/h in order to include the untreated profile. The corresponding velocity gradients are shown in figures 3.17b-3.21b. In each finlet case, there is a clear region of high shear, with a marked increase in the gradient at the start of the mixing layer, and a marked decrease at the end of it. The velocity gradients were used in this manner to estimate the mixing layer thickness, defined here as L_M , for each finlet treatment. Specifically, the start of the mixing layer is defined as the point at which the change in the gradient is greater than 0.006 mm^{-1} . The end of the mixing layer (the upper limit) is defined as the point at which the gradient returns to the untreated trailing edge values. The absolute and normalized shear layer thicknesses (L_M and L_M/h , respectively) are included in table 3.5, as well as the maximum gradient. The shear layer thickness can also be quantified in terms of the vorticity thickness, δ_ω , a common metric in mixing layer literature [34, 35, 36]. For the wall jet, the vorticity thickness shall be defined as:

$$\delta_\omega = \frac{(U/U_j)_{max}}{(\partial(U/U_j)/\partial y)_{max}} \quad (3.6)$$

In this experiment, since $(U/U_j)_{max} \approx 0.4$ is essentially constant (hot-wire measurements were only made at $U_{ref} = 50 \text{ m/s}$), the vorticity thickness is another way to quantify the mixing layer strength; a smaller vorticity thickness implies higher shear. Examining both the maximum gradient and the vorticity thickness, it becomes clear that the Rail and Dense finlet treatments, with 2.5 mm and 2 mm spacing, create the strongest mixing layers. Of the remaining treatments (all with 4 mm spacing), the Short finlets have the highest shear.

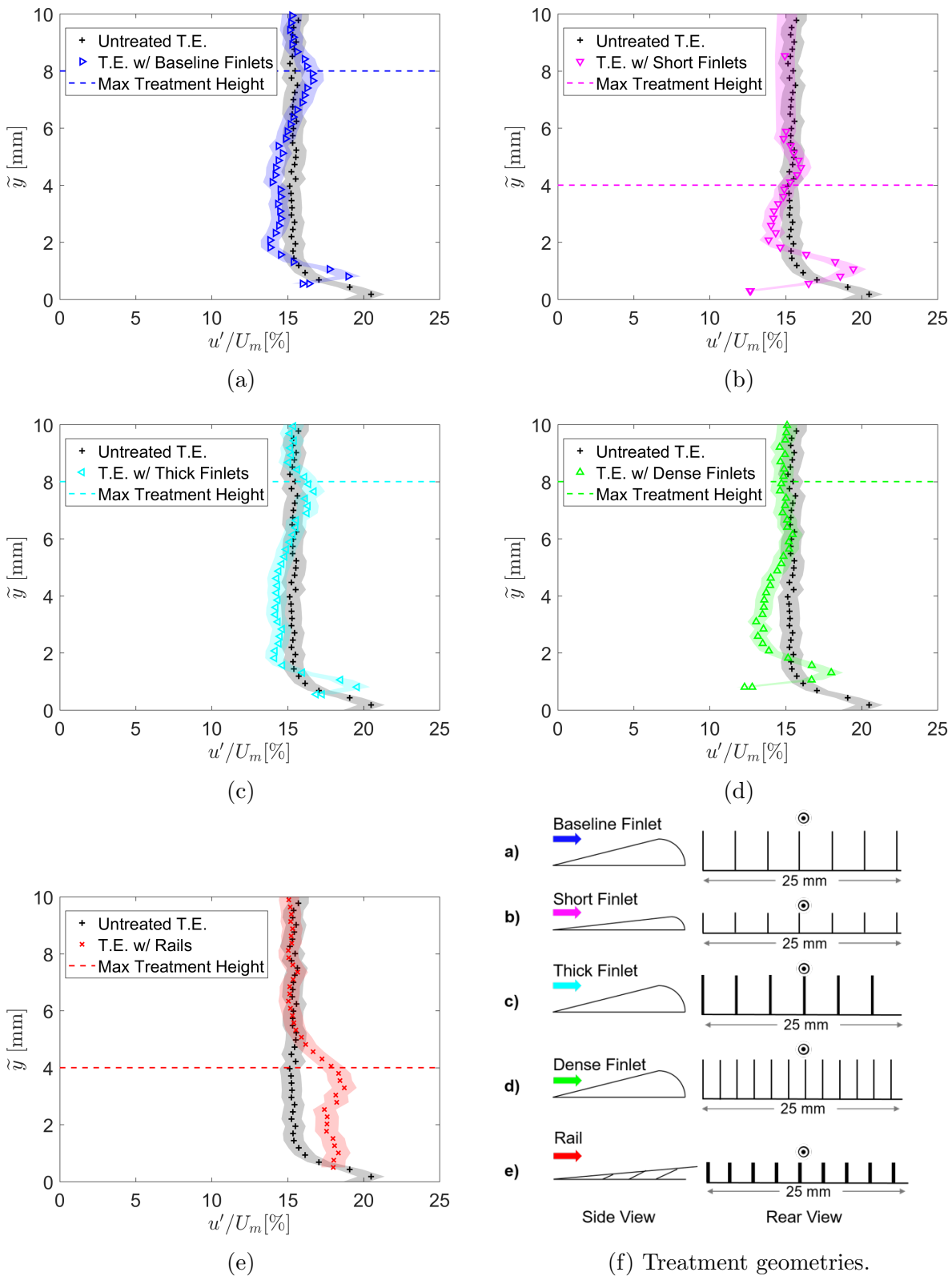


Figure 3.23: Treated and untreated trailing edge turbulence intensities, measured at $x = 1400 \pm 1$ mm, $z = 0 \pm 0.25$ mm. Shaded areas indicate the 95% confidence interval. Horizontal line indicates maximum treatment height. Legends are inset in figures a-e. (f) Relevant treatment geometries.

Interestingly, although the Baseline and Thick treatments produce almost the same velocity deficit, the Thick finlets have a much stronger gradient.

Qualitatively, the various treatments are compared to the Baseline finlet in figure 3.22, where the effect of the finlet height is also shown by normalizing the probe location on the individual treatment height, h . For example, figures 3.22a-d show the Short, Rail, Thick, and Dense treatments (4 mm, 4 mm, 8 mm, 8 mm heights) compared to the Baseline finlet (8 mm height). As alluded to previously, the finlet spacing appears to be the dominant parameter. For a given spacing, the velocity deficit throughout the treatment height is similar, as evidenced by the similar velocity profiles, δ^* , and θ . With the exception of the Short finlet profile, the mean velocities collapse well, irrespective of treatment height. One can see clearly that the treated profiles tend to return to the untreated velocity by about $\tilde{y} = 1.25h$. Plotted this way, it's also easier to see that the narrower spacing leads to a larger velocity deficit (3.22b,d). Figure 3.22c shows that thickening the finlets had a negligible effect on the velocity.

As mentioned previously, each treatment has achieved noise attenuation from 2-7 dB. In the previous discussion, it was shown that each treatment induces a shear layer near the maximum treatment height, whose strength seems dependent on the treatment spacing. It is hypothesized that this induced shear layer is causing the attenuation through a mechanism known as shear sheltering [37]. It is this shear layer, varying in thickness from about $0.2 \lesssim L_M/h \lesssim 0.6$ that may be preventing large-scale eddies from penetrating down to the trailing edge. Surface pressure measurements by Clark *et al.* [2] revealed attenuation of up to 15 dB for frequencies above 2 kHz when the trailing edge was treated with the Baseline finlets. That frequency is where the far-field noise attenuation began to manifest itself, both in that experiment and in this one. Measurements by Afshari *et al.* also revealed reductions in surface pressure fluctuations of up to 8 dB when finlets were applied. These findings would be consistent with the hypothesis that the local shear layers at the top of the treatments are sheltering the trailing edge from large eddies. This is analogous to the mixing-layer hypothesis presented in Clark *et al.* [7] and in literature for boundary layers in and above forest canopies (see Raupach *et al.* [36, 38] and Finnigan *et al.* [39] for detailed reviews).

This idea is further supported by the turbulence intensity profiles shown in figures 3.23a-3.23e. As before, the 95% confidence intervals are shown with the shaded regions. As with the mean velocity profiles, there appear to be two distinct features, below the maximum treatment height and in the mixing layer. From about $0.25 \lesssim \tilde{y}/h \lesssim 0.75$, the finlet treatments appear to reduce the turbulence intensities slightly relative to the untreated case. This is approximately where the largest reductions in mean velocity were seen. It should be noted that for the 4 mm-spaced treatments (figures 3.23a-3.23b), the uncertainty intervals tend to overlap throughout this region. The reduction in turbulence intensity can be seen most clearly for the Dense finlets in figure 3.23d. There, the maximum reduction is about 3 percentage points. The pronounced increase in turbulence intensity near the surface is believed to be a combination of the 0.5 mm treatment substrate and the local mixing layer associated with the trailing edge. The Rail treatment produces a significant increase in

turbulence intensity below the maximum treatment, believed to be due to vortex shedding off of the cylindrical supports (see figure 2.18b. In the literature, e.g. Smedman *et al.* [40], a reduction in turbulence intensity (like that seen in figure 3.23) is considered an indicator of shear sheltering. With the exception of the Dense finlets, the treatments also exhibit a slight peak in the mixing layer region near the top of the treatments, which would be expected because of the increase in the streamwise shear stresses (proportional to the velocity gradients). The reason for the lack of a turbulence intensity peak near the Dense finlet mixing layer is unclear. It is worth emphasizing that the Dense finlets had the best acoustic performance.

3.2.3 Turbulence Spectra

The power spectral densities of the velocity fluctuations were computed for each measurement run as described in section 2.5.2. The spectral data are presented first as contour maps in figure 3.24. Before analyzing the results in detail, a description of the way the data is presented will be helpful. Figures 3.24a-3.24d show the *change* in the logarithm of the power spectral density caused by the various treatments, as defined in equation 3.7. The vertical axes show the probe location normalized by the treatment height, \tilde{y}/h . The horizontal axes show the frequency up to 7 kHz, consistent with the cutoff frequency given in section 2.5.2. Finally, the color gradient indicates the magnitude of the change created by the treatments. A diverging color map was chosen to emphasize the increase or decrease relative to the untreated trailing edge turbulence levels. Put another way, the color scheme was chosen such that $\Delta_{\text{PSD}} = 0$ corresponds to white, a decrease in turbulence levels ($\Delta_{\text{PSD}} < 0$) is blue, and an increase in turbulence levels ($\Delta_{\text{PSD}} > 0$) is red. Figure 3.24f is included as a visual reminder of the geometric differences between treatments.

$$\Delta_{\text{PSD}} = 10 \log_{10} \left(\frac{G_{uu,\text{treated}}}{G_{uu,\text{untreated}}} \right) [\text{dB/Hz}] \quad (3.7)$$

Because the vertical probe locations varied slightly between runs, the spectral contours are

Table 3.6: Estimates of the mixing layer frequency, f_M , and starting/ending locations in terms of the maximum treatment height, h .

Treatment	f_M [Hz]	$\tilde{y}_{M,\text{lower}}/h$	$\tilde{y}_{M,\text{upper}}/h$	$\frac{\tilde{y}_M}{h} _{\text{max}}$
Baseline	1070	0.9	1.2	1.1
Short	1390	1.0	1.5	1.3
Thick	1000	0.9	1.2	1.1
Dense	470	0.5	1.3	1.1
Rail	930	0.7	1.5	0.9

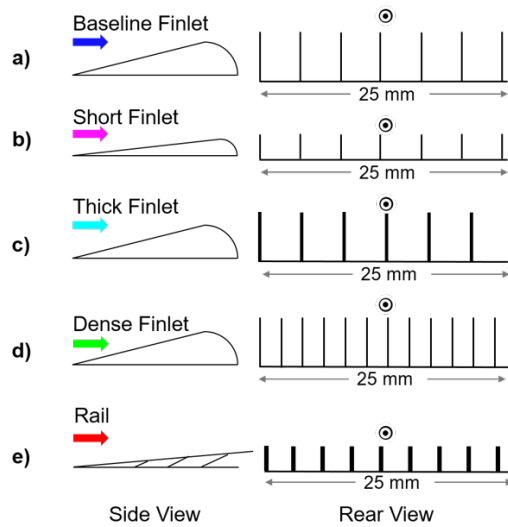
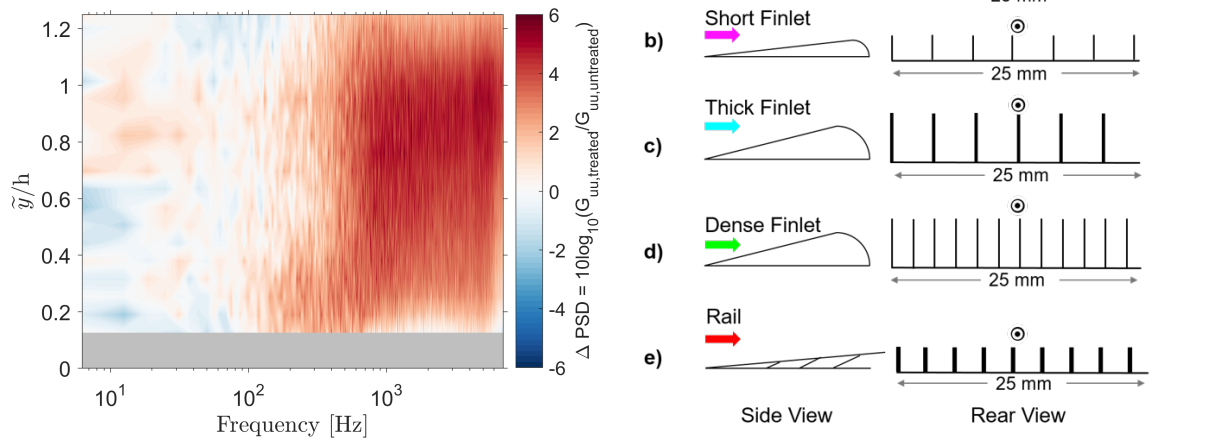
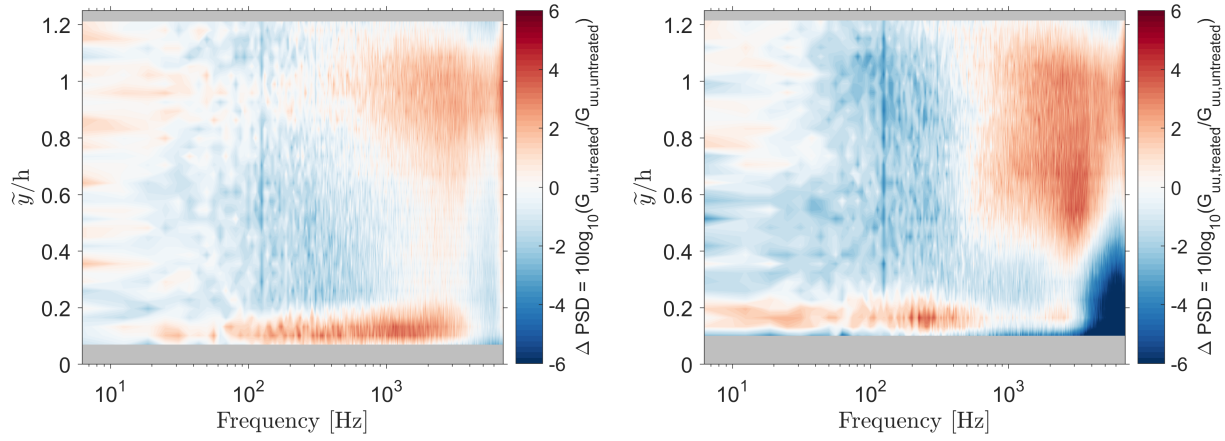
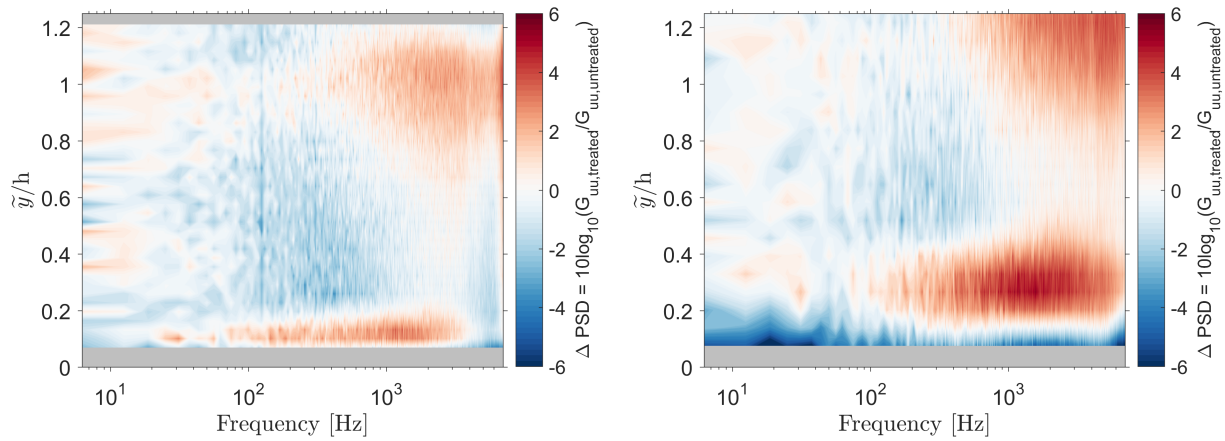


Figure 3.24: Change in power spectral densities (units of dB/Hz) with the treatments applied. Vertical axis is the normalized probe location using the maximum treatment height, h . Horizontal axis is the frequency, up to 7 kHz. Color indicates magnitude of the change. Grayed areas contain no data.

presented only where corresponding gridpoints were within 0.2 mm of each other i.e. for regions where $|\tilde{y}_{\text{treated}} - \tilde{y}_{\text{untreated}}| < 0.2$ mm. Grayed regions in figures 3.24a-3.24e did not meet this criterion and do not contain any data. For ease of comparison throughout the treatments, the contours are presented between $0 \leq \tilde{y}/h \leq 1.25$. However, with the data shown in this manner, care is needed when analyzing the vertical axis, as h varies for different treatments. The reader is referred to the inset in figure 3.24f to visualize the corresponding treatment dimensions. Lastly, the uncertainty in Δ_{PSD} is estimated conservatively to be 1 dB.

With this in mind, the spectral contours yield some important insights into the aerodynamics near the treatments, particularly in light of the preceding mean velocity and turbulence intensity analysis. As with the mean quantities, generally there are two distinct regions, above and below the maximum treatment height, $\tilde{y}h = 1$. Beginning first with the Baseline finlets in figure 3.24a (8 mm height, 4 mm spacing, 0.5 mm thickness), there is a noticeable decrease in turbulence levels between $80 \lesssim f \lesssim 1000$ Hz below the maximum treatment height. This supports the earlier claim that the finlets tend to reduce the turbulence intensity (see figure 3.23). Each finlet treatment, figures 3.24a-3.24d, achieves reductions in this frequency range, although the magnitude of the reduction is dependent on the finlet geometry. The Dense finlets produce a significant decrease in turbulence levels throughout the treatment height for a clearly defined frequency range of 60-370 Hz. Below about 80 Hz, the remaining finlet treatments tend to increase the turbulence levels. In each finlet case, there is also a marked, broadband increase in turbulence levels near the wall, consistent with the local peaks in turbulence intensity seen in figure 3.23, attributed to the 0.5 mm treatment substrate and the local mixing layer associated with the trailing edge. This near-wall shear region is strongest in the Short finlet contour (4 mm height, 4 mm spacing, 0.5 mm thickness, figure 3.24b). Because of the shorter treatment height, and the fact that the probe locations are normalized on h , at first glance it appears that the near-wall region of high turbulence is thicker for the Short finlet compared to the Baseline finlet. However, in terms of millimeters (e.g. $\frac{\tilde{y}}{h} * h$, this region extends to about 1.6 mm above the trailing edge surface. What figure 3.24b shows is that the near-wall turbulent region makes up a larger portion of the Short finlet profile, as expected due to the smaller treatment height. The spectral contour for the Rail treatment (figure 3.24e) is significantly different than the finlet contours. No clear region of turbulence reduction is present; indeed, a strong increase in turbulence levels is seen above about 100 Hz. This overall increase in turbulence levels is consistent with the turbulence intensity profile in figure 3.23e, and is attributed to vortex shedding off the support struts and the 10 mm extensions downstream of the trailing edge.

The key feature in the spectral contours is the mixing layer that occurs near $\tilde{y}/h=1$, believed to be responsible for the shear sheltering phenomenon. With the Baseline finlets (8 mm height, 4 mm spacing, 0.5 mm thickness), the thickness of the induced mixing layer was estimated to be about 1.8 mm, or $0.2h$ (table 3.5). The high-turbulence feature in the upper-right corner of figure 3.24a above about 600 Hz, has a vertical size of about $0.8 \lesssim \tilde{y}/h \lesssim 1.1$, which is roughly the expected mixing layer thickness. The highest turbulence levels in this

region occur at approximately the location of the maximum velocity gradient, as evidenced by the mean velocity gradients in figures 3.17-3.20 and the turbulence intensity peaks near the treatment maxima in figures 3.23a-3.23e. Lastly, this high-turbulence region begins to manifest itself near a frequency consistent with turbulent eddies of the same size as the mixing layer thickness. This frequency can be estimated as follows. We start with the assumption that the largest eddy that can fit in the mixing layer has a size L_M , and a convection velocity, U_c , equal to the mean velocity in the mixing layer. In this experiment, $U_c \approx 0.35U_j$ for each treatment. The associated frequency can then be estimated as in equation 3.8. This frequency can be considered the lowest frequency associated with the mixing layer. An implicit assumption in this estimate is that the largest-sized eddy will have the lowest convection velocity.

$$f_{U_c} \approx U_c / 2\pi L_M \quad (3.8)$$

For the Baseline treatment, the nominal frequency using table 3.5 would be about 1500 Hz. Considering the uncertainty in the estimate of L_M and Δ_{PSD} , this aligns well with the formation of the high-turbulence region in figure 3.24a. The trends discussed for the Baseline finlets are consistent for each treatment. There is a noticeable increase in turbulence levels throughout probe locations associated with the mixing layer, starting roughly at a frequency f_{U_c} predicted by equation 3.8. For reference, f_{U_c} as well as the estimated lower and upper limits of the mixing layer location, $\tilde{y}_{M,\text{lower}}$, $\tilde{y}_{M,\text{upper}}$ are included in table 3.6.

Within the frequencies shown here, there remains one feature unique to the finlet treatments that has not been discussed. For the Baseline, Thick, and Dense finlets (figures 3.24a, 3.24c, 3.24d, geometry shown in figure 3.24f), there is a noticeable reduction in turbulence intensities below the mixing layer region (e.g. below $\tilde{y}/h \approx 0.5$) at frequencies above about 4500 Hz. For the Dense finlets (8 mm height, 2 mm spacing, 0.5 mm thickness, figure 3.24d), this region is slightly wider, beginning at about 3200 Hz. Additionally, the turbulence levels are significantly reduced, by up to 8 dB relative to the untreated trailing edge. The transition between the high-turbulence mixing layer region and the region of reduced turbulence is most pronounced for the Dense finlets, and may be evidence of frequency-dependent shear sheltering. It should be noted that this region of reduced turbulence was not seen with the Short finlets (4 mm height, 4 mm spacing, 0.5 mm thickness, figure 3.24b), possibly because of the interaction between the near-wall shear region and the mixing-layer near the maximum treatment height. The high-frequency region of turbulence reduction is also absent from the Rail spectral contour (4 mm height, 2.5 mm spacing, 1.25 mm thickness), possibly because of turbulence due to vortex shedding off the cylindrical supports breaking apart upstream of the probe.

A Note on Shear Sheltering in the Context of Finlets

Keeping in mind that the goal of the present work is to identify the local aerodynamic effects of the finlets and relate those aerodynamics to the trailing edge noise reductions, it is helpful to briefly revisit the far-field noise results presented in figure 3.10. Far-field noise measurements were made with the Baseline, Thick, and Dense finlets, all of which had an 8 mm maximum treatment height. Each finlet design created noise reductions starting near 1000 Hz. It was hypothesized that these noise reductions may be due to shear sheltering. Examining the mean velocity and turbulence intensity profiles showed the existence of a mixing layer near the top of each treatment. Spectral contours of the turbulent fluctuations also support the existence of a mixing layer. Estimating the lowest frequency associated with the onset of the mixing layer, e.g. the frequency where the high-turbulence region near $\tilde{y}/h \approx 1$, reveals that this frequency is fairly close to the frequency associated with noise attenuation. This would suggest that shear sheltering is playing a significant role in the noise reduction. Up to $\tilde{y}/h \approx 0.5$ (below the mixing layer), there is a reduction in turbulent energy at frequencies associated with the noise reduction. Specifically, the Dense finlets, which eliminated the second noise peak centered at about 5.5 kHz at $U_{ref} = 50$ m/s (see figure 3.10b), have a reduction in turbulent energy of over 6 dB at 5.5 kHz. This may be due to the mixing layer sheltering the trailing edge from some of the turbulent eddies associated with these frequencies.

3.2.4 Streamwise Development

The last portion of the hot-wire measurements involved documenting the streamwise development of the flow along the finlets. This was done by additively manufacturing the leading 50% of the Baseline finlet treatment and applying it directly to the trailing edge, as shown in figure 2.19. This was a way to simulate traversing the hot-wire probe along a finlet channel, assuming that the effects of the rounded trailing edge portion of the finlets are not communicated upstream, and that the performance is not sensitive to the location of the finlet leading edge. The mean velocity and turbulence intensity profiles for the “mid-plane” treatment are shown in figures 3.25a-3.25b. For reference, the profiles for the untreated trailing edge and trailing edge with Baseline finlets are also included, as well as a qualitative comparison between the Baseline treatment and the “mid-plane” piece in the thumbnail image (figure 3.25c). The mid-plane treatment appears to have the same effect as the Short finlets on the mean velocity and turbulence intensity; that is, there is still a significant mean velocity deficit, and a peak in turbulence intensity near the top of the mid-plane treatment associated with the presence of a mixing layer. Interestingly, the region where turbulence intensity is reduced is significantly smaller for the mid-plane treatment compared to the Baseline treatment. The same mean velocity and turbulence intensities are shown plotted on the normalized coordinate, \tilde{y}/h in figure 3.26, where h is the maximum treatment height, consistent with the definition used throughout this chapter. Recall that for the Baseline

finlets, $h = 8$ mm; at the mid-plane of the Baseline finlets, $h = 4.36$ mm. When plotted in this manner, the profiles collapse well, suggesting that the maximum height of the applied treatment is an appropriate lengthscale, regardless of station along the treatment. One can also see that the peak turbulence intensity occurs at $\tilde{y}/h \approx 1$. The mixing layer region is seen more clearly in terms of \tilde{y} in figure 3.27. Specifically, figure 3.27b shows that the local velocity gradient in the mixing layer region is similar for both the full Baseline finlets and the Baseline finlet mid-plane. Lastly, the local boundary layer properties are tabulated in table 3.7 for the mid-plane, Baseline, and Short finlets. The displacement thickness for the Baseline finlet at mid-plane and the Short finlet is very similar. The change in power spectral density of the velocity fluctuations is shown in figure 3.28. There are clear signs of a mixing layer, as described in section 3.2.3, and the change is very similar to that caused by the short finlets (see figure 3.24b). The conclusion here is that the flow along a fixed finlet treatment, e.g. the Baseline finlet, acts like a shorter finlet with a height equal to the treatment height in the plane of interest. However, there may be increased far-field noise due to scattering off the treatments if the leading edge angle, Λ , is too steep.

3.3 Surface Pressure Fluctuations

The variation in surface pressure fluctuations with both microphone location and jet velocity is shown in matrix form in figures 3.29-3.33. Each row represents a different jet velocity, $U_{\text{ref}} = 40, 50, 60$ m/s. Within each row, the surface pressure spectra have been broken up into three different frequency ranges: 100-1,000 Hz, 1,000-10,000 Hz, and 10,000-20,000 Hz. One can imagine combining the subfigures along a row to create one “full” spectrum from 100-20,000 Hz. The different microphone positions are denoted with different symbols (figures 3.29-3.31 show the stream-aligned microphone positions, figures 3.32-3.33 show the spanwise microphone positions). Note that the microphone positions are shown in figure 2.5b. It should also be noted that four repetitions were made with a microphone at position 4, and five repetitions were made with a microphone at position five. For each configuration, e.g. untreated trailing edge, trailing edge with Baseline finlets, or trailing edge with Thick finlet, the magnitude of the pressure fluctuations tends to increase with increasing jet speed, while

Table 3.7: Comparison of boundary layer properties for the trailing edge treated with Baseline finlets, Baseline finlets at mid-plane, and Short finlets.

Treatment	L_M [mm]	L_M/h	$\frac{U}{U_j} _{\max}$	$\frac{\partial(U/U_j)}{\partial y} _{\max}$ [mm ⁻¹]	δ_ω [mm]	δ [mm]	δ^* [mm]	θ [mm]
Baseline	2.6	0.3	0.40	0.026	15.5	12.5	1.6	1.2
Baseline at Mid-Plane	2.8	0.6	0.39	0.032	12.0	14.9	1.5	1.0
Short	2.0	0.5	0.41	0.039	10.7	14.9	1.6	1.0

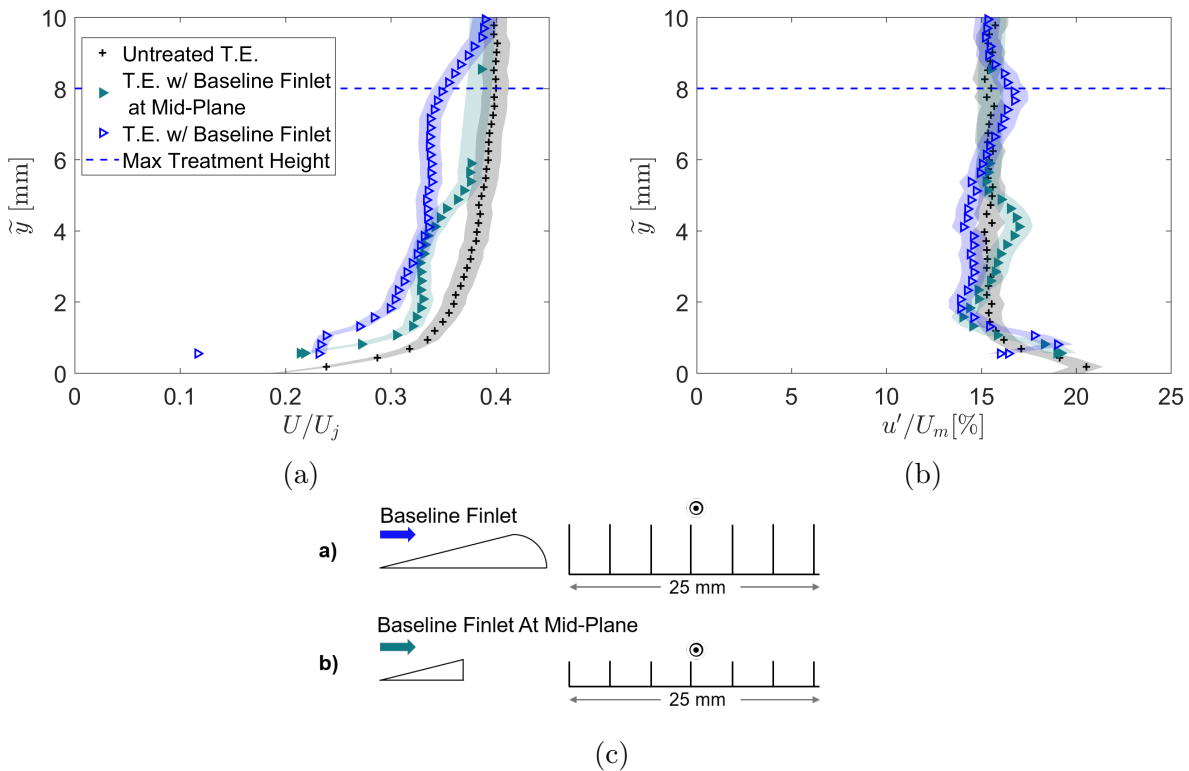


Figure 3.25: Streamwise flow development along the Baseline finlets, comparing data measured at the “mid-plane” of the Baseline treatment with results for the untreated trailing edge and trailing edge with the full Baseline finlets applied. Influence is shown for **(a)** mean velocity, normalized on U_j , and **(b)** turbulence intensity, found by integrating the turbulent spectra up to 7000 Hz, for reasons given in section 2.5.2. **(c)** Corresponding treatment geometry

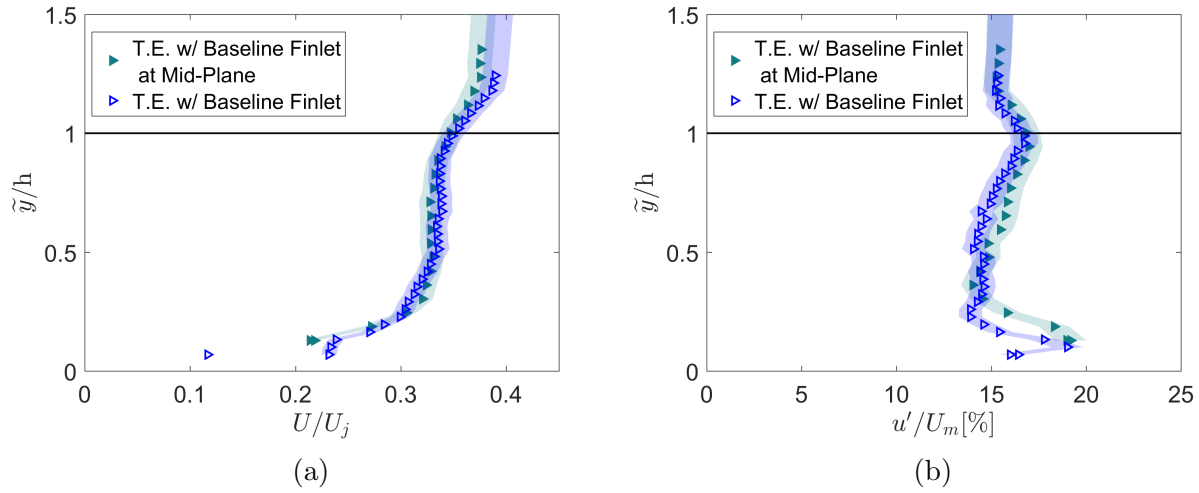


Figure 3.26: Comparison of mean velocity, **(a)**, and turbulence intensity, **(b)**, as a function of normalized probe location, \tilde{y}/h , where h is the maximum height of the applied treatment.

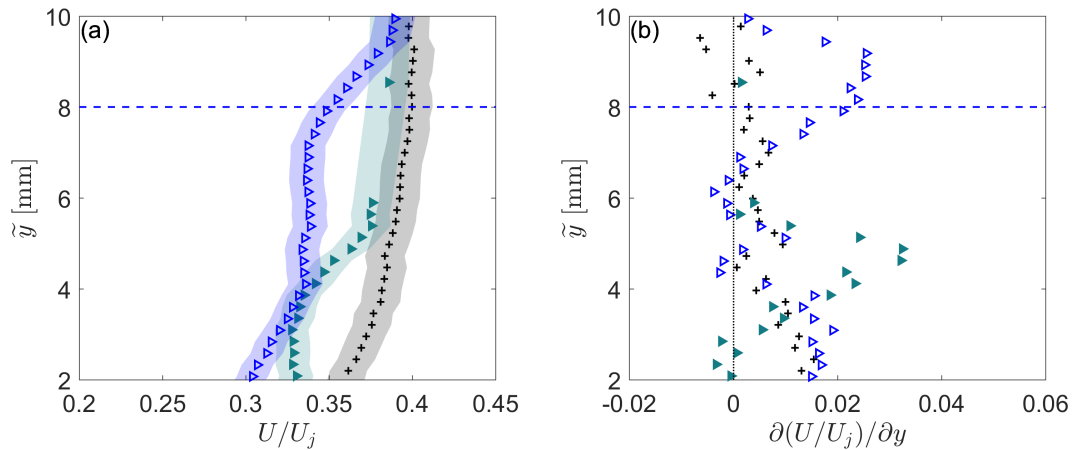


Figure 3.27: **(a)** Shear layer near the top of the Baseline and Baseline mid-plane treatments (see figure 3.25c), **(b)** Corresponding velocity gradient, with zero marked by vertical dotted line. Legend given in figure 3.25.

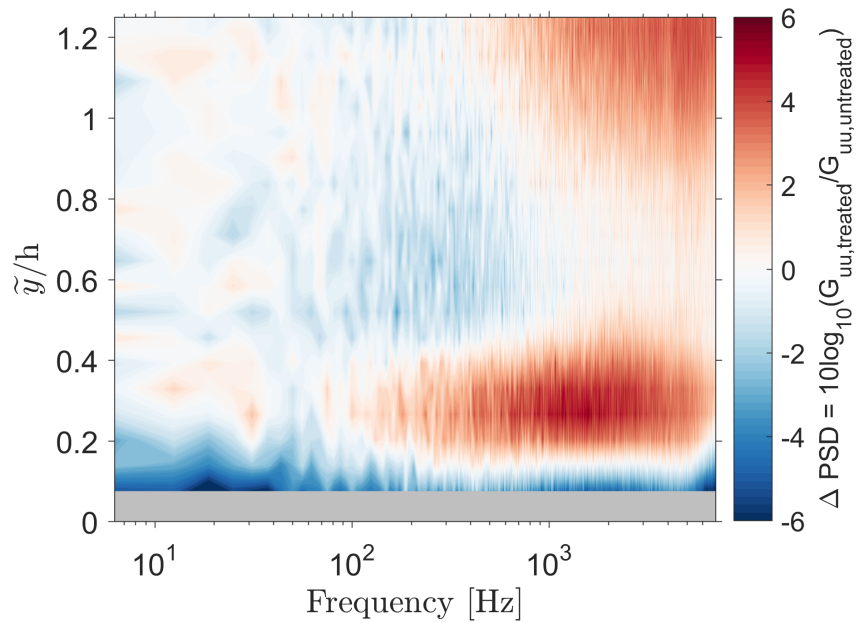


Figure 3.28: Change in power spectral density (units of dB/Hz) with the mid-plane Baseline finlet treatment applied. Vertical axis is normalized on maximum treatment height, h . Horizontal axis is the frequency up to 7 kHz. Color indicates magnitude of the change. Grayed areas contain no data.

the spectral shapes are consistent. Based on this, the ensuing discussion will focus on the data measured for a jet speed of $U_{ref} = 60$ m/s. This is shown more clearly in figures 3.34-3.35, where figure 3.34 shows the streamwise variation and figure 3.35 shows the spanwise variation. First, we examine the streamwise variation at the low frequencies (figure 3.34, first row). The unsteady surface pressures for the untreated trailing edge (first row) increase as the microphones are closer to the trailing edge e.g. from position nine to position four. The microphone at position four, nearest the trailing edge, measures the highest levels when the Baseline and Thick finlets are applied as well. Beyond that, no clear pattern with streamwise microphone position when the finlets are applied. In the mid-to-high frequencies (figures 3.34, second and third columns), no clear pattern with microphone emerges, regardless of the presence of a finlet treatment. In the spanwise direction (figure 3.35), variation between positions 1, 2, 3, 6 is within one dB. Positions 4 and 5 are about 4 dB higher. This pattern is consistent across the mid- and high-frequencies (columns two and three); the reason for this is unclear. Note that, per the test plan, measurements at the spanwise microphone positions were only made for the untreated trailing edge and trailing edge with Baseline finlets (i.e. not with the Thick finlets). This is because, with thicker finlets, the finlet channels could not be aligned with the holes in the trailing edge.

The treatment effects are seen most clearly in figures 3.36-3.41. Figures 3.36 - 3.38 show the low-, mid-, and high-frequency data, respectively, for the streamwise microphone positions. Each subfigure represents a unique microphone positions. For example, figure 3.36 shows the surface pressure fluctuation sound pressure levels at $100 \leq f \leq 1000$ Hz for (streamwise) positions 9, 8, 7, and 4. Specifically, subfigures 3.36a - 3.36d represent figures 9, 8, 7, and 4, respectively. For convenience, the microphone positions relative to each other and the finlets are shown in subfigure 3.36e. Figures 3.37 - 3.41 are plotted in a similar manner.

In the low frequencies, figure 3.36 shows that, in general, the Baseline finlets increase the surface pressure levels by about 1 dB relative to the untreated trailing edge, whereas the Thick finlets cause about a 4 dB increase. The reason for the large variation at position 4 (figure 3.36d) is unclear. In the mid-frequencies (figure 3.37), the Thick finlets increased the magnitude of the surface pressure fluctuations by about 3.5 dB relative to the untreated trailing edge, compared to a 1.5 dB increase with the Baseline finlets. In the high-frequency range (figure 3.38), no significant change is seen below 14 kHz when the finlets are applied; beyond that, the finlet effects appear dependent on the position at which the measurement was made. In the spanwise direction, at low frequencies (figure 3.39), the Baseline finlets increase the unsteady surface pressures by about 1.5 dB. In the mid-frequencies (figure 3.39) adding the Baseline finlets has a much smaller effect, tending to decrease the levels by about 1 dB between 1500-3300 Hz and increase the levels by about 1 dB between about 5-10 kHz. At the high frequencies, the Baseline finlets appear to increase the levels relative to the untreated trailing edge by about 10 dB above 14 kHz. It is surprising that the surface pressure fluctuations are increased with finlets, while the far-field noise levels are significantly decreased. Based on Amiet's theory, this is rather unexpected. However, this is consistent with measurements made by Clark *et al.* [2, 25] with similar unsteady pressure

transducers between finlet channels on the pressure side of a wind turbine airfoil near the trailing edge. There, it was hypothesized based on RANS simulations that the increase in pressure fluctuation magnitude may be due to a local increase in turbulent kinetic energy.

Lastly, the coherence for various pairs of microphones is shown in figures 3.42 - 3.43. For streamwise pairs of microphones, the finlets consistently reduce the coherence relative to the untreated trailing edge. As expected, the coherence increases with decreasing separation distance. In the streamwise direction, the maximum coherence (occurring at about 100 Hz) for the untreated trailing edge increases from 0.4 at a separation of $\Delta x = 57.15$ mm to 0.55 at a separation of $\Delta x = 19.05$ mm. For the largest separation distance (positions 4-9, $\Delta x = 19.05$ mm), the coherence is reduced by about 0.09 and 0.11 with the Thick and Baseline finlets, respectively. For the smallest separation distance (positions 4-7, $\Delta x = 19.05$ mm), the Baseline finlets have a negligible effect on the peak coherence, whereas the Thick finlets reduce the peak coherence by about 0.04. In the spanwise direction (figure 3.43), the microphone pair with the smallest separation distance (positions 5-4, $\Delta z = 13.27$ mm) has a peak untreated trailing edge coherence of 0.4. Between about 100 and 170 Hz, the Baseline finlets slightly increase the coherence, by up to 0.04. Above about 170 Hz, the coherence is reduced by up to 0.09 with the Baseline finlets. This further supports the conclusions made by Clark *et al.* [2, 25] that the noise reduction with finlets is a mixture of shear sheltering e.g. moving turbulent eddies away from the edge, and reducing the spanwise correlation lengthscale, as evidenced by the reduction in coherence by spanwise pairs of microphones.

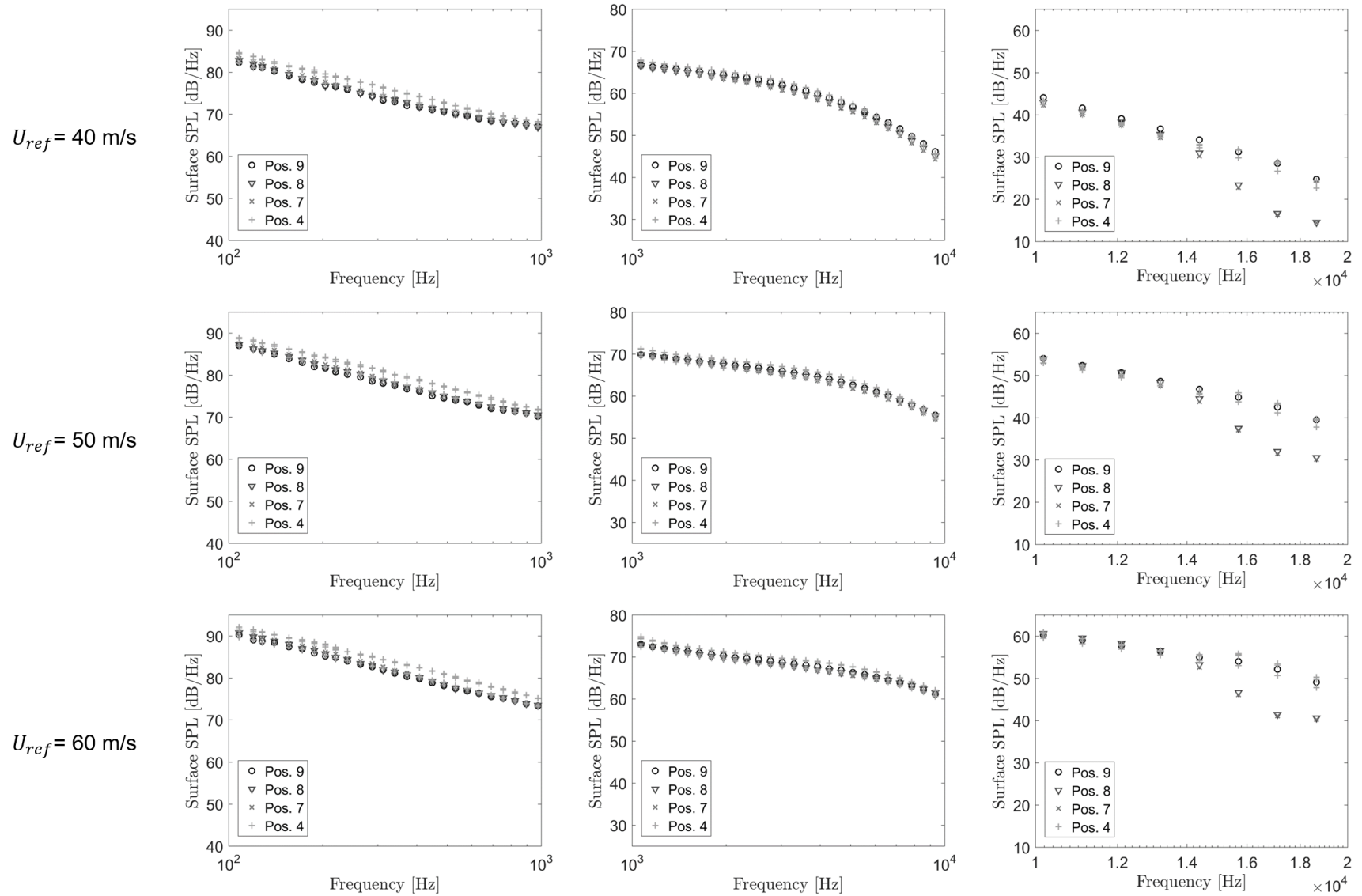


Figure 3.29: Surface pressure spectra variation in the streamwise direction for the untreated trailing edge. Each row represents a different speed ($U_{ref} = 40, 50,$ and 60 m/s). Each column represents a different frequency range (left to right, 100-1,000 Hz, 1,000-10,000 Hz, and 10,000-20,000 Hz). Within each figure, the different symbols denote different, streamwise-aligned microphone positions.

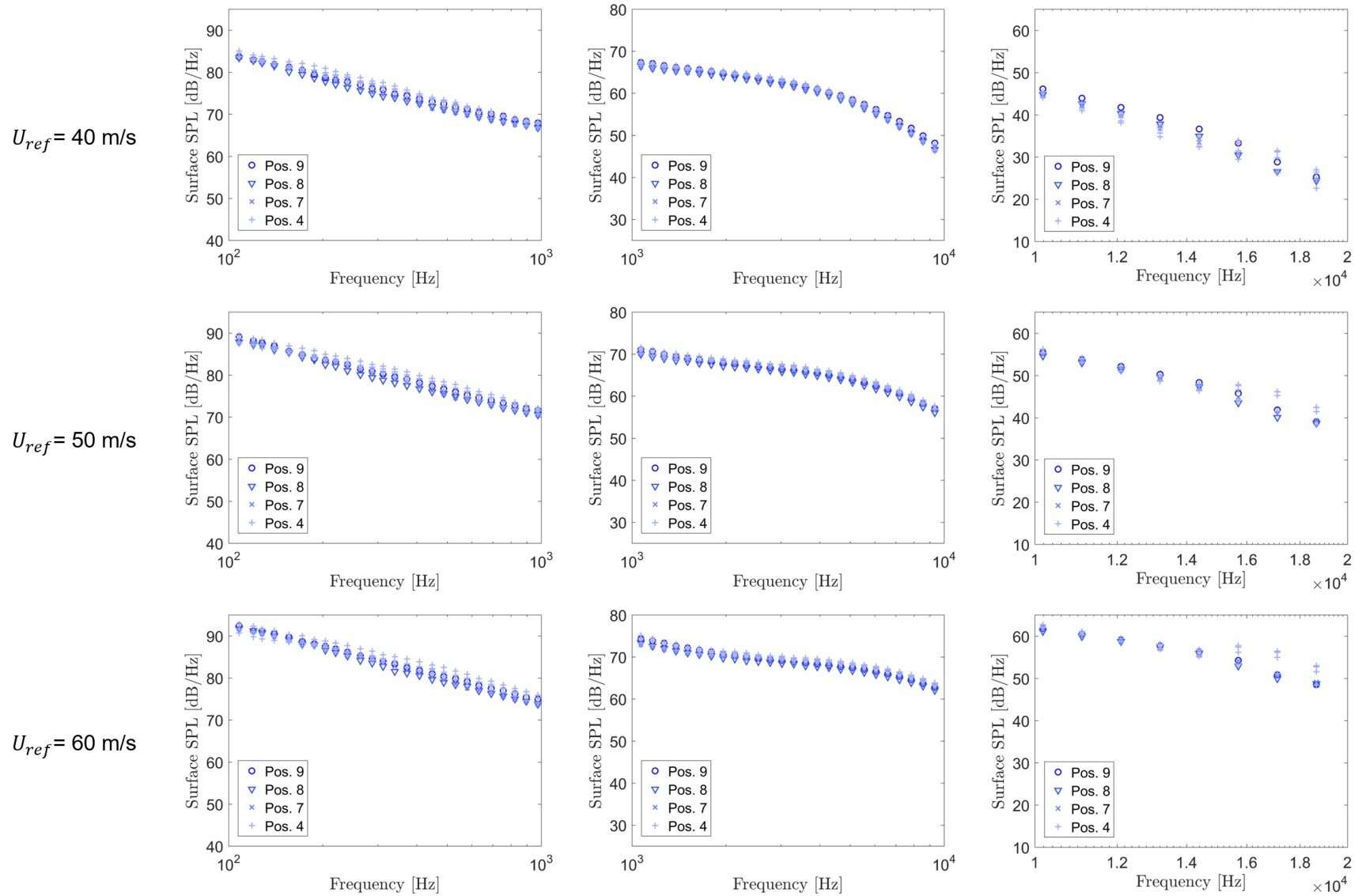


Figure 3.30: Surface pressure spectra variation in the streamwise direction for the trailing edge with Baseline finlets applied. Each row represents a different speed ($U_{ref} = 40, 50,$ and 60 m/s). Each column represents a different frequency range (left to right, 100-1,000 Hz, 1,000-10,000 Hz, and 10,000-20,000 Hz). Within each figure, the different symbols denote different, streamwise-aligned microphone positions.

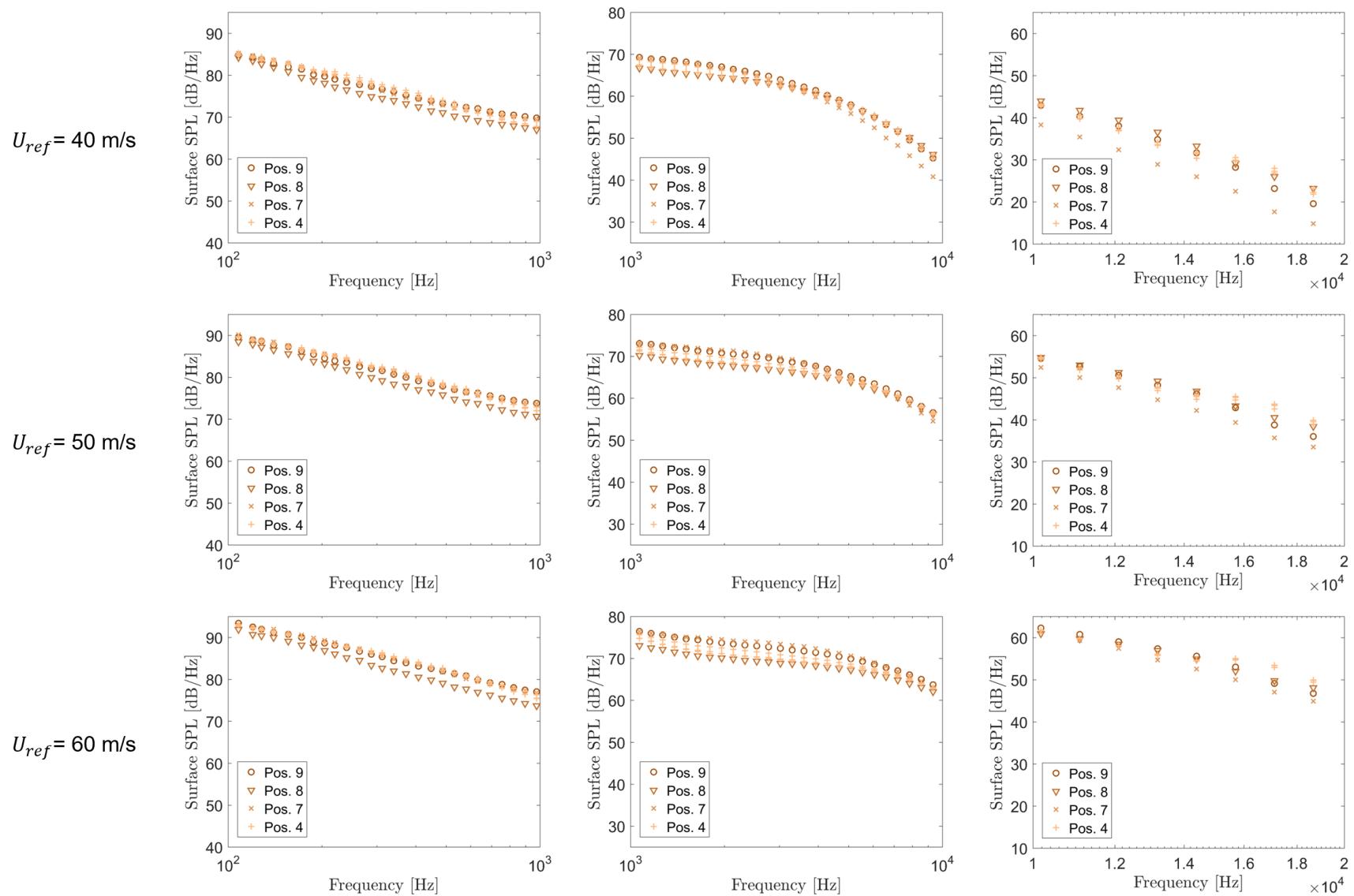


Figure 3.31: Surface pressure spectra variation in the streamwise direction for the trailing edge with Thick finlets applied. Each row represents a different speed ($U_{ref} = 40, 50,$ and 60 m/s). Each column represents a different frequency range (left to right, 100-1,000 Hz, 1,000-10,000 Hz, and 10,000-20,000 Hz). Within each figure, the different symbols denote different, streamwise-aligned microphone positions.

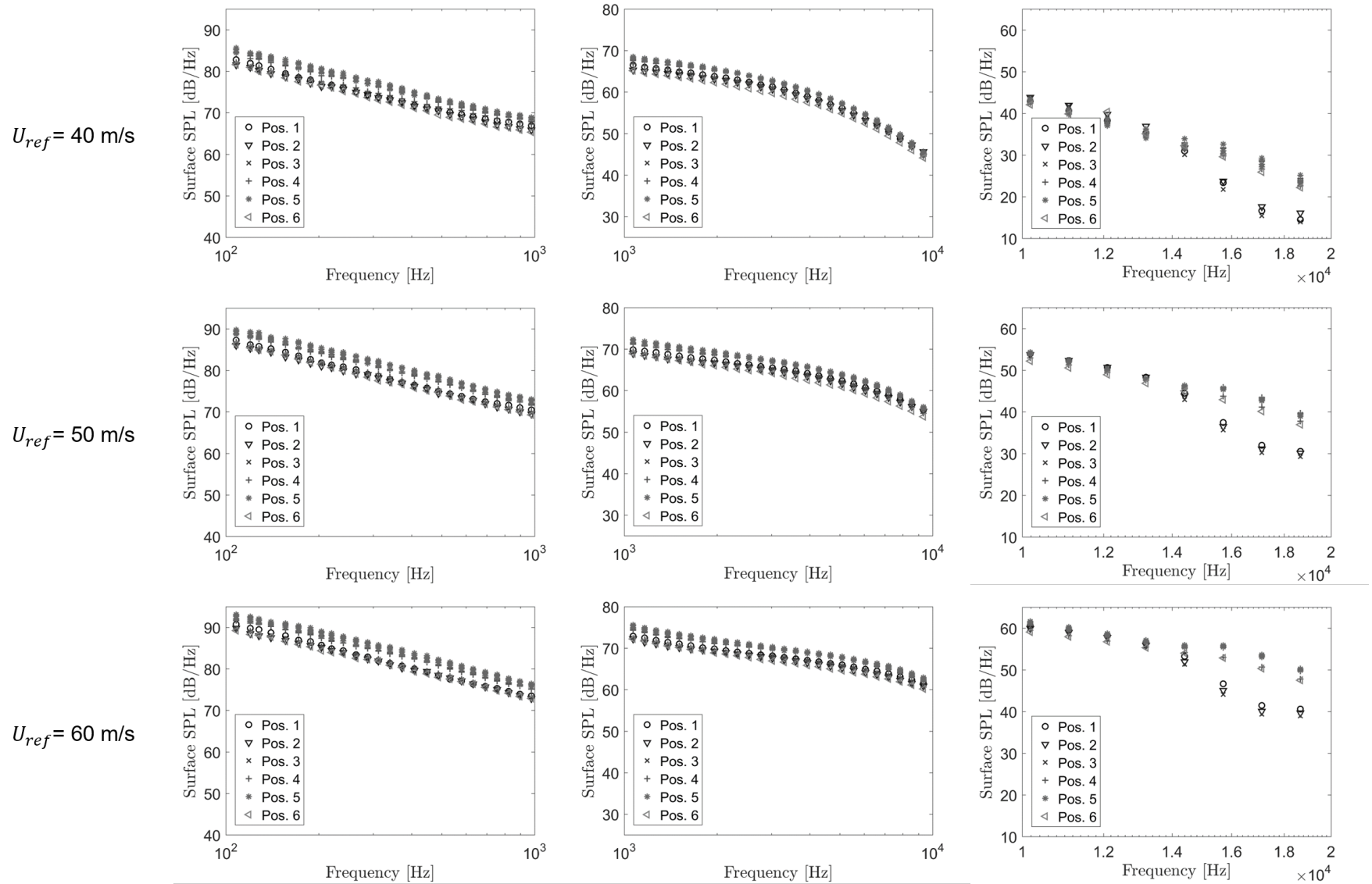


Figure 3.32: Surface pressure spectra variation in the spanwise direction for the untreated trailing edge. Each row represents a different speed ($U_{ref} = 40, 50,$ and 60 m/s). Each column represents a different frequency range (left to right, 100 - $1,000$ Hz, $1,000$ - $10,000$ Hz, and $10,000$ - $20,000$ Hz). Within each figure, the different symbols denote different, spanwise-aligned microphone positions.

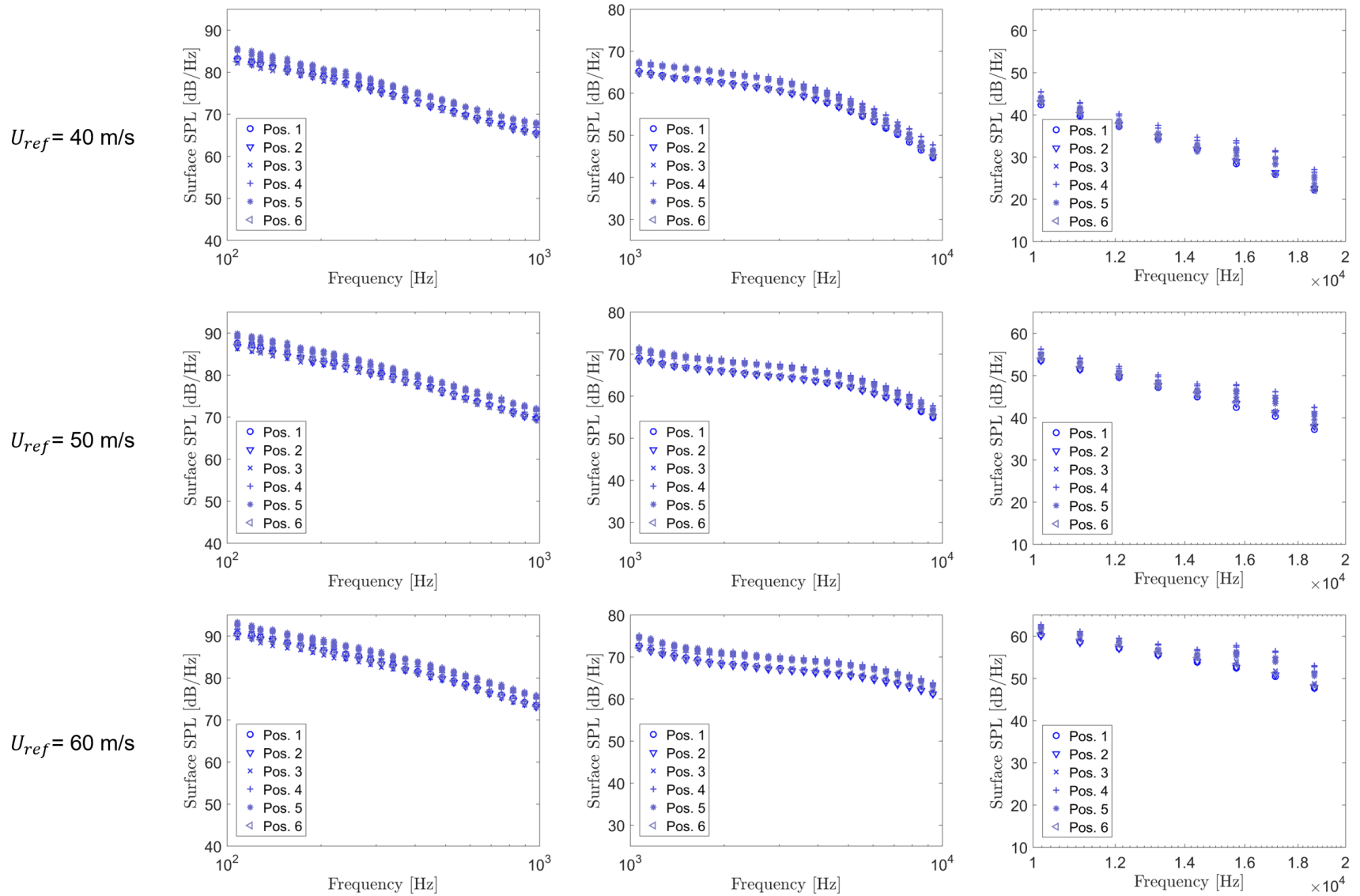
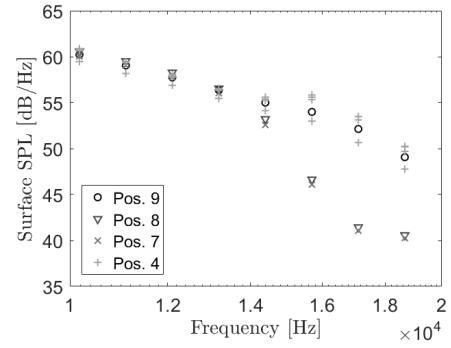
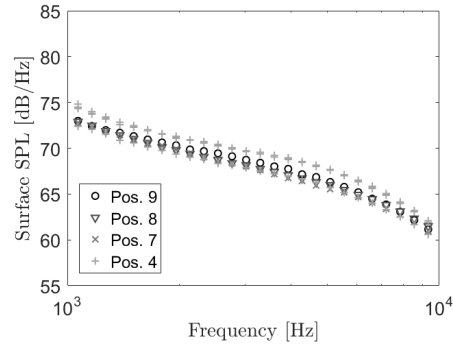
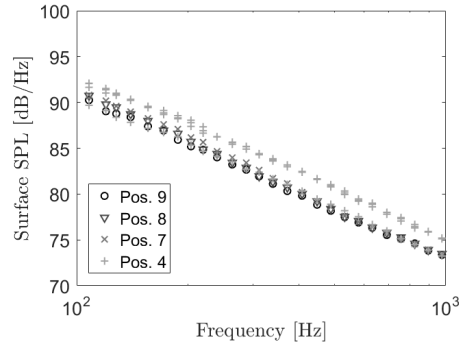
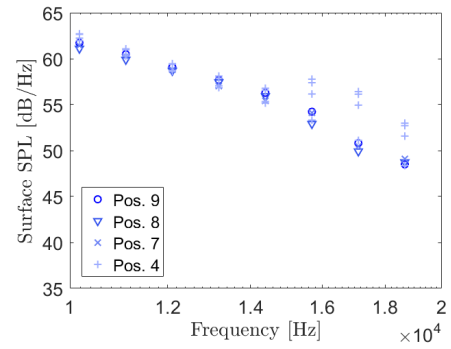
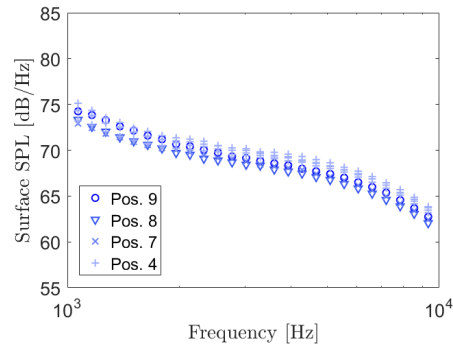
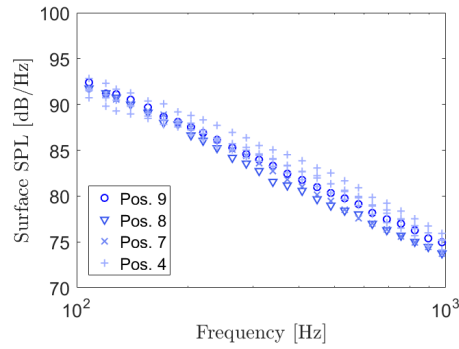


Figure 3.33: Surface pressure spectra variation in the spanwise direction for the trailing edge with Baseline finlets applied. Each row represents a different speed ($U_{ref} = 40, 50,$ and 60 m/s). Each column represents a different frequency range (left to right, 100 - $1,000$ Hz, $1,000$ - $10,000$ Hz, and $10,000$ - $20,000$ Hz). Within each figure, the different symbols denote different, spanwise-aligned microphone positions.

Untreated T.E.,
 $U_{ref} = 60m/s$



T.E. w/ Baseline Finlets,
 $U_{ref} = 60m/s$



T.E. w/ Thick Finlets,
 $U_{ref} = 60m/s$

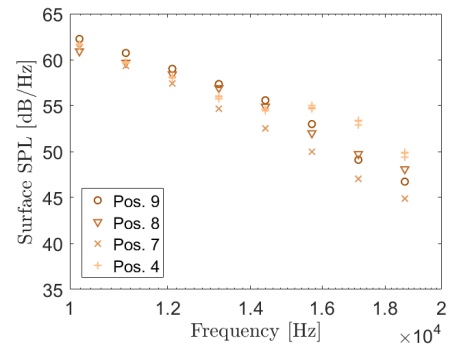
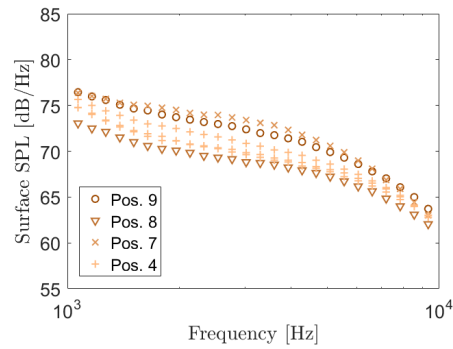
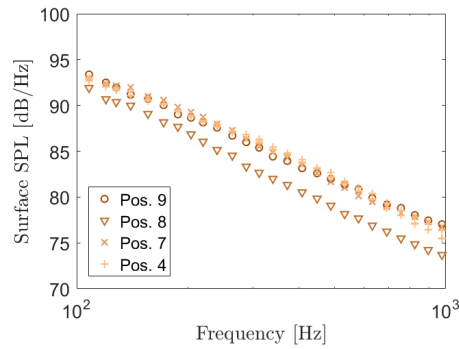
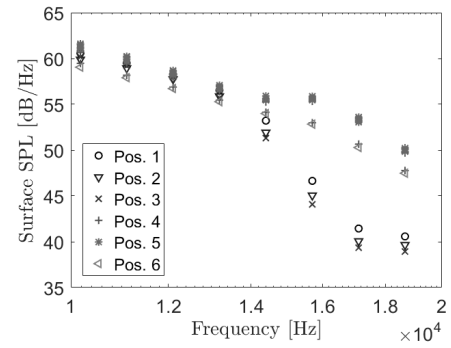
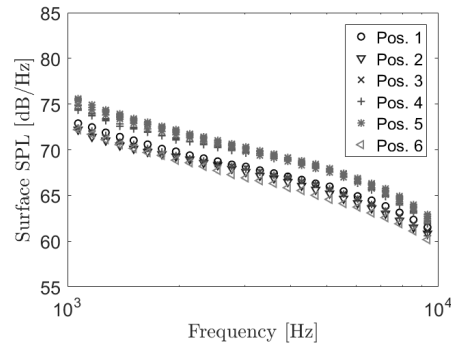
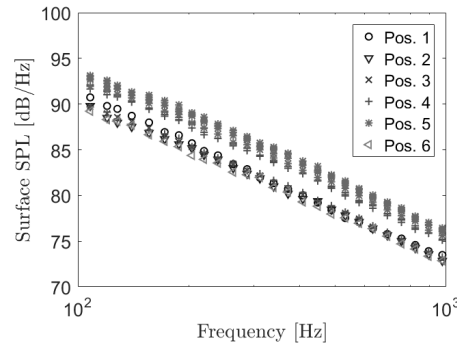


Figure 3.34: Surface pressure spectra variation in the streamwise direction for the untreated trailing edge (first row), trailing edge with Baseline finlets applied (second row), and trailing edge with Thick finlets applied (third row), measured at a jet speed of $U_{ref} = 60$ m/s. Each column represents a different frequency range (left to right, 100-1,000 Hz, 1,000-10,000 Hz, and 10,000-20,000 Hz). Within each figure, the different symbols denote different, streamwise-aligned microphone positions.

Untreated T.E.,
 $U_{ref} = 60\text{m/s}$



T.E. w/ Baseline Finlets,
 $U_{ref} = 60\text{m/s}$

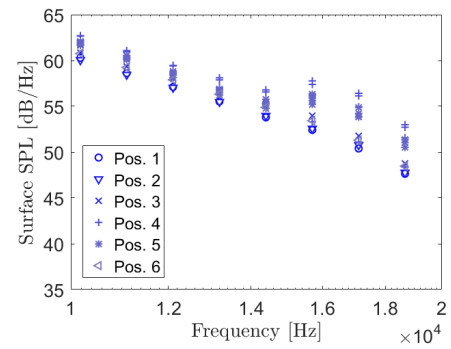
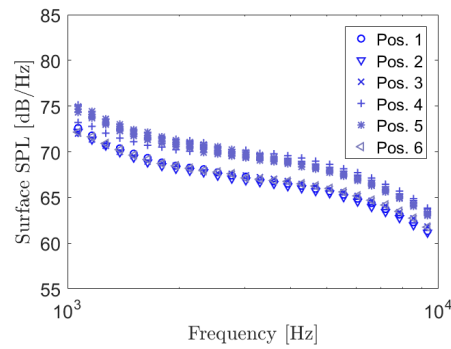
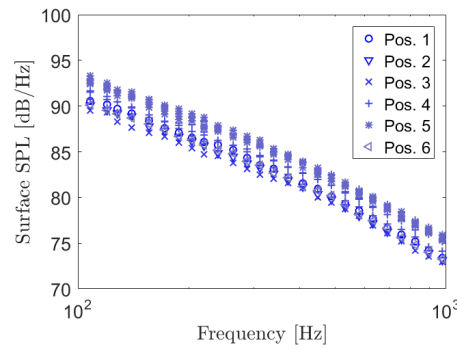
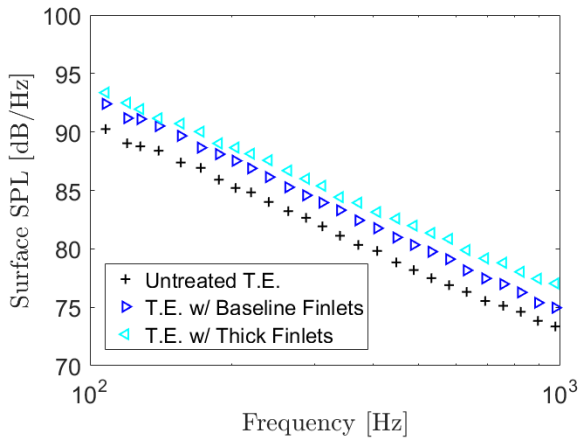
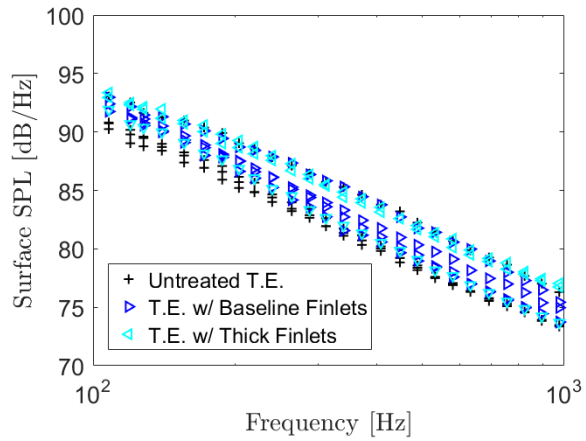


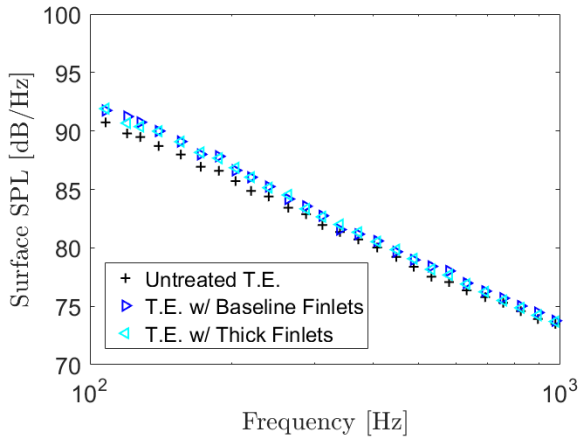
Figure 3.35: Surface pressure spectra variation in the spanwise direction for the untreated trailing edge (first row) and trailing edge with Baseline finlets applied (second row), measured at a jet speed of $U_{ref} = 60\text{ m/s}$. Each column represents a different frequency range (left to right, 100-1,000 Hz, 1,000-10,000 Hz, and 10,000-20,000 Hz). Within each figure, the different symbols denote different, spanwise-aligned microphone positions.



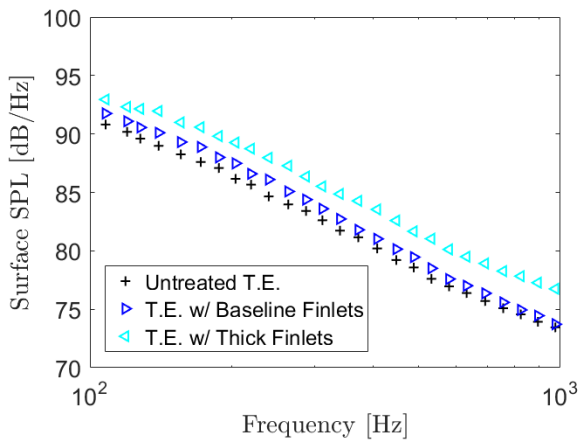
(a) Surface pressure spectra, position 9.



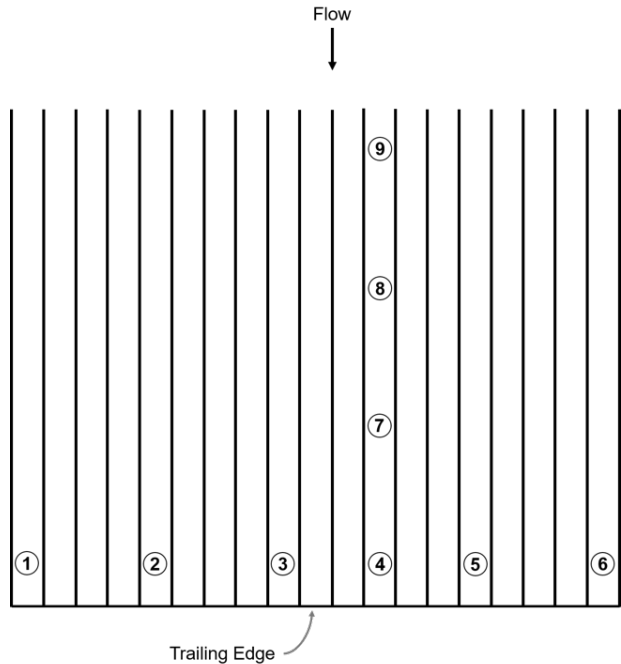
(d) Surface pressure spectra, position 4.



(b) Surface pressure spectra, position 8.

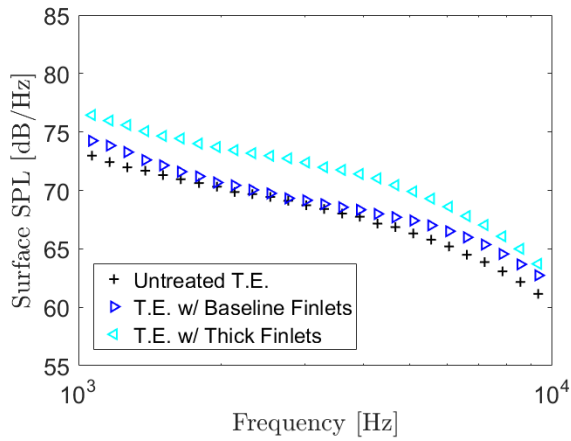


(c) Surface pressure spectra, position 7.

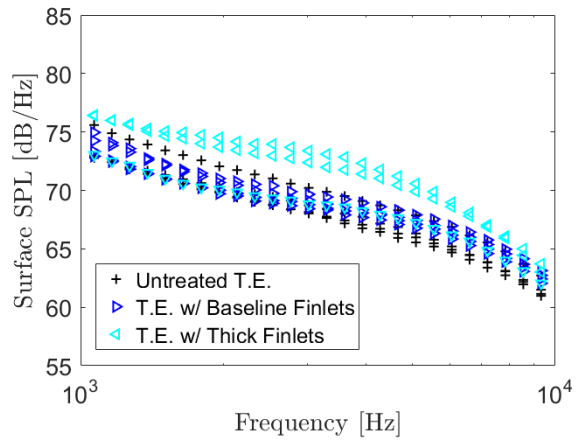


(e) Relative microphone positions

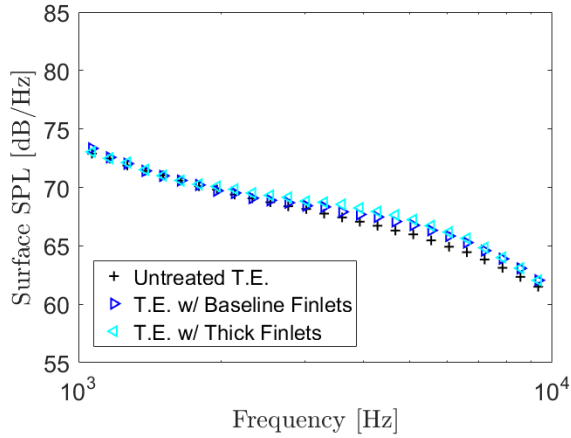
Figure 3.36: Surface pressure spectra at various streamwise positions, shown for $100 \leq f \leq 1,000$ Hz. **a-d)** Positions 9-7, 4, **e)** Top view (flow direction indicated with arrow) of relative surface pressure fluctuation microphone positions used in the experiment.



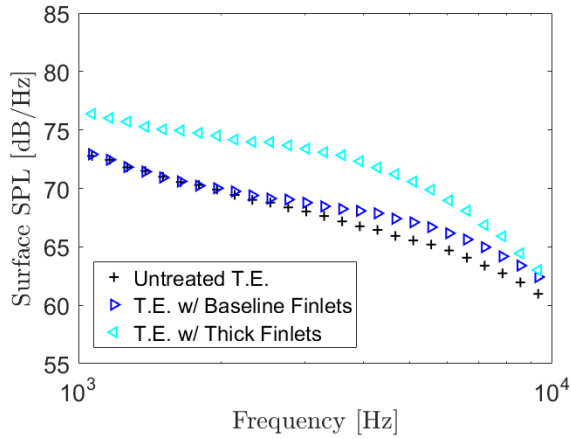
(a) Surface pressure spectra, position 9.



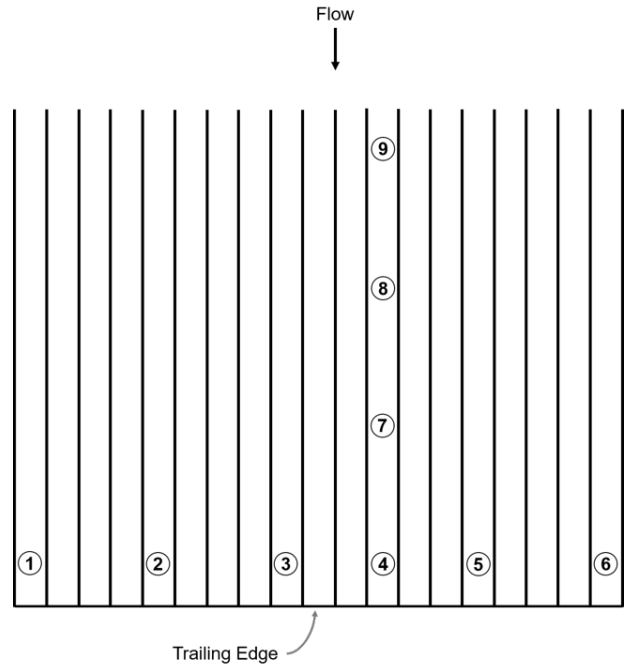
(d) Surface pressure spectra, position 4.



(b) Surface pressure spectra, position 8.

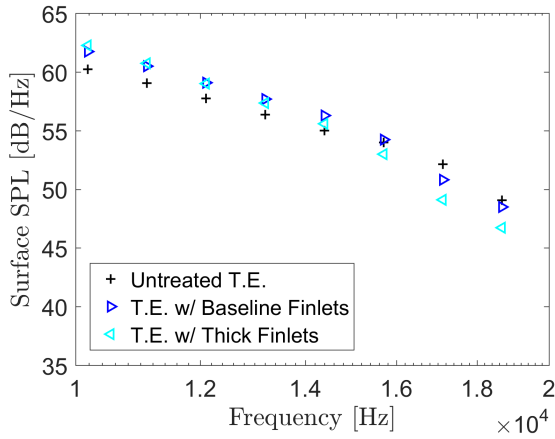


(c) Surface pressure spectra, position 7.

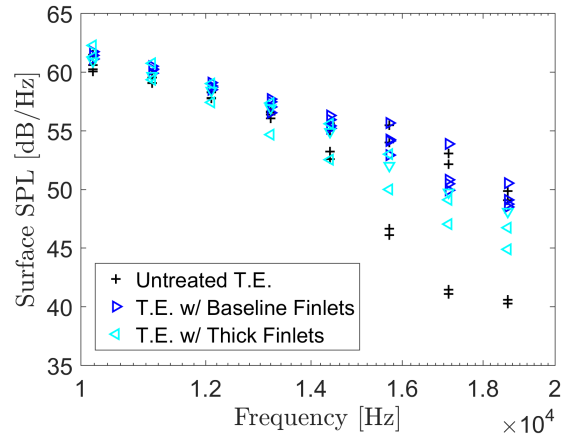


(e) Relative microphone positions

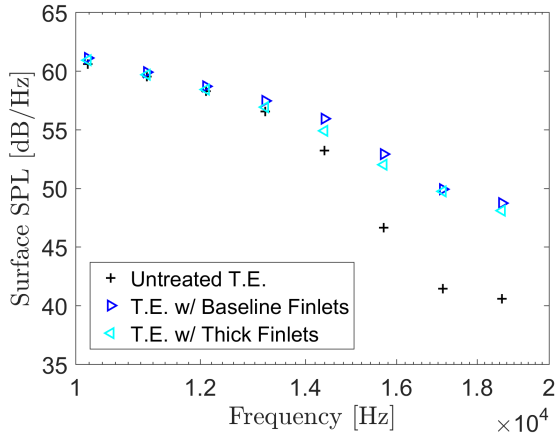
Figure 3.37: Surface pressure spectra at various streamwise positions, shown for $1,000 \leq f \leq 10,000$ Hz. **a-d)** Positions 9-7, 4, **e)** Top view (flow direction indicated with arrow) of relative surface pressure fluctuation microphone positions used in the experiment.



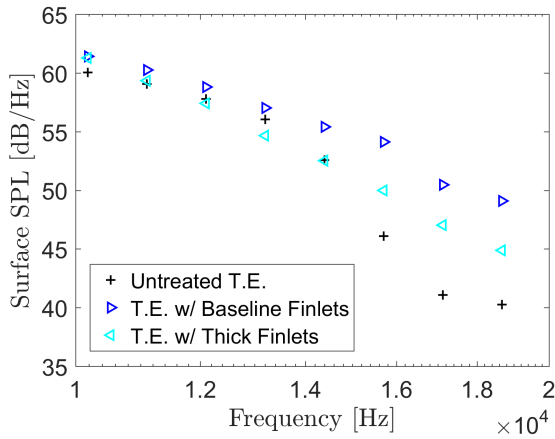
(a) Surface pressure spectra, position 9.



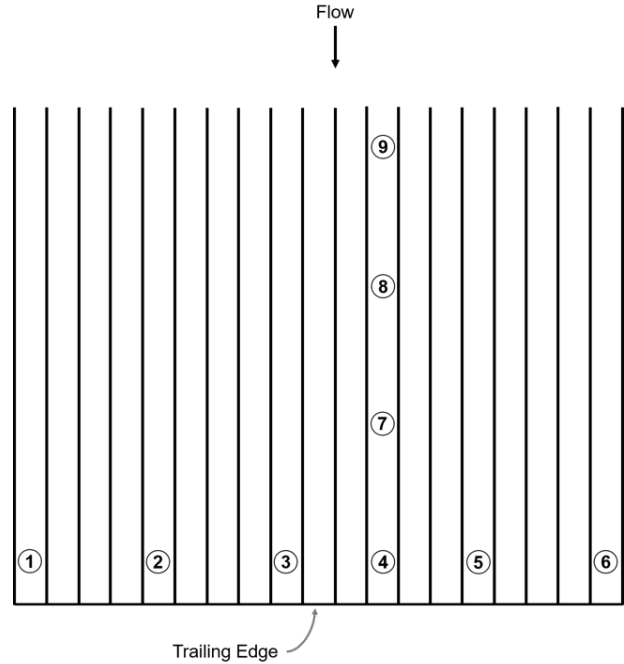
(d) Surface pressure spectra, position 4.



(b) Surface pressure spectra, position 8.

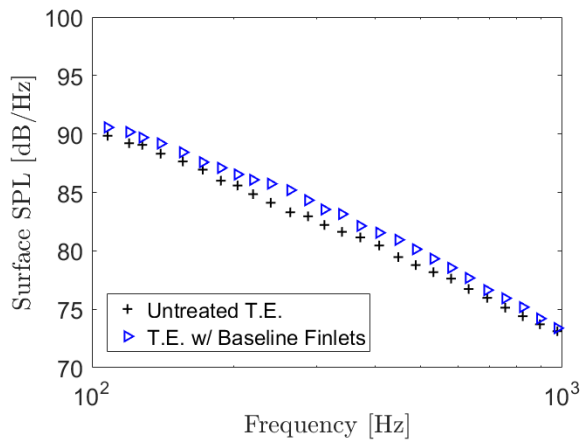


(c) Surface pressure spectra, position 7.

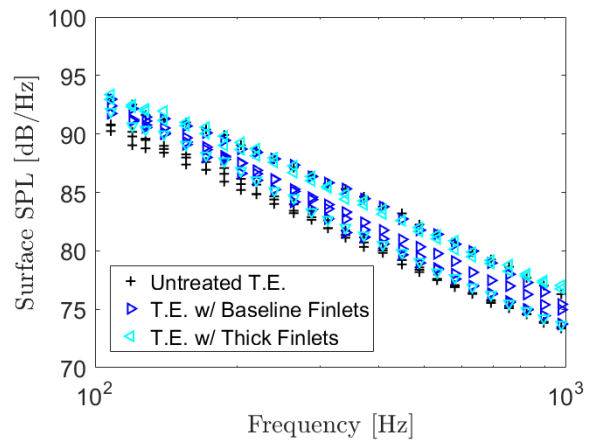


(e) Relative microphone positions

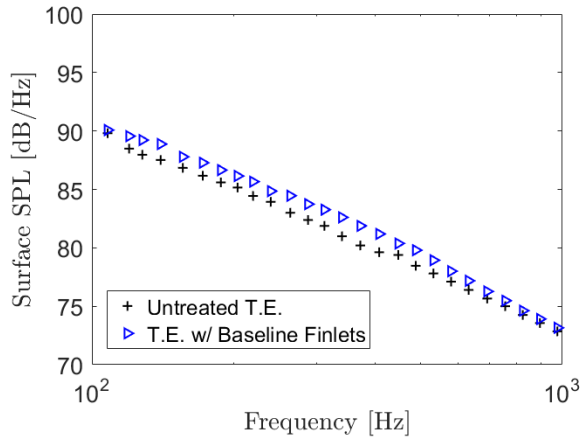
Figure 3.38: Surface pressure spectra at various streamwise positions, shown for $10,000 \leq f \leq 20,000$ Hz. **a-d)** Positions 9-7, 4, **e)** Top view (flow direction indicated with arrow) of relative surface pressure fluctuation microphone positions used in the experiment.



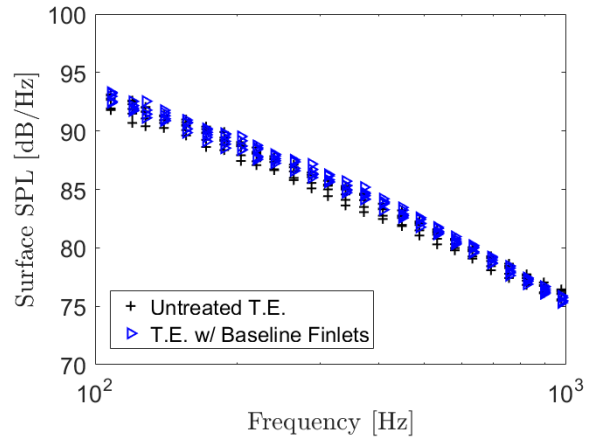
(a) Surface pressure spectra, position 1.



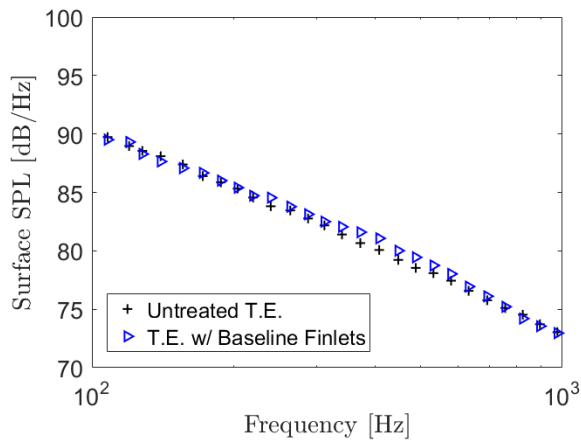
(d) Surface pressure spectra, position 4.



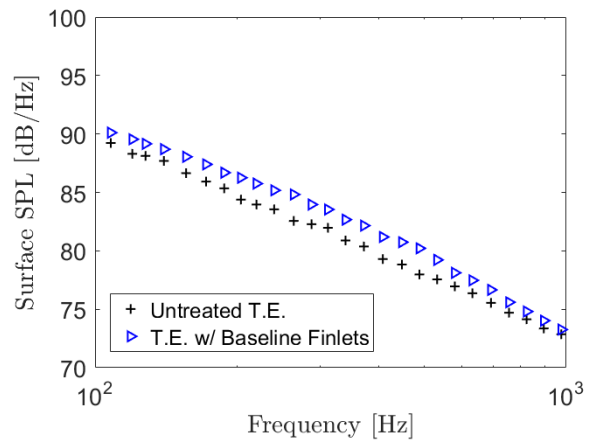
(b) Surface pressure spectra, position 2.



(e) Surface pressure spectra, position 5.

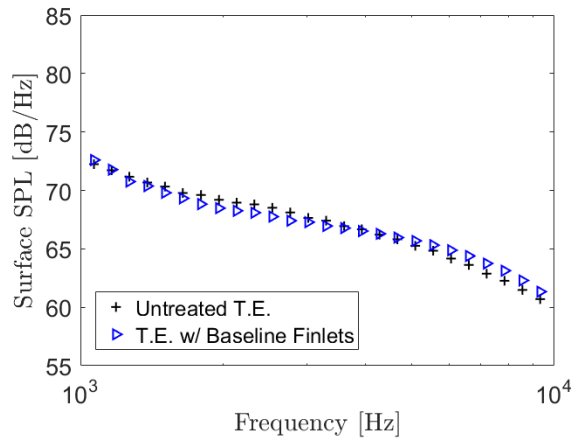


(c) Surface pressure spectra, position 3.

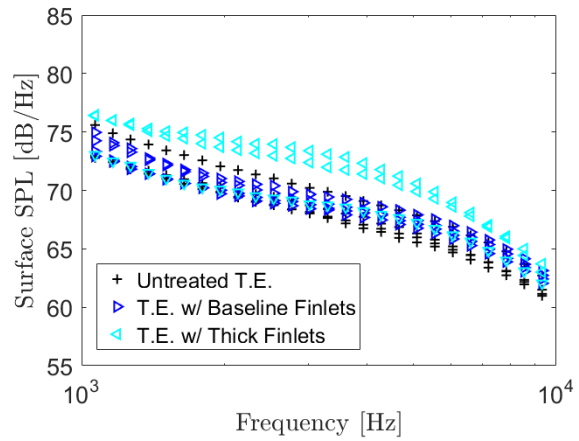


(f) Surface pressure spectra, position 6.

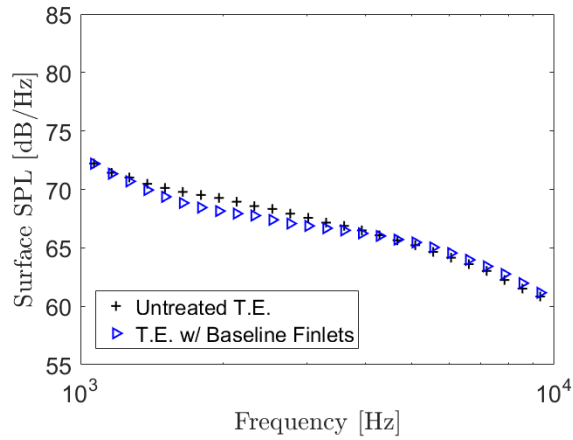
Figure 3.39: Surface pressure spectra at various spanwise positions, shown for $100 \leq f \leq 1,000$ Hz. Relative microphone positions are shown in figure 3.38e.



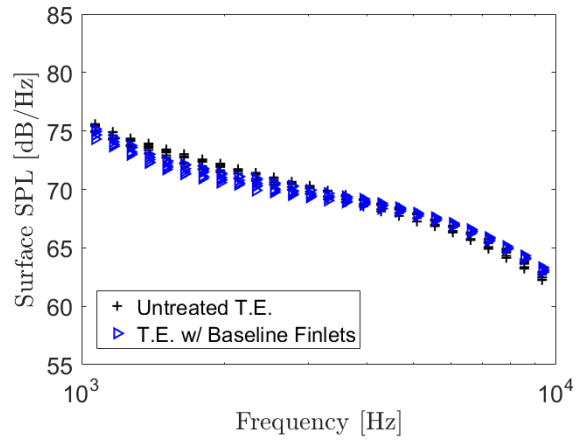
(a) Surface pressure spectra, position 1.



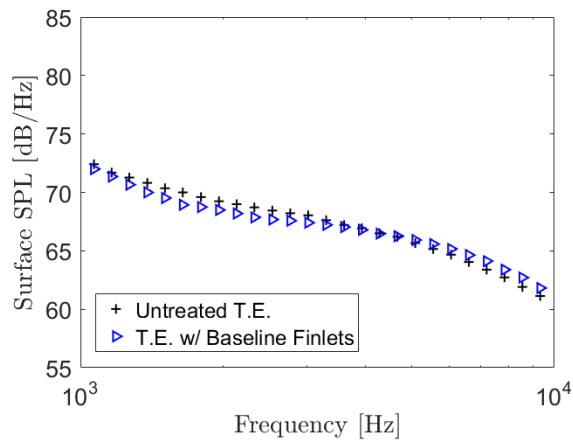
(d) Surface pressure spectra, position 4.



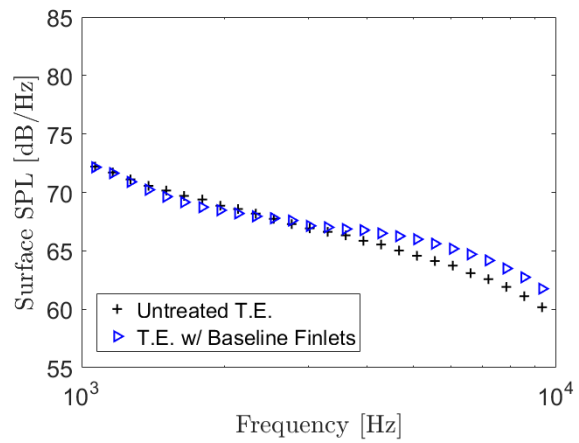
(b) Surface pressure spectra, position 2.



(e) Surface pressure spectra, position 5.

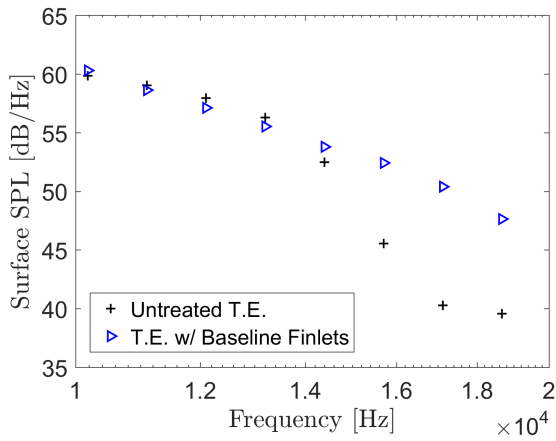


(c) Surface pressure spectra, position 3.

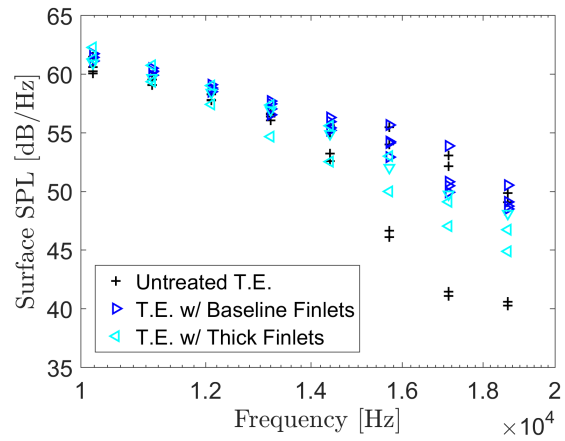


(f) Surface pressure spectra, position 6.

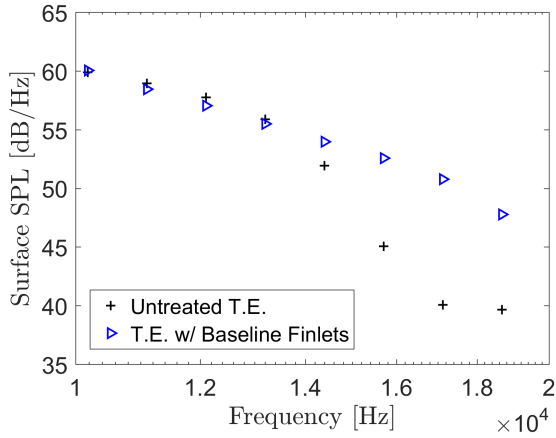
Figure 3.40: Surface pressure spectra at various spanwise positions, shown for $1,000 \leq f \leq 10,000$ Hz. Relative microphone positions are shown in figure 3.38e.



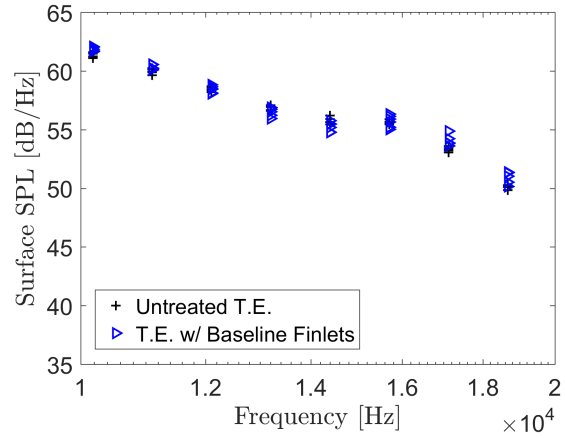
(a) Surface pressure spectra, position 1.



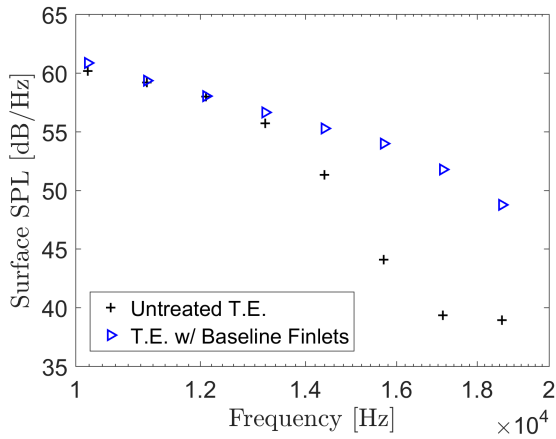
(d) Surface pressure spectra, position 4.



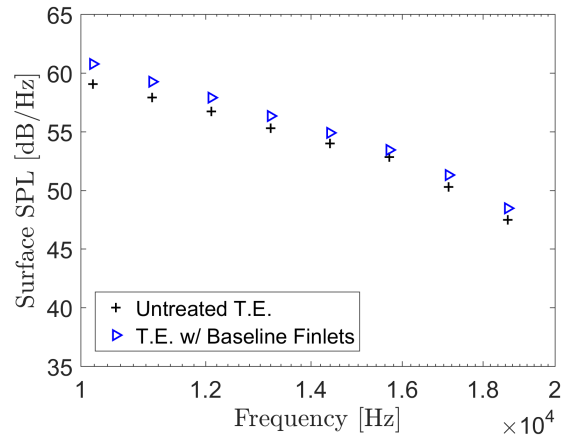
(b) Surface pressure spectra, position 2.



(e) Surface pressure spectra, position 5.

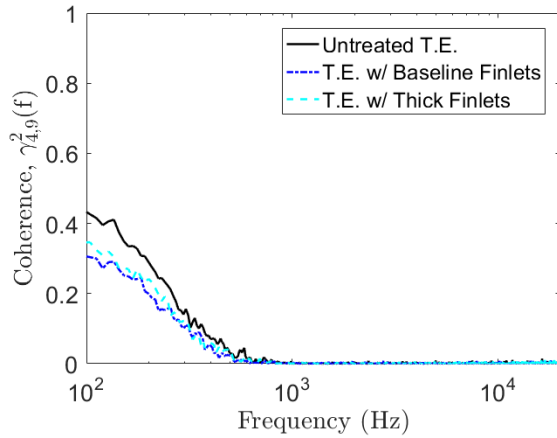
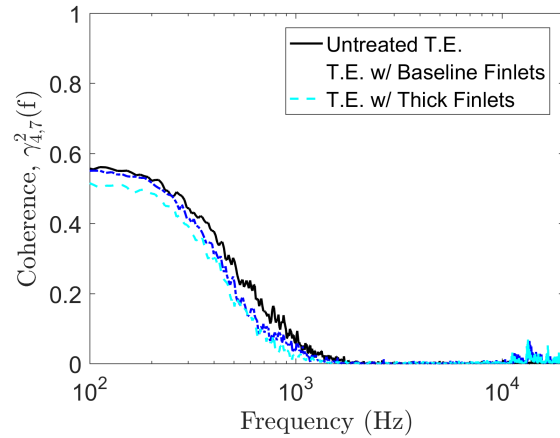
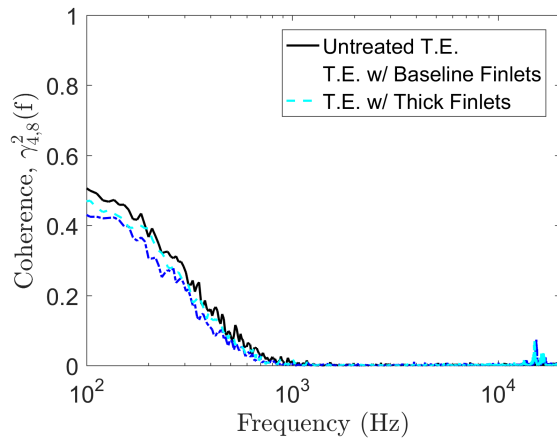
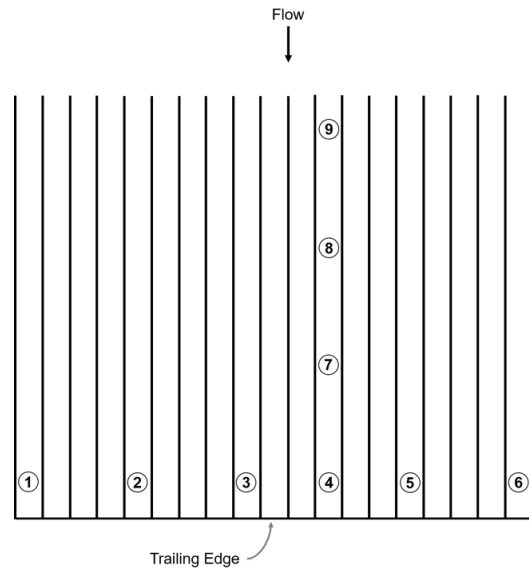


(c) Surface pressure spectra, position 3.



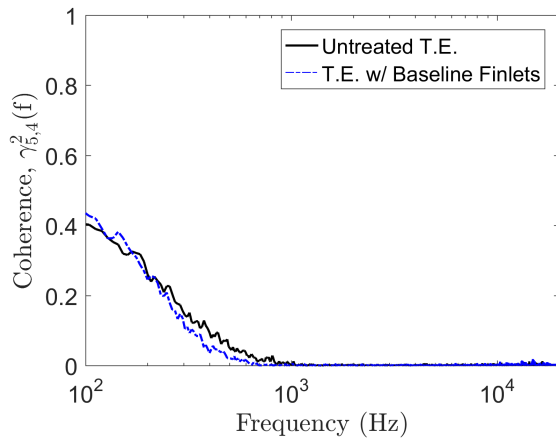
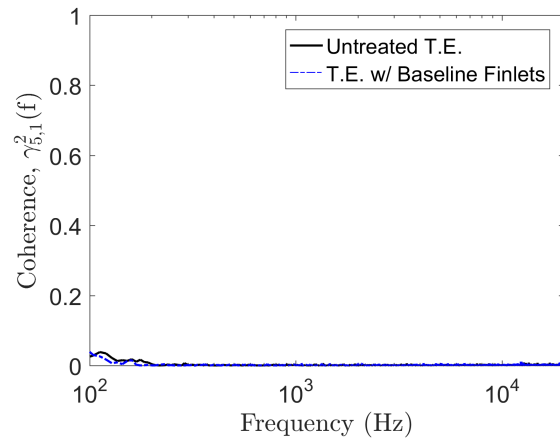
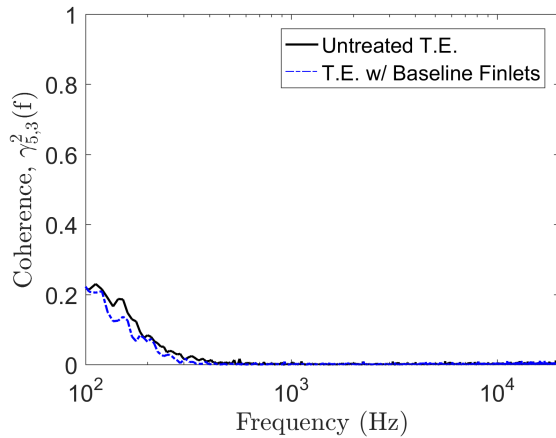
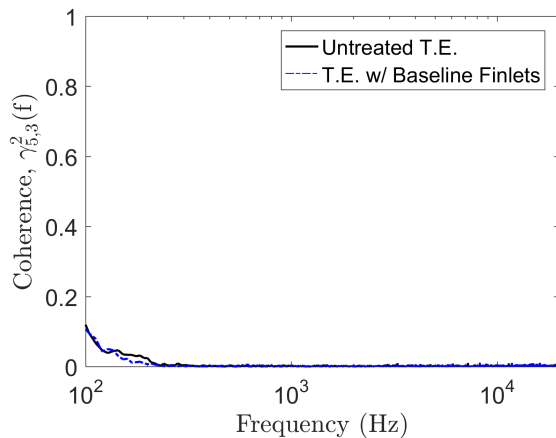
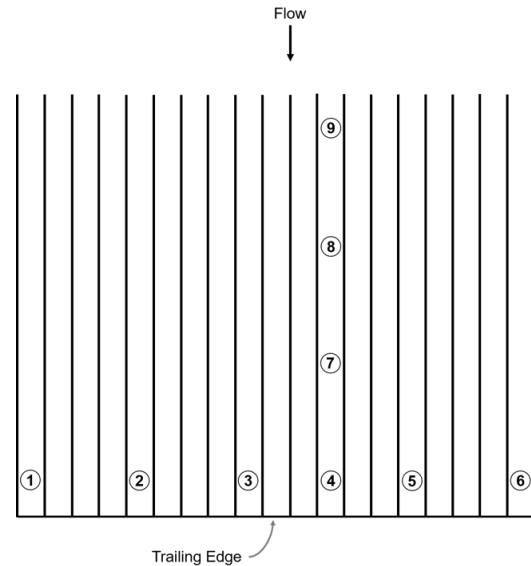
(f) Surface pressure spectra, position 6.

Figure 3.41: Surface pressure spectra at various spanwise positions, shown for $10,000 \leq f \leq 20,000$ Hz. Relative microphone positions are shown in figure 3.38e.

(a) Coherence, positions 4-9, $\Delta x = 57.15$ mm.(c) Coherence between positions 4-7, $\Delta x = 19.05$ mm.(b) Coherence, positions 4-8, $\Delta x = 38.1$ mm.

(d) Relative microphone positions.

Figure 3.42: Coherence between streamwise pairs of surface pressure fluctuation microphones. **a)** Positions 4-9, $\Delta x = 57.15$ mm, **b)** Positions 4-8, $\Delta x = 38.1$ mm, **c)** Positions 4-7, $\Delta x = 19.05$ mm, **d)** Top view (flow direction indicated with arrow) of relative positions surface pressure fluctuation microphone positions used in the experiment.

(a) Coherence, positions 5-4, $\Delta z = 13.27$ mm.(d) Coherence, positions 5-1, $\Delta z = 50.3$ mm.(b) Coherence, positions 5-3, $\Delta z = 27.44$ mm.(c) Coherence, positions 5-2, $\Delta z = 45.72$ mm.

(e) Relative microphone positions.

Figure 3.43: Coherence between spanwise pairs of surface pressure fluctuation microphones. **a)** Positions 5-4, $\Delta z = 13.27$ mm, **b)** Positions 5-3, $\Delta z = 27.44$ mm, **c)** Positions 5-2, $\Delta z = 45.72$ mm, **d)** Positions 5-1, $\Delta z = 50.3$ mm, **d)** Top view (flow direction indicated with arrow) of relative positions surface pressure fluctuation microphone positions used in the experiment.

Chapter 4

Conclusions

Existing trailing edge noise control technology, ranging from mature concepts such as serrations, to developing concepts such as porous airfoils, rely on altering the physical trailing edge (the scattering efficiency). It would be desirable to develop a noise control strategy based on manipulating the boundary layer turbulence upstream of the trailing edge. The goal of this thesis is to build on the body of knowledge created by Clark *et al.* [2, 7, 1] to establish manipulation of boundary layer turbulence as a viable method of trailing edge noise control. This was accomplished through a comprehensive wall jet experiment involving far-field noise measurements, measurements of surface pressure fluctuations, and hot-wire measurements. To the best of author's knowledge, this is the first experiment documenting the flow immediately downstream of bio-inspired finlet and rail trailing edge treatments.

Using a mock trailing edge as a testbed for various finlet and rail concepts designed to replicate treatments validated by Clark *et al.* [2, 7, 1], far-field noise measurements showed that each design significantly reduced the radiated noise by between 2 and 7 dB, effective at frequencies between about 1.5 and 10 kHz. At high frequencies, the finlets increased the noise; for example, by up to 2.7 dB at 15 kHz. No sound directionality was seen when the finlets were applied to the trailing edge. The results further suggest that treatments with the smallest spacing (2 mm, in this experiment) produced the most attenuation.

Velocity measurements made with a single hot-wire placed 3 mm downstream of the trailing edge with and without the noise treatments led to the development of a shear-sheltering hypothesis. Essentially, the treatments create a local mixing layer at the top of the treatments, analogous to flow over rough surfaces in the atmospheric boundary layer. The mixing layer prevents turbulent structures of a certain size that are present in the boundary layer from impacting the trailing edge and producing sound, e.g. sheltering the edge from larger coherent structures. The presence of the mixing layer was identified in the hot-wire data by examining the gradients in the mean velocity profiles, the turbulence intensity profiles, and the change in the power spectral densities of the velocity fluctuations. The finlets with the

2 mm spacing reduced the turbulence levels by over 6 dB relative to the untreated trailing edge, occurring at about 5.5 kHz, the frequency at which the highest acoustic attenuation was seen. In general, the acoustic results seem to indicate that treatments creating a strong mixing layer (characterized by a large velocity gradient or small vorticity thickness) have the largest reduction in far-field noise. The strength of the mixing layer appears to be dependent on the treatment spacing, e.g. a narrower spacing leads to a stronger mixing layer.

Unsteady surface pressure fluctuations between finlet channels were measured using microphones placed at nine different positions. Adding the finlet treatments to the trailing edge tended to increase the magnitude of the pressure fluctuations. Similar behavior was measured by Clark *et al.* [2] on the pressure side of a wind turbine airfoil, also measured with unsteady surface pressure transducers placed along finlet channels. In this experiment, the coherence between pairs of microphones placed along the trailing edge span was reduced, coherence was reduced by up to 0.09 with the application of finlets. This is consistent with the findings reported by Clark [25], which indicated that the noise reduction associated with finlets was due to a combination of displacing turbulent structures away from the trailing edge and reducing the spanwise pressure correlation lengthscales. Overall, these findings support the current understanding of finlet performance [1, 2, 24], and represent a significant contribution toward understanding the local aerodynamics of finlets and the associated aeroacoustic impacts and validating boundary layer manipulation as a viable method of trailing edge noise control.

Bibliography

- [1] Ian A. Clark, W. Nathan Alexander, William Devenport, Stewart Glegg, Justin W. Jaworski, Conor Daly, and Nigel Peake. Bioinspired trailing-edge noise control. *AIAA Journal*, 55(3):740–754, 2017.
- [2] I. A. Clark, D. Baker, W. N. Alexander, W. Devenport, N. Peake, S. Glegg, and J. W. Jaworski. Experimental and theoretical analysis of bio-inspired trailing edge noise control devices. In *22nd AIAA/CEAS Aeroacoustics Conference, 30 May-1 June 2016*, 22nd AIAA/CEAS Aeroacoustics Conference, page 15 pp. American Institute of Aeronautics and Astronautics.
- [3] B. E. Launder and W. Rodi. The turbulent wall jet. *Progress in Aerospace Sciences*, 19:81–128, 1981.
- [4] Thomas F Brooks, D Stuart Pope, and Michael A Marcolini. *Airfoil self-noise and prediction*, volume 1218. National Aeronautics and Space Administration, Office of Management, Scientific and Technical Information Division, 1989.
- [5] Ian A. Clark. *A Study of Bio-Inspired Canopies for the Reduction of Roughness Noise*. Thesis, 2015.
- [6] William J. Devenport, Dustin L. Grissom, W. Nathan Alexander, Benjamin S. Smith, and Stewart A. L. Glegg. Measurements of roughness noise. *Journal of Sound and Vibration*, 330(17):4250–4273, 2011.
- [7] Ian A. Clark, Conor A. Daly, William Devenport, W. Nathan Alexander, Nigel Peake, Justin W. Jaworski, and Stewart Glegg. Bio-inspired canopies for the reduction of roughness noise. *Journal of Sound and Vibration*, 385(22):33–54, 2016.
- [8] RR Graham. The silent flight of owls. *The Aeronautical Journal*, 38(286):837–843, 1934.
- [9] W. H. Thorpe and D. R. Griffin. The lack of ultrasonic components in the flight noise of owls compared with other birds. *Ibis*, 104(2):256–257, 1962.
- [10] Richard A Kroeger, Heinz D Grushka, and Tibor C Helvey. Low speed aerodynamics for ultra-quiet flight. Report, DTIC Document, 1972.

- [11] E. Sarradj, C. Fritzsche, and T. Geyer. Silent owl flight: Bird flyover noise measurements. *AIAA Journal*, 49(4):769–779, 2011.
- [12] Geoffrey M Lilley. A study of the silent flight of the owl. *AIAA paper*, 2340(1998):1–6, 1998.
- [13] HD Gruschka, IU Borchers, and JG Coble. Aerodynamic noise produced by a gliding owl. *Nature*, 233:409–411, 1971.
- [14] MS Howe. Aerodynamic noise of a serrated trailing edge. *Journal of Fluids and Structures*, 5(1):33–45, 1991.
- [15] Michael J Lighthill. On sound generated aerodynamically. i. general theory. In *Proceedings of the Royal Society of London A: Mathematical, Physical and Engineering Sciences*, volume 211, pages 564–587. The Royal Society, 1952.
- [16] JE Ffowcs Williams and LH Hall. Aerodynamic sound generation by turbulent flow in the vicinity of a scattering half plane. *Journal of Fluid Mechanics*, 40(04):657–670, 1970.
- [17] RK Amiet. Noise due to turbulent flow past a trailing edge. *Journal of sound and vibration*, 47(3):387–393, 1976.
- [18] R.K. Amiet. Effect of the incident surface pressure field on noise due to turbulent flow past a trailing edge. *Journal of Sound and Vibration*, 57(2):305–306, 1978.
- [19] Terry D Scharton, Benjamin Pinkel, and John F Wilby. A study of trailing edge blowing as a means of reducing noise generated by the interaction of flow with a surface. 1973.
- [20] Stefan Oerlemans, Murray Fisher, Thierry Maeder, and Klaus Kögler. Reduction of wind turbine noise using optimized airfoils and trailing-edge serrations. *AIAA journal*, 47(6):1470–1481, 2009.
- [21] Michaela Herr and Werner Dobrzynski. Experimental investigations in low-noise trailing edge design. *AIAA journal*, 43(6):1167–1175, 2005.
- [22] T. Geyer, E. Sarradj, and C. Fritzsche. Measurement of the noise generation at the trailing edge of porous airfoils. *Experiments in Fluids*, 48(2):291–308, 2010.
- [23] I. Clark, N. Alexander William, J. Devenport William, A. Glegg Stewart, Jaworski Justin, Daly Conor, and Peake Nigel. Bio-inspired trailing edge noise control. In *21st AIAA/CEAS Aeroacoustics Conference*, AIAA Aviation. American Institute of Aeronautics and Astronautics.

- [24] A. Afshari, M. Azarpeyvand, A. A. Dehghan, and M. Szoke. Trailing edge noise reduction using novel surface treatments. In *22nd AIAA/CEAS Aeroacoustics Conference, 30 May-1 June 2016*, 22nd AIAA/CEAS Aeroacoustics Conference, page 15 pp. American Institute of Aeronautics and Astronautics.
- [25] Ian A. Clark. *Bio-Inspired Control of Roughness and Trailing Edge Noise*. Dissertation, 2017.
- [26] Abbas Afshari, Ali A. Dehghan, Mahdi Azarpeyvand, and Mate Szoke. Three-dimensional surface treatments for trailing edge noise reduction. In *23rd International Congress on Sound and Vibration, ICSV 2016, July 10, 2016 - July 14, 2016*, ICSV 2016 - 23rd International Congress on Sound and Vibration: From Ancient to Modern Acoustics, page Dynamic Acoustics S.A.; et al.; Hellenic Association; Pemard; T and S Technologies Group; Traffic Transportation and Environment Consultants SA (TT and E S.A.). International Institute of Acoustics and Vibrations.
- [27] Dustin Grissom, Benjamin Smith, William Devenport, and Stewart Glegg. Rough-wall boundary layer noise: An experimental investigation. In *13th AIAA/CEAS Aeroacoustics Conference (28th AIAA Aeroacoustics Conference)*, Aeroacoustics Conferences. American Institute of Aeronautics and Astronautics.
- [28] I.J. Wygnanski, Y. Katz, and E. Horev. On the applicability of various scaling laws to the turbulent wall jet. *Journal of Fluid Mechanics*, 234:669–690, 1992.
- [29] William Devenport, Elisabeth A. Wahl, Stewart A. L. Glegg, W. Nathan Alexander, and Dustin L. Grissom. Measuring surface pressure with far field acoustics. *Journal of Sound and Vibration*, 329(19):3958–3971, 2010.
- [30] Julius S Bendat and Allan G Piersol. *Random data: analysis and measurement procedures*, volume 729. John Wiley & Sons, 2011.
- [31] Liselle A. Joseph, Timothy W. Meyers, Nicholas J. Molinaro, and William J. Devenport. *Pressure Fluctuations in a High-Reynolds-Number Turbulent Boundary Layer Flow over Rough Surfaces*. Aeroacoustics Conferences. American Institute of Aeronautics and Astronautics, 2016.
- [32] PW Bearman. Corrections for the effect of ambient temperature drift on hot-wire measurements in incompressible flow. *DISA information*, 11(1):25–30, 1971.
- [33] F.E. Jorgensen. How to measure turbulence with hot-wire anemometers. Report, DANTEC Dynamics, 2002.
- [34] J. H. Bell and R. D. Mehta. Measurements of the streamwise vortical structures in a plane mixing layer. *Journal of Fluid Mechanics*, 239:213–248, 1992.

- [35] I. N. Harman and J. J. Finnigan. A simple unified theory for flow in the canopy and roughness sublayer. *Boundary-Layer Meteorology*, 123(2):339–363, 2007.
- [36] M. R. Raupach, J. J. Finnigan, and Y. Brunet. Coherent eddies and turbulence in vegetation canopies: The mixing-layer analogy. *Boundary-Layer Meteorology*, 78(3-4):351–382, 1996.
- [37] J.C.R. Hunt and P.A. Durbin. Perturbed vortical layers and shear sheltering. *Fluid Dynamics Research*, 24(6):375 – 404, 1999.
- [38] MR Raupach and A St Thom. Turbulence in and above plant canopies. *Annual Review of Fluid Mechanics*, 13(1):97–129, 1981.
- [39] John Finnigan. Turbulence in plant canopies. *Annual Review of Fluid Mechanics*, 32:519, 2000.
- [40] Ann-Sofi Smedman, Ulf Hgstrm, and J. C. R. Hunt. Effects of shear sheltering in a stable atmospheric boundary layer with strong shear. *Quarterly Journal of the Royal Meteorological Society*, 130(596):31–50, 2004.